Self-consistent quantum-electrostatics

Pacôme Armagnat

Communauté
UNIVERSITÉ Grenoble Alpes

THÈSE

Pour obtenir le grade de

DOCTEUR DE LA COMMUNAUTE UNIVERSITE GRENOBLE ALPES

Spécialité : **Physique Théorique**

Arrêté ministériel : 25 mai 2016

Présentée par

Pacôme Armagnat

Thèse dirigée par **Xavier WAINTAL**, et
codirigée par **Christoph GROTH**

préparée au sein du **laboratoire de PHotonique ELécronique et Ingénieries QuantiqueS**
dans **l'École Doctorale de physique de Grenoble**

Physique quantique et éléctrostatique auto-cohérentes

Thèse soutenue publiquement le **« 26 Juin 2019 »**,
devant le jury composé de :

M. Michael WIMMER
Professeur, TU DELFT (Rapporteur)
M. Patrice ROCHE
Directeur de recherche, CEA Saclay SPEC/GNE (Rapporteur)
M. Christopher BAUERLE
Directeur de recherche, Insitut Néel (Membre)
M. Xavier BLASE
Directeur de recherche, Institut Néel (Président)
M. Gwendal FÈVE
Maître de conférences, LPA Paris (Membre)

Abstract

Electrostatic energy is very often the largest energy scale in quantum nanoelectronic systems. Yet, in theoretical work or numerical simulations, the electrostatic landscape is equally often taken for granted as an external potential, which may result in a wrong physical picture. Developing numerical tools that can properly handle the electrostatics and its interplay with quantum mechanics is of utter importance for the understanding of quantum devices in e.g. semi-conducting or graphene like materials.

This thesis is devoted to the self-consistent quantum-electrostatic problem. This problem (also known as Poisson-Schrödinger) is notoriously difficult in situations where the density of states varies rapidly with energy. At low temperatures, these fluctuations make the problem highly non-linear which renders iterative schemes deeply unstable. In this thesis, we present a stable algorithm that provides a solution to this problem with controlled accuracy. The technique is intrinsically convergent including in highly non-linear regimes. Thus, it provides a viable route for the predictive modeling of the transport properties of quantum nanoelectronics devices. We illustrate our approach with a calculation of the differential conductance of a quantum point contact geometry. We also revisit the problem of the compressible and incompressible stripes in the integer quantum Hall regime. Our calculations reveal the existence of a new "hybrid" phase at intermediate magnetic field that separate the low field phase from the high field stripes.

In a second part we construct a theory that describes the propagation of the collective excitations (plasmons) that can be excited in two-dimensional electron gases. Our theory, which reduces to Luttinger liquid in one dimension can be directly connected to the microscopic quantum-electrostatic problem enabling us to make predictions free of any free parameters. We discuss recent experiments made in Grenoble that aim at demonstrating electronic flying quantum bits. We find that our theory agrees quantitatively with the experimental data.

Résumé

Dans un système nano-électronique quantique, l'énergie électrostatique représente souvent la plus grand échelle d'énergie. Pourtant, dans les travaux théoriques ou les simulations quantiques, l'environnement électrostatique est tout aussi souvent considérée comme un potentiel externe, ce qui peut conduire à une mauvaise représentation de la physique. Le développement d'outils numériques capables de traiter correctement l'électrostatique et son interaction avec la mécanique quantique est d'une importance capitale pour la compréhension des dispositifs quantiques, pax exemple dans les matériaux semi-conducteurs ou le graphène.

Cette thèse est consacrée au problème de la physique quantique et électrostatique autocohérente. Ce problème (également connu sous le nom de Poisson-Schrödinger") est notoirement difficile dans des situations où la densité des états varie rapidement avec l'énergie. A basse température, ces fluctuations rendent le problème hautement non linéaire, ce qui rend les schémas itératifs profondément instables. Dans cette thèse, nous présentons un algorithme stable qui apporte une solution à ce problème avec une précision contrôlée. La technique est intrinsèquement convergente, y compris dans les régimes très non linéaires. Il fournit ainsi une voie viable pour la modélisation prédictive des propriétés de transport des dispositifs de nanoélectronique quantique. Nous illustrons notre approche par un calcul de la conductance différentielle d'un point de contact quantique. Nous réexaminons également le problème des bandes compressibles et incompressibles dans le régime de l'effet Hall quantique entier. Nos calculs révèlent l'existence d'une nouvelle phase "hybride" pour les champ magnétiques intermédiaires, qui sépare la phase à faible champ des bandes (in)compressibles à champ élevé.

Dans une deuxième partie, nous construisons une théorie qui décrit la propagation des excitations collectives (plasmons) qui peuvent être excitées dans des gaz électroniques bidimensionnels. Notre théorie, qui se réduit au liquide de Luttinger en une dimension, peut être directement reliée au problème électrostatique quantique microscopique, ce qui nous permet de faire des prédictions sans aucun paramètre libre. Nous discutons des expériences récemment faites à Grenoble, qui visent à démontrer la faisabilité de bits quantiques volants. Nous constatons que notre théorie concorde quantitativement avec les données expérimentales.

Contents

Introduction **11**

I The self-consistent quantum-electrostatic problem in highly non linear situation **17**

1 Introduction to the self-consistent quantum-electrostatic problem **21**
1.1 Formulation of the self-consistent quantum-electrostatic problem . . . 21
1.2 Review of the different approaches . . . 23
1.2.1 Direct methods . . . 23
1.2.2 Indirect methods . . . 26

2 The local adiabatic problem approach **29**
2.1 Role of non-linearities: a zero-dimensional toy model . . . 29
2.2 The adiabatic self-consistent problem . . . 30
2.2.1 Quantum Adiabatic Approximation (QAA) . . . 32
2.2.2 Poisson Adiabatic Approximation (PAA) . . . 34
2.2.3 Solving the local self-consistent problems . . . 34
2.3 Relaxing the Adiabatic self-consistent problem . . . 36
2.4 A mixed Neuman-Dirichlet Poisson solver . . . 40
2.4.1 Problem formulation . . . 40
2.4.2 Finite volume discretization . . . 41
2.5 Calculation of the integrated local density of states . . . 42
2.6 Conclusion . . . 43

3 Applications to a quantum point contact **45**

4 Application to the quantum Hall effect **53**
4.1 Introduction . . . 53
4.2 The LB picture of the QHE regime (and its failure) . . . 54
4.3 The CSG picture of compressible and incompressible stripes . . . 57
4.4 New results . . . 58
4.4.1 Hybrid phase at intermediate fields . . . 58

4.4.2 Magneto-conductance of ballistic wires . . . 58
4.4.3 Discussion . . . 60
4.5 Complementary informations . . . 61

II The flying qubit project 67

5 The flying qubit project 71
5.1 What is a flying qubit and why is it interesting . . . 72
5.1.1 What is a flying qubit ? . . . 72
5.1.2 How to theoretically build a flying qubit quantum computer . . . 72
5.1.3 Advantages of a flying qubit . . . 73
5.2 Toward flying qubit spectroscopy . . . 75
5.2.1 Mach-Zender interferometer for electrons . . . 77
5.2.2 Introduction to rectification currents . . . 78
5.2.3 Realistic model of the MZI and self consistent calculations . . . 79
5.2.4 Spectroscopy of the Flying qubit . . . 82

6 Time of flight experiment 85
6.1 Description of the experiment . . . 85
6.1.1 The sample . . . 85
6.1.2 The time resolved method . . . 86
6.2 Results : measurement of the renormalized velocities . . . 87
6.2.1 conclusion . . . 89

7 Theory of plasmon propagation 91
7.1 Formulation of the Self-consistent Boltzmann-Poisson problem . . . 91
7.2 Application to plasmons in one and two dimensions . . . 92
7.2.1 Electrostatic problem . . . 93
7.2.2 Boltzman problem. . . . 93
7.2.3 Self-consistent problem in two dimensions . . . 94
7.3 Application to quasi-one dimensional plasmons . . . 94
7.3.1 self-consistent calculations . . . 95
7.3.2 Infinite range interaction limit . . . 96

8 Numerical calculation of plasmons velocity 99
8.1 Self consistent calculations . . . 99
8.1.1 Self-consistent electrostatic-quantum problem . . . 100
8.2 velocity calculations . . . 102

9 Conclusion 107

III Appendix 109

A Calculation of the Lindhart function 111
A.1 Bloch picture and Dyson equation . . . 112
A.2 Calculation of the residues . . . 113
A.3 Calculation of the upper integral of the contour . . . 114

B On the ionization of dopants 115

C Integrating the LDOS 117
C.1 Generalities on interpolation . . . 117
C.1.1 Direct integration and interpolation . . . 117
C.1.2 Gaussian quadratures . . . 118
C.1.3 Interpolation and Legendre quadratures . . . 119
C.2 Integration in the k space . . . 120
C.2.1 Simple integration . . . 120
C.2.2 Integration of interpolated function . . . 123

D More details on the IQHE 125
D.1 Landau levels . . . 125
D.2 Construction of compressible and incompressible stripes . . . 128
D.3 Estimation of the width of an incompressible plateau . . . 131

Bibliography 133

Introduction

Precision modeling for quantum nano-electronics

Important progress has been made in the understanding and realization of quantum materials, i.e. materials whose behavior can not be solely explained by classical physics but require using the concepts of quantum mechanics. Among these quantum materials are supraconductors and semi-conductor heterostructures but also new types of materials such as graphene, topological insulators or Majorana fermions. Moreover, progress has also been made in the manipulation of these materials. One can nowadays construct complex devices, bring them to ultra-low temperature (of the order of 10mK) and perform electronics at the nano scale. An example of such system that we studied in this thesis - a quantum point contact - is shown in Fig. 1 (a). A quantum gate allows to confine a two-dimensional electron gas, which forces electrons in a narrow system (i.e. with a width of the order of the Fermi wave length). This results in the conductance as a function of the gate confinement exhibiting plateaus (see Fig. 1 (b)). More details about this simple system will be provided later in this thesis.

The transition from research into nanoelectronic phenomena to research into combining and applying them inevitably leads to a dramatic increase in the complexity of the systems under study. In this thesis, we argue that this increasing complexity must be accompanied by precise numerical modeling. The corresponding numerical tools shall allow one to cover all the step between the microscopic model and the experimental observations. The quest for simple and efficient numerical methods is at the center of the work done in the laboratory where this work was done, and is perhaps best embodied by the quantum transport simulation open source library Kwant [2]. Such software is becoming more and more accessible and aims to relieve users from managing low level details (numerical resolution of equations, integration, book keeping, etc.) to let them focus on the theoretical problem. However, significant bottlenecks remain.

The quantum-electrostatic problem

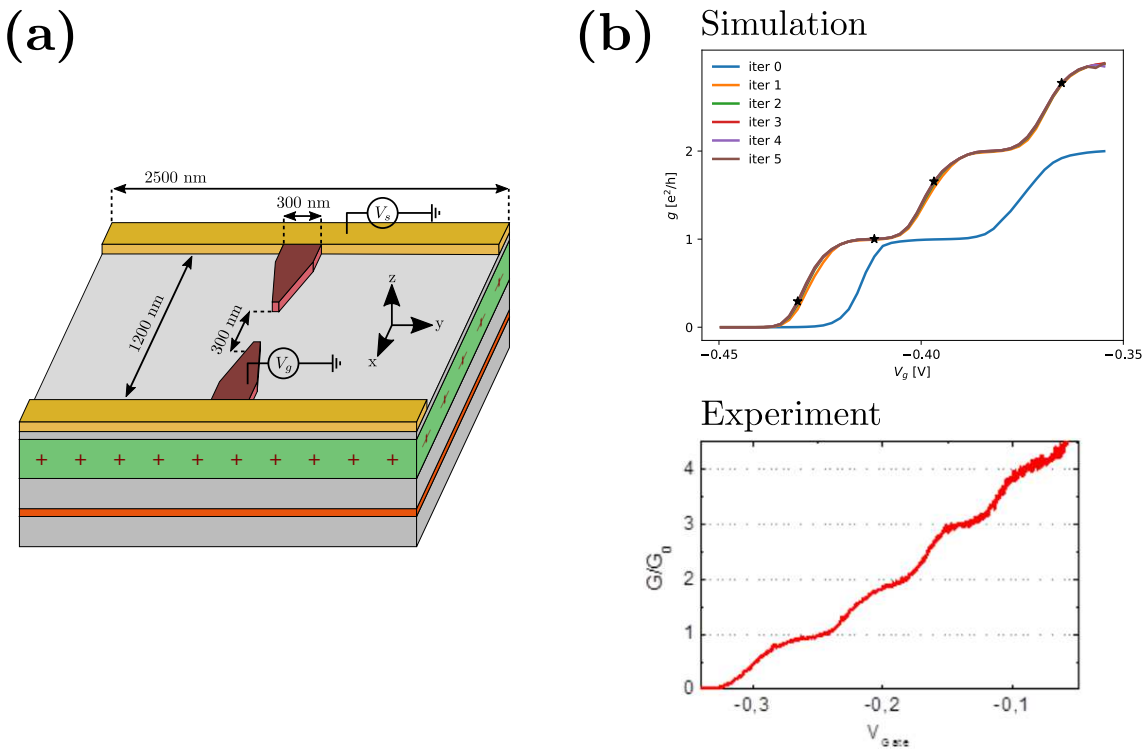

Figure 1: An example of a nanoelectronic system: a quantum point contact (QPC). (a) Schema of a typical experimental device: quantum gates on top of an electron gas wire create a constriction comparable to the Fermi wave length of the gas. (b) Quantized conductance of the QPC as a function of the gate voltage. (top) Simulations: the iteration 5 is the final result. (bottom) Experiments in a similar geometry (from [1]).

One bottleneck for the simulation of quantum systems, the focus of this thesis, is associated with the interplay between the electrostatics and the quantum kinetic energy. We call it here the quantum-electrostatic problem. One of the reasons that makes this problem so difficult is associated with the presence of two very different energy scales. On one hand the different band offsets lie in the 1 eV range (this is also the typical voltage that one must apply on electrostatic gates to deplete an electron gas). On the other hand, the typical Fermi energy of a two-dimensional electron gas in an heterostructure (2DEG) lies in the 1 meV range. Solving such a multi-scale problem is not an easy task as it means that to obtain precision of the order of 10 μeV one needs to resolve five orders of magnitude. However, as we will see in this thesis, solving the quantum-electrostatic problem is a prerequisite for the development of quantum technologies such as quantum dot based localized qubits or flying qubits. The goal of this thesis was to address this quantum-electrostatic problem by developing a new **general**, **precise** and **robust** algorithm.

The three keywords above are equally important: the method must be general and apply to a large spectrum of materials (semi-conducting heterostructures but

also nanowires, graphene like materials, topological materials) and geometries (hybrid systems, multi-terminal devices). The method must be robust, i.e. its convergence must not rely on the fine tuning of the parameters of the algorithm. Finally, it must also be precise as it needs to handle energy scale in the 10-100μeV range to possess true predictive power.

In its simplest mean field form, the quantum-electrostatic problem can be formulated as the solution of a self-consistent set of 3 equations: the Poisson equation, the Schrödinger equation and the density equation.

$$
\begin{aligned}
&(i) \qquad \Delta V(r) = \frac{e}{\epsilon} n(r) \\
&(ii) \qquad (H + V(r))\, \psi(r) = E\psi(r) \\
&(iii) \qquad n(r) = \frac{1}{2\pi} \int \mathrm{dE}\ \psi(\mathrm{E})\, \mathrm{f(E)}
\end{aligned}
$$

(i) For a given electronic density $n(r)$ of electrons of charge e in an environment with permittivity ϵ, the solution of the Poisson equation provides the electrostatic potential $V(r)$. (ii) For a given electrostatic potential $V(r)$ and free particle Hamiltonian H, one can solve the Schrödinger equation and obtain the energy spectrum and wave functions $\psi(E)$. (iii) Statistical physics provides the last equation: filling up the states according to the Fermi distribution $f(E)$, one obtains the electronic density $n(r)$. This problem, hereafter referred as the (self-consistent) quantum-electrostatic problem is a central aspect of material science and quantum chemistry. It is in particular the central problem solved in density-functional theory calculations.

Historically, this problem was solved using iterative schemes: one calculates the potential from the density (electrostatic problem), then the density from the potential (quantum problem) and one iterates until convergence. Nowadays, most of the algorithms use various form of this iterative procedures, often combined with preconditioning and/or predictor/correctors approaches. These approaches can be very effective, for instance when the temperature is not too low or when the density of state is rather smooth. However, they also suffer from difficulties. They often require some manual fine tuning of various parameters to converge, or even require deep physical insight to build a good approximation of the result used to make the method convergent. In some cases, such as the quantum Hall physics that will be discussed in this thesis, they fail altogether. Here, we shall build an algorithm that is stable in these highly non-linear situations.

Outline of the thesis

This thesis presents the work published (or in the process of being published) in 4 articles [3–6] and is separated in two parts.

The first part is dedicated to the description of our new self-consistent algorithm and direct applications [3, 4]. We start by quickly introducing the problem and the different existing approaches. By using a simplified model that encompasses the principal difficulty for the convergence of self-consistent algorithms, we explain why these method might fail. We then move to the principal novelty and central point of this thesis: the adiabatic self-consistent solver. This new approach takes a novel perspective to the problem: instead of looking for self-consistency iteratively, we solve the self-consistency exactly for an approximate problem. The approximate problem is already a very good approximation of the exact one and it can itself be improved iteratively until it is arbitrarily close of the exact problem. The chief advantage of this point of view is that the self-consistent approximate problem can be solved to arbitrary precision at no significant computational cost; its solution is provably intrinsically convergent. Thus we first explain how to construct this approximated problem (adiabatic self-consistent problem). As a second step, we describe how to relax this approximation in order to obtain the final problem and its solution. Some particular tools needed in order to perform these two steps are introduced. To conclude this first part, we illustrate our algorithm with two physical examples. First we calculate the density and potential in a 3D quantum point contact (see Fig. 1) and use these results to calculate interesting transport properties of this system, which can be either compared to experiments, or used to develop new theories.

We were also able to apply our algorithm to the system presented in Fig. 2 (a). It consists of an infinite system invariant in the y-direction: a two dimensional electron gas is confined by two gates on a wire like geometry and submitted to a constant magnetic field in the z-direction. As we stated, the highly non-linear density of state created by the large magnetic field makes it a particularly difficult problem to solve with usual iterative methods. However, our method was specially designed for such non-linearities. To our knowledge, this wrok presents the first of such fully self-consistent calculations. This system allows us to study an old problem, namely how does one transition between the zero field limit (where clear conductance channels exist and are well defined by Landauer-Büttiker theory [7]) and the quantum Hall effect with compressible and incompressible stripes [8]. We show an example of the density as a function of the position and of the potential as a function of the momentum k in Fig. 2 (b). We were able to reproduce the compressible and incompressible stripes predicted by Chklovskii-Shklovskii-Glazman (CSG) [8] in the Thomas-Fermi approximation, but also to go beyond this approximation. As we will show latter on, by solving the real self-consistent problem, we predicted a new phase, intermediate between the Landauer-Büttiker and the CSG picture.

In the second part of this thesis, we focus on early calculations for a new type of quantum bits: the flying qubits [5, 6]. Let us stress here that the understanding of the self-consistent solver presented in Part I is not necessary to understand this second part. This mean the in practice the two parts of this thesis can be read independently from each other. We begin by replacing the flying qubit into its context, i.e. a flying qubit quantum computer. We then move to our final interest in

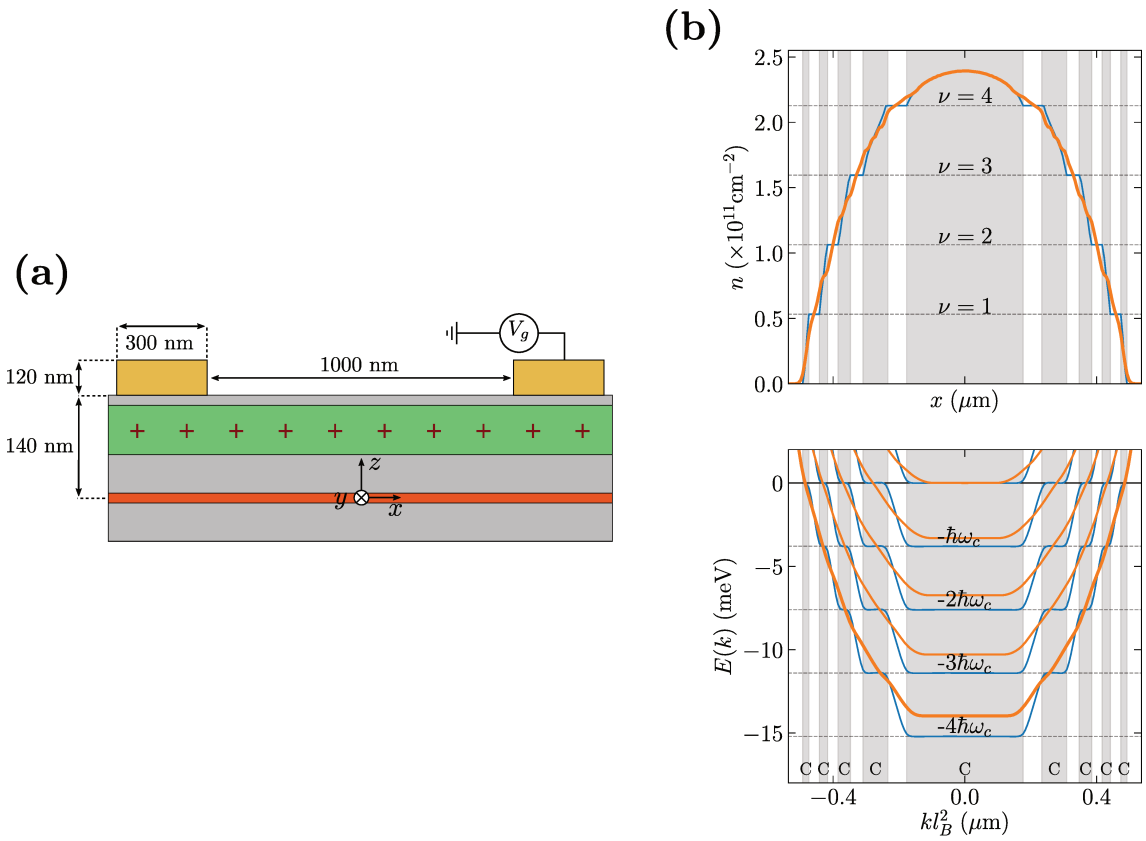

Figure 2: Observation of the quantum Hall effect regime. (a) Schema of the system: a quasi one-dimensional wire is created by two split gates situated above an electron gas submitted to a perpendicular magnetic field. The system is infinite along the y axis. (b) Example of our self consistent calculations: electronic density $n(x)$ (top) and band structure $E_n(k)$ (bottom) for a magnetic field $B = 2.2T$ and a confinement $V_g = -0.75$V. Blue lines: self-consistent calculations in the Thomas-Fermi approximation; orange lines: full self consistent solution of the quantum-Poisson problem. The gray "C" regions indicate the compressible stripes while the white regions are incompressible.

this thesis: the study of the velocity of surface plasmons (that can be used as flying qubits) as measured in an experiment by the group of C. Bäuerle in the Institut Neel of Grenoble. This experiment is schematized in Fig. 3 (a). A tension pulse is sent and made to propagate through a wire. The velocity of this pulse is then measured with a method that will be discussed later in chapter 6. We calculated the velocity of the collective excitations associated with the pulse. To do so we developed a technique that allows to recover analytically the dispersion relation found by the bozonization of the full many-body problem by using a multy-channel Luttinger liquid. This has the main advantage of allowing one to directly connect the plasmon velocity to the microscopic problem, without the need of any adjustable parameter. This allowed us to calculate this velocity as a function of the confinement gate voltage, as presented

in Fig. 3 (b) in three different cases (that will be discussed in section 6.2). One sees a very good agreement with experimental results, without adjustable parameter.

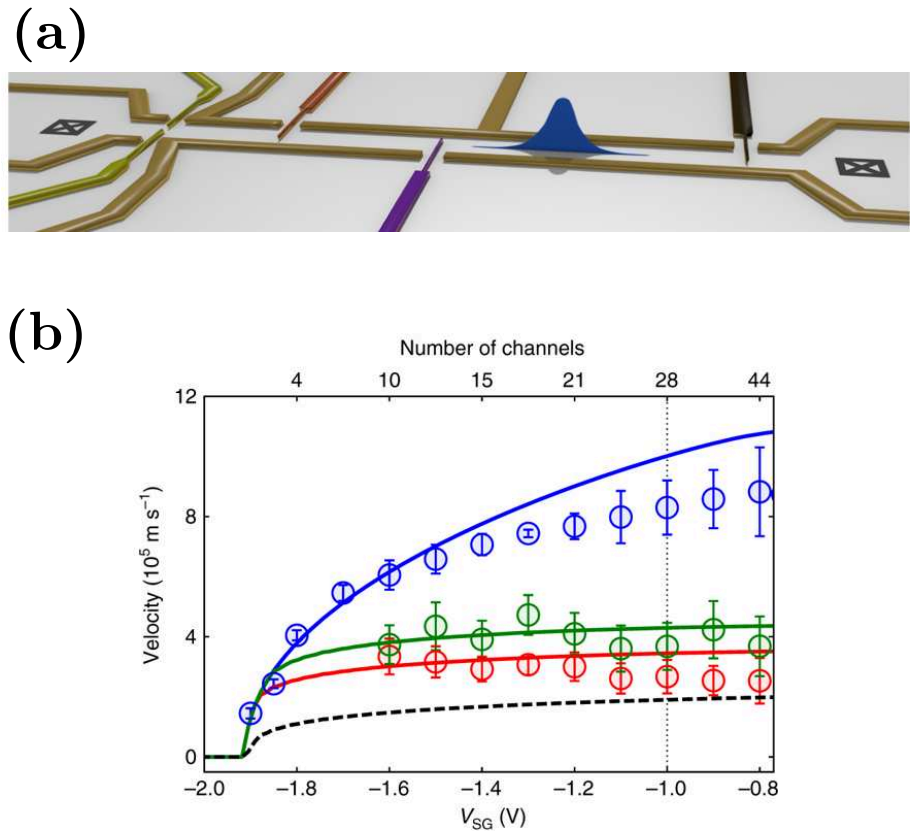

Figure 3: Measurement of the velocity of surface plasmons. (a) Schema of the experiment: a plasmon is sent in a wire and its velocity is measured. (b) Plasmon velocities as a function of the gate confinement. The circles are the experimental measurements with their error bars, the solid lines are the results from our parameter free theory calculations. The three different colors correspond to three different cases that will be discussed during this thesis. The dashed black lines shows the Fermi velocity calculated from the simulations.

Part I

The self-consistent quantum-electrostatic problem in highly non linear situation

SUMMARY OF PART I

In the first part of this thesis we describe our new self-consistent quantum-electrostatic solver and apply it to a quantum point contact geometry and a 2D wire in the quantum Hall regime. It consists mostly of the text from two currently unpublished articles [3, 4].

The adiabatic self-consistent algorithm: The quantum-electrostatic problem aims to describe the effect of mean field electrostatic interactions for a quantum system in an electrostatic environment. Let us assume a discrete quantum system described by a free particle with Hamiltonian H living in a potential $eU(\vec{r})$ and with wave functions $\psi(\vec{r})$. Its statistic is represented by a Fermi function $f(E)$. This system is immersed in an electrostatic environment described by a dielectric constant $\epsilon(\vec{r})$, constant charges (e.g. dopants) $n^{\mathrm{d}}(\vec{r})$ and some boundary conditions. The particle spatial density is $n(\vec{r})$. The quantum-electrostatic problem is defined by the three following equations: the Schrödinger equation, the integral over modes and the Poisson equation

$$(H + eU(i))\,\psi(i) = E\psi(\vec{r}) \tag{1}$$

$$n(\vec{r}) = \int \frac{dE}{2\pi}\,|\psi_E(\vec{r})|^2\,f(E) \tag{2}$$

$$\nabla \cdot (\epsilon(\vec{r})\nabla U(\vec{r})) = -e[n(\vec{r}) + n^{\mathrm{d}}(\vec{r})] \tag{3}$$

As we can see, this system of equations is non-local (coupled equations) but it can also be highly non-linear through equations 1.8 and 1.9. In order to solve this system, we introduce a local version of these equations that allows us to solve exactly the non-linearities. The full self-consistent solution is later obtained by reintroducing the non-locality iteratively.

Applications to the quantum Hall effect: Under high magnetic field, a Hall bar geometry exhibits quantized hall resistivity (and conductance). One usually explains it by using the Landau level picture, which doesn't include the effect of electrostatic interactions. Adding an approximated self-consistent treatment to this problem induces the creation of alternating compressible and incompressible strips of electrons [8]. A full self consistent treatment of the problem allows us to explore the crossover regime between no magnetic field and high magnetic field, which we find has properties of both regimes.

1

Introduction to the self-consistent quantum-electrostatic problem

In this chapter we will introduces the three equations that allow to define the quantum-electrostatic problem: the Schrödinger equation, the density equation and the Poisson equation. We will also introduce the notations that will be used throughout the whole part I of this thesis. In a second section, we describe the different approaches to the quantum-electrostatic problem that can be found in the literature.

1.1 Formulation of the self-consistent quantum-electrostatic problem

Let us formulate the quantum problem. We consider a non-interacting Hamiltonian H that describes a quantum conductor. It can consist of a scattering region connected to electrodes as in typical quantum transport problems [2], it can also describe bulk physics in 1 (infinite nanowires), 2 (two-dimensional electron gas, graphene) or 3 dimensions. All these systems share an important property. They are infinite, hence possess a proper density of states as opposed to a discrete spectrum. We suppose that H has been discretized onto sites i filled with the electronic gas. This discretization can be obtained in various ways. One can discretize an effective mass or $k \cdot p$ Hamiltonian; one can also construct a tight-binding model by projecting a microscopic Hamiltonian onto atomic orbitals. The electron gas is subject to an electrostatic potential $U(\vec{r})$ whose discretized form is written as a vector U of components U_i. The Schrödinger equation reads,

$$\sum_{j \in \mathcal{Q}} H_{ij}\psi_{\alpha E}(i) + U_i\psi_{\alpha E}(i) = E\psi_{\alpha E}(i) \tag{1.1}$$

where $\psi_{\alpha E}(i)$ is the electronic wave-function at energy E and the discrete index α labels the different bands (or propagating channels) of the problem. In the actual simulations performed in this thesis, $\psi_{\alpha E}(i)$ have been calculated with the Kwant package [2]. We call $\mathcal{Q}$ the set containing all the sites on which the quantum problem is defined. The number of electrons on site $i \in \mathcal{Q}$ is given by filling up the states with the Fermi distribution $f(E) = 1/[e^{E/(k_B T)} + 1]$ (hereafter the Fermi energy $E_F = 0$ is our reference energy),

$$n_i = \int dE \rho_i(E) f(E) \tag{1.2}$$

where we have introduced the local density of states (LDOS),

$$\rho_i(E) \equiv \frac{1}{2\pi} \sum_{\alpha} |\psi_{\alpha E}(i)|^2 \tag{1.3}$$

The last equation that closes the problem is the Poisson equation that reads,

$$\nabla \cdot (\epsilon(\vec{r}) \nabla U(\vec{r})) = \frac{-e}{\epsilon} [n(\vec{r}) + n^{\mathrm{d}}(\vec{r})] \tag{1.4}$$

where e is the electron charge, ϵ the local dielectric constant and $n(\vec{r})$ is the density of the electron gas. The $n^{\mathrm{d}}(\vec{r})$ term corresponds to any charge density located elsewhere in the system, e.g. dopants or charges trapped in an oxide. The Poisson equation is also specified by its boundary conditions. We shall use Neumann conditions at the boundary of the system as well as Dirichlet conditions at the electrostatic (metallic) gates. As for the quantum problem, we suppose that the Poisson equation has been discretized with some scheme such as a finite difference, finite element or (as we have done, see section 2.4) finite volume method. The discretization of the Poisson equation is rather straightforward and most approaches converge smoothly to the correct solution. The discretized Poisson equation takes the form,

$$\sum_{\nu \in \mathcal{P}} \Delta_{\mu\nu} U_\nu = n_\mu + n_\mu^{\mathrm{d}}. \tag{1.5}$$

We call $\mathcal{P}$ the set containing all sites of the system on which the Poisson equation is defined. We emphasize that the quantum problem is defined on a subset of the electrostatic problem, i.e. $\mathcal{Q} \subset \mathcal{P}$. The set $\mathcal{P} \setminus \mathcal{Q}$ contains regions with dielectric materials, dopants or vacuum. We often use greek letters for sites $\mu \in \mathcal{P}$ and latin letter for sites $i \in \mathcal{Q}$. The problem of the (partial) ionization of the dopants is commonly addressed by supposing that they correspond to a certain number n_μ^0 of localized levels with degeneracy g and energy E_0 so that,

$$n_\mu^{\mathrm{d}} = \frac{n_\mu^0}{1 + g e^{\frac{U_\mu + E_0}{k_B T}}} \tag{1.6}$$

At very low temperature, the focus of this thesis, this equation can only have three solutions: the dopants are fully ionized $n_\mu^{\mathrm{d}} = n_\mu^0$; no dopants are ionized $n_\mu^{\mathrm{d}} = 0$; or

$U_\mu = -E_0$. In the first two regimes, Eq.(B.1) fixes the charge density in the Poisson equation. In the last one, the dopant layer acts as an effective electrostatic gate, i.e. as a Dirichlet boundary condition in the Poisson equation. For the problems studied here, we restrict ourselves to the experimentally relevant regime where the dopants are fully ionized. *A more detailed discussion about the dopants can be found in appendix B.*

The set of equations (1.1), (4.5), (1.3) and (1.5) forms the (discrete version of the) quantum electrostatic problem. Hereafter, its Full Self-Consistent solution is referred to as FSC .

In what follows, our approach will be illustrated with a two-dimensional electron gas (2DEG) formed at the interface between GaAs and GaAlAs. We model the 2DEG within the effective mass approximation by discretizing

$$\frac{1}{2m^\star}\left(i\hbar\vec{\nabla} - eA\right)^2\psi + eU(x,y)\psi = E\psi \tag{1.7}$$

on a regular grid using Peirls substitution. The vector potential $\vec{A}$ is taken in the Landau gauge associated with a perpendicular magnetic field $\vec{B} = \vec{\nabla}\times\vec{A}$. The effective mass $m^\star$ is set to $0.067\,m_e$. Furthermore, we assume the permittivity ϵ to be $\epsilon = 12\epsilon_0$ in the semi-conductors and a 2DEG density $n = 2.11\ \times 10^{11}\mathrm{cm}^{-2}$. The two geometries that will be considered are shown in Fig.4.1 (b) and (c).

1.2 Review of the different approaches

We present here the different existing methods for the resolution of the self-consistent quantum-electrostatic problem. To the exception of the predictor-corrector approach of [9], this re-traces in chronological order, our investigation to find a suitable method.

Direct methods

The Schrödinger-Poisson algorithm

The Schrödinger-Poisson algorithm is the simplest method to solve the quantum-electrostatic problem. However, there is no intrinsic reason for it to converge. It is still worth to be presented, as it allows to introduce some notations and better understand the self-consistent problem. Let us start by rewriting our system of equations

$$(H+V)\psi(E) = E\psi(E) \tag{1.8}$$

$$n = \frac{1}{2\pi}\int \mathrm{d}E|\psi(E)|^2 f(E) \tag{1.9}$$

$$\Delta V = n + n_0 \tag{1.10}$$

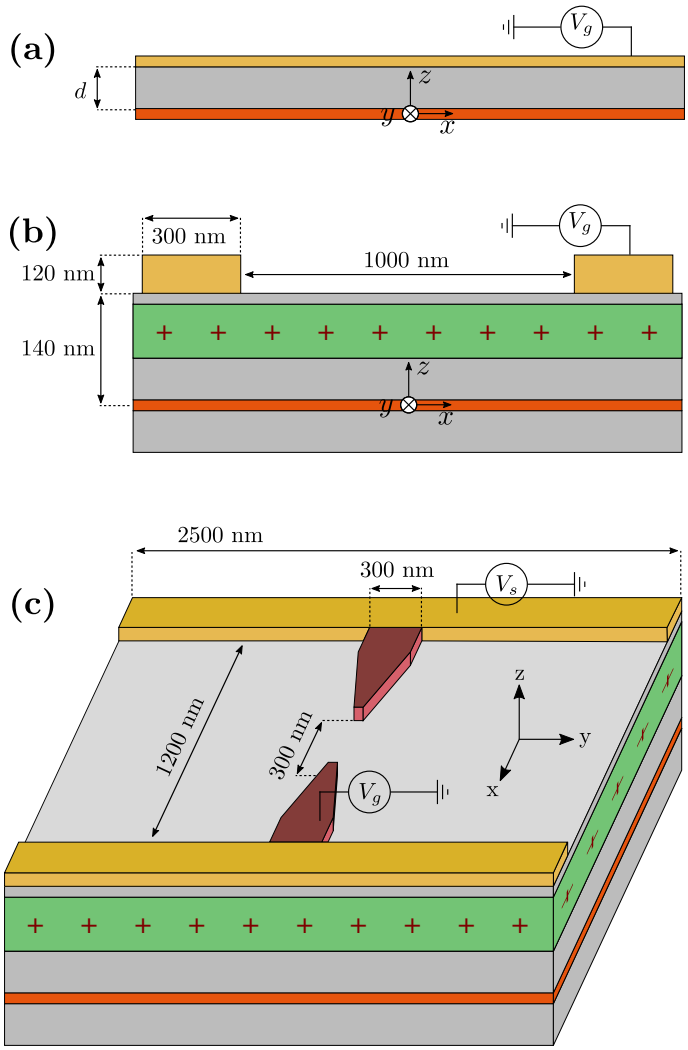

Figure 1.1: Schematic of the three systems considered in this part of the thesis. (a) infinite 2DEG along x and y directions. (b) quasi-one dimensional wire infinite along the y direction (c) Quantum Point Contact geometry. The red part corresponds to the 10 nm thick 2DEG. The green part corresponds to the doping region. The yellow and dark red part correspond to the electrostatic gates. The gray part to effective dielectrics (here GaAs and GaAlAs in practice).

where the space dependencies, the boundary conditions of the Poisson equation are omitted and the permittivity ϵ and charge e have been included inside the Δ operator. These equations have been discretized on sites, i.e. V and n are vectors, which components are the values of the potential and density on each sites. It is tempting to chain these equations.

The density n in equation 1.9 depends on the potential through equation 1.8. Formally, the effect of solving consecutively the two equations for a given potential V_{in} can be expressed with one operator. Thus we can rewrite equations 1.8 and 1.9 as

$$n \equiv Q(V_{in}) \tag{1.11}$$

where Q (Q as in Quantum) is an abstract function solving the Schrödinger equation for an electrostatic potential V_{in} and integrating it to get a density. Similarly, the Poisson equation can be solved for an input density n to obtain a potential V_{out}. The equation 1.10 can be rewritten with an abstract function P (P as in Poisson) and becomes

$$V_{out} \equiv P(n) \tag{1.12}$$

What remains is to define the composition of these two equations to get

$$V_{out} = P(Q(V_{in})) = (P \circ Q)(V_{in}) \tag{1.13}$$

From there we get that the self consistent solution $V^\star$ verifies $V^\star = (P \circ Q)(V^\star)$, which means that it is a fixed point of the operator $(P \circ Q)$. The self consistent density being obtained by a final call $n^\star = Q(V^\star)$. It is clear that the previous reasoning stays true if one choses to solve for the densities. One then just looks for the fixed point of $(Q \circ P)$. For simplicity we define the action of F such that $F = (P \circ Q)$. In term of algorithm the simplest solution is to just iteratively apply the operator . At iteration (i), $V^{(i+1)} = F(V^{(i)})$. One then iterates until some convergence criteria is reached, for example the average over space of the difference of potential $\overline{V^{(i-1)} - V^{(i)}}$. This was the first algorithm used historically [10–12].

Under-relaxation and mixing

However, these simple iteration do not always converge and in the cases where they can converge (typically if the density of state is close to linear) they are dependent on the initial conditions. Here we present two possible refinements to this technique that can help the convergence in some cases, but these methods still fail when the non linearities are too strong. The first refinement is to add a damping parameter to mix the previous iteration with the output. This should in principle reduce the risk of overshoot.

$$V^{(i+1)} = (1 - \alpha)V^{(i)} + \alpha F(V^{(i)}) \tag{1.14}$$

with α an external tuning parameter. This is the typical under-relaxation scheme used for example in [13].

This concept of keeping a memory of the history of the iterations and mixing them can be generalized. Let us once again redefine for simplicity the output of the calculation $F^{(i)} \equiv F(V^{(i)})$. One then construct the next iteration $V^{(i+1)}$ from the previous ones $\{V^{(i)}\}$ following $V^{(i+1)} = \mathcal{F}(\{V^{(i)}\}, \{F^{(i)}\})$, where $\mathcal{F}$ realizes the mixing. Among these mixing schemes is the Anderson mixing, which uses a linear mixing of previous iterations. Let β be a tunable mixing parameter and m the maximum number of iteration to mix, then the Anderson iteration in its simplest form is defined [14] by

$$\begin{aligned} \bar{V}^{(i)} &= \sum_{j=0}^{m} \theta_j^{(i)} V^{(i-j)} \\ \bar{F}^{(i)} &= \sum_{j=0}^{m} \theta_j^{(i)} F^{(i-j)} \\ V^{(i+1)} &= \bar{V}^{(i)} + \beta \bar{F}^{(i)} \end{aligned}$$

where optimal linear superposition at each iteration $\{\theta_j^{(i)}\}$ is found by minimizing a chosen error function. In practice one uses preferably a linear combination of the residuals $V^{(i)} - V^{(i-1)}$ (instead of a linear combination of the inputs $V^{(i)}$), but the technique is the same. One can see here that: (i) the final result is still dependent of the initial guess for the potential, and (ii), the methods suppose some linearity in order to converge. The Anderson mixing was the first technique that we tried try to use - following [15] - before developing our algorithm.

Indirect methods

Predictor-corrector

Predictor-corrector methods follow a different approach. The idea is to solve a simpler approximated problem (predictor), correct the approximation and update the problem (corrector), and then iterate on this loop until convergence. More precisely in the case of the self-consistent problem, this means solving an effective non linear Poisson equation $V = P(\tilde{n}[V])$, where $\tilde{n}[V]$ is a known functional. The $\tilde{n}(V)$ functional is supposed to be a good approximation of the real functional $Q(V)$ and should be easy to calculate. Once the non-linear Poisson equation is solved, the new effective $\tilde{n}(V)$ functional is calculated, and so on until convergence [9, 16–21]. An example of this method was used in [16] (which serves as a base for the self consistent solver NextNano [17]), where the calculation in the case of a 2DEG in a quasi 1D geometry was done. The density obtained through the quantum equations can be written as $n(\psi[V], E_F, x)$, where the dependency of the wave functions into

the potential is explicit. The approximated equation (Thomas-Fermi approximation) reads

$$\tilde{n}(\psi[V+\delta V], E_F, x) \sim n(\psi[V], E_F - \delta V(x), x) \tag{1.15}$$

The change of potential only changes the local Fermi energy but not the wave functions, which means that the $\psi[V]$ are only calculated once. The non-linear Poisson equation $V = P(\tilde{n}[V])$ is then solved with a gradient descent method: the Newton-Raphson method [22] with exact line-search [23]. Since the dependence in V is explicit, an exact gradient can be used. Once this equation is solved, giving a new potential $V^\star$, the new wave functions $\psi[V^\star]$ are calculated, to obtain a new effective $\tilde{n}$. Iteration are made until convergence. Once again, since this process does not exactly treat the non-linearities (this time in the non-linear Poisson equation), there is still a risk that the method does not converge in extreme situations.

Newton-Raphson with explicit gradient

Newton-Raphson and gradient methods in general aim to find the minimum of a function by following gradient (or Jacobian if the function is vectorial) [24] or an approximation of the gradient [25, 26]. This is in strong contrast with the mixing case, as it allows one to add the information of the knowledge of the gradient. As we will see later on, these methods are not perfect either and in particular behave badly when the function to minimize has strong non-linearities. Indeed by definition, since a the idea is to follow gradient lines into a minimum that one hopes to be a global minimum, the method supposes that the function to be minimized is locally linear. In general, one uses an approximation of the gradient similar to the predictor-corrector approach. It is also possible to calculate the gradient exactly, which is what we tried in the beginning of this work. However it is not a suitable approach since it is very expensive numerically, and also does not solve the convergence problem inherent to gradient methods.

Principle Let us set the problem. The previous fixed-point problem becomes finding the minimal value of the function $((P \circ Q)(V) - V)^2$. For simplicity we write now the discretized equations. Its Jacobian is

$$\frac{\partial \left((P \circ Q)_i(V) - V_i\right)^2}{\partial V_j} = 2 \sum_i \left((P \circ Q)_i(V) - V_i\right) \left(\frac{\partial (P \circ Q)_i}{\partial V_j} - \delta_{ij} \right) \tag{1.16}$$

the only unknown being the gradient of the composition, which can be expressed as a product of the gradient of the P and Q functions.

$$\frac{\partial (P \circ Q)_i}{\partial V_j} = \sum_k \frac{\partial P_i}{n_k} \left(\frac{\partial Q_k}{V_j} \right)^{-1}. \tag{1.17}$$

The derivative of the Poisson equation is just the Poisson green's function matrix defined in section 2.7. What remains is to compute how the density in site i is changed by a small perturbation of the potential at site j. To do so, we move into the Green's function formalism.

Lindhard function and Jacobian Suppose that our quantum system has a Hamiltonian H. For simplicity, we suppose that there is only one degree of freedom per site, but the following line of reasoning can be easily generalized. Its retarded Green's function between sites i and j at energy E is $g_{ij}(E) \equiv \lim_{\eta\to 0}[(E - H + i\eta)^{-1}]_{ij}$, where η is a regularization parameter that can be taken as small as possible. The density of the system can be expressed as

$$n_i \propto \int \mathrm{Im}\left(g_{ii}(E)\right) f(E)\, \mathrm{d}E + \mathcal{O}(\epsilon^2) \tag{1.18}$$

This means that we can get the derivative needed in 1.17 by simply derivating the Green's function. This calculation is far from trivial, thus we refer to appendix A for more details. In a nutshell one uses a Dyson equation to calculate the effect of a perturbation of the one-dimensional Bloch Green's function. We will just mention here that it can be calculated, but it is cumbersome and computationaly very expensive, which motivates our next step: use an approximated form of the Jacobian. This is similar to the approximation in the predictor-corrector approach, the wave functions are supposed to be independent of the potential, and we only derive the Fermi function. At low temperature, the derivative of the Fermi function behaves as a delta peak, which simply gives for the approximated Jacobian $\partial Q_i/\partial V_j \sim \delta_{ij} n_i(E_F)$. And for the full gradient of the quantum-electrostatic system

$$\frac{\partial(P \circ Q)_i}{\partial V_j} \sim G^P_{ij} \frac{1}{n_j(E_f)} \tag{1.19}$$

where G^P is the Green's function of the Poisson equation as defined in 2.7. Since only the Jacobian is approximated, this method does not need a correction step. However, it still fails when the density of state is non linear, as it is the case when the Fermi energy is close to a band opening, or when magnetic field is added. This calls for a new kind of method that treat the non-linearities with more care.

2

The local adiabatic problem approach

This chapter is the main part of this thesis, where we explain how we treat the self-consistent problem.

2.1 Role of non-linearities: a zero-dimensional toy model

Let us start with a very simple zero-dimensional problem that already provides key insights into the structure of the quantum-electrostatic problem. We consider an infinite homogeneous 2DEG characterized by a – spatially invariant – density n and an electric potential U. The system is sketched in Fig. 4.1a. An electrostatic gate placed at a distance d above the 2DEG forms a planar capacitor with the latter. The potential at the gate is the reference electric potential. The Poisson equation for this problem is readily solved: it is given by the solution of the infinite capacitor problem:

$$n = -\frac{\epsilon}{ed}U \tag{2.1}$$

The quantum problem is also readily solved. At zero temperature, n is given by the integrated density of states (ILDOS):

$$n = \int^{\mu} dE\rho(E) \tag{2.2}$$

where μ is the chemical potential. At equilibrium, the total *electrochemical* potential has a fixed value $V_g = U - \mu/e$. Up to a constant shift, V_g is the voltage difference applied between the 2DEG and the gate with e.g. a voltage generator. The two equations (2.1) and (2.2) form the set of equations to be solved self-consistently.

At zero magnetic field, the density of states (DOS) is constant $\rho = m^\star/(\pi\hbar^2)$ and these equations reduce to a trivial linear system of equations. The situation is more interesting when one switches a magnetic field B perpendicular to the 2DEG. Indeed, in presence of a magnetic field, the DOS consists of Dirac peaks at the positions of the Landau levels. The system reduces to

$$n = \frac{\epsilon}{ed}[-V_g - \mu/e] \tag{2.3}$$

and

$$n(\mu) = \frac{2eB}{h}\sum_{n=0}^{\infty}\theta(\mu - E_n) \tag{2.4}$$

with θ the Heaviside function, $E_n = \hbar\omega_c\left(n + \frac{1}{2}\right)$ the energies of the Landau levels and $\omega_c = eB/m^\star$ is the cyclotron frequency.

Fig. 2.1 shows the two functions n versus μ for the Poisson problem Eq.(2.3) (blue line) and quantum problem Eq.(2.4) (orange line). Solving the self-consistent equations amounts to finding the intersection point of these two curves. This is a trivial task where the accuracy of the solution increases exponentially with the number of evaluations of the two functions: one curve (Poisson) is strictly decreasing with μ while the other (Quantum) is strictly increasing so that a simple dissected scheme converges exponentially. *Note that the slope of the Poisson equation has been voluntarily exaggerated. A more realistic slope will be shown in Fig 2.4.*

Using this 0D model, one can also verify that iterative algorithms are extremely unstable in presence of magnetic field. For instance, the green arrows indicate a simple iterative scheme where one starts with a given chemical potential, calculates the density from the ILDOS, then gets the potential from Poisson. One applies the preceding sequence iteratively until convergence. The non-linearity of the ILDOS – which reflects the rapid variation of the DOS – makes this scheme divergent even with a good initial guess for the density. This is a rather extreme (yet physical) situation where the ILDOS has a highly non-linear staircase shape. Yet, even under more favorable conditions, the convergence of iterative schemes is seldom guaranteed and one has to rely on the fine-tuning of the parameters of the algorithm to obtain reliable results. These parameters characterize e.g. the learning rate or approximate solutions used by the algorithm to speed up convergence.

In the next two sections, we introduce our algorithm for solving the full (spatially dependent) problem. Conceptually, the idea is to reduce the global self-consistent problem to a set of approximate local self-consistent problems similar to Eq.(2.1) and Eq.(2.4).

2.2 The adiabatic self-consistent problem

The zero-dimensional model of Sec. 2.1 could be solved exactly – even in the presence of high non linearities – because finding its solution amounted to searching for the

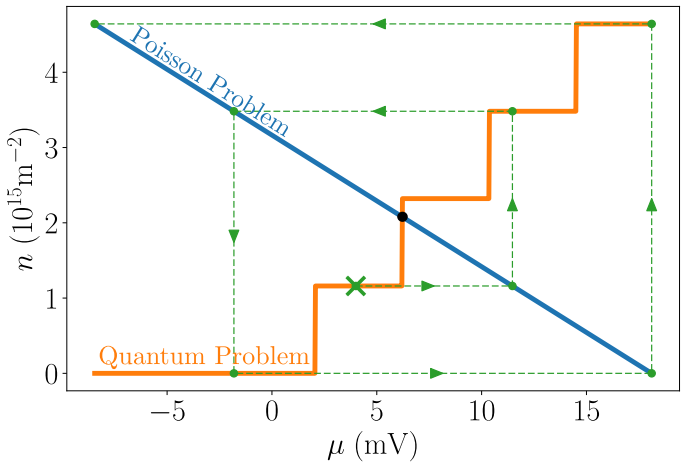

Figure 2.1: Toy model for the self-consistent quantum electrostatic problem in the planar capacitor 0D geometry of Fig. 4.1a. Orange line: solution of the quantum problem Eq.(2.4). Blue line: solution of the Poisson problem Eq.(2.1). Green arrows: example of a simple iterative solution of the problem which fails to converge. Geometric capacitance $C = 0.028$ F/m^2, dopant density $n_0 = 3.16 \times 10^{11}$cm^{-2}, magnetic field $B = 2.4$ T.

intersection between two curves. In this section we will introduce the adiabatic self-consistent problem. It is a local problem where on each site $i \in \mathcal{Q}$ one needs to solve an intersection problem similar to the one in Sec. 2.1. Hence, it can be easily solved numerically.

The adiabatic self-consistent problem is obtained by making two hypothesis. The first concerns the quantum problem and is called the quantum adiabatic approximation (QAA). The second is applied to the Poisson problem and is named the Poisson adiabatic approximation (PAA). The adiabatic self-consistent problem is similar, in spirit, to the approximate problem solved in density functional theory within the Local Density Approximation (LDA) [27]. The LDA becomes exact in the limit of an infinitely spatially smooth electronic density. Similarly, the adiabatic self-consistent problem becomes exact when the electric potential is infinitely smooth. However, the error of LDA cannot be controlled. In contrast, we can systematically improve the adiabatic self-consistent problem until its solution matches the FSC solution.

The adiabatic self-consistent problem will be our main tool to solve the self-consistent quantum electrostatic problem defined in Sec.1.1. In the current section, we show how to formulate and solve exactly the adiabatic self-consistent problem. In Sec.2.3, we will show how one can make "the adiabatic self-consistent problem" converge towards the FSC solution.

Quantum Adiabatic Approximation (QAA)

The quantum adiabatic approximation (QAA) maps the quantum problem onto a local problem. We consider an electric potential U_i defined on the quantum site i, with $i \in \mathcal{Q}$. We suppose that we have solved the Shcrödinger equation (1.1) for this potential and computed the LDOS $\rho_i(E)$ on each site i using Eq. (1.3). The density n_i is obtained by filling up the states according to Eq.(4.5). Now suppose that we introduce a perturbation δU. The electric potential becomes $U + \delta U$, i.e. $U_i \to U_i + \delta U_i$. One thus should recalculate $n_i[\delta U]$. In principle, this would imply resolving the Schrödringer equation for $U + \delta U$, which is a computationally expensive task. Also, the new value of $n_i[\delta U]$ depends on δU_j in a non local way ($j \neq i$). However, if δU is either small or has very smooth spatial variations, one can use the Quantum Adiabatic Approximation (QAA),

$$n_i[\delta U] \approx \int dE\ \rho_i(E) f(E + \delta U_i). \tag{2.5}$$

In the QAA, one needs not recalculate the LDOS. Eq.(2.5) is exact to first order in δU (small perturbation). It is also exact when δU is infinitely smooth (when δU_i does not depend on i, a global shift in energy does not modify the wave functions). We shall find empirically that the QAA is an excellent approximation for realistic systems. Indeed, effective electrostatic potentials *do* vary smoothly, the rapidly varying part of the electric potential at the atomic level being usually included in a renormalization of the effective parameters of the theory. Note that with our convention the electrochemical potential is set to zero so that a change of electric potential δU_i is equivalent to the opposite change in the local chemical potential, i.e. $\delta U_i + \delta \mu_i = 0$. The QAA approximation bears two important features: (i) it is a local equation on each site i and (ii) the knowledge of the LDOS is sufficient to calculate n_i for any variation δU.

In practice, we shall construct an interpolant of $\rho_i(E)$ in order to calculate the integral Eq.(2.5) for various δU_i. At zero temperature, Eq.(2.5) reduces to the integrated local density of states (ILDOS),

$$n_i[\delta \mu_i] \approx \int^{\delta \mu_i} dE\ \rho_i(E). \tag{2.6}$$

The shape of the LDOS often contains $1/\sqrt{E}$ singularities (no magnetic field) or Dirac functions $\delta(E)$ (Landau levels in presence of magnetic field). This is illustrated in Fig. 2.2 where we have plotted the functions LDOS and ILDOS versus energy for two magnitudes of the magnetic field. At low magnetic field the integration can be performed with quadrature techniques. At large magnetic field, however, a different approach is required to handle the presence of the Dirac peaks. This aspect is discussed in Sec. 2.5.

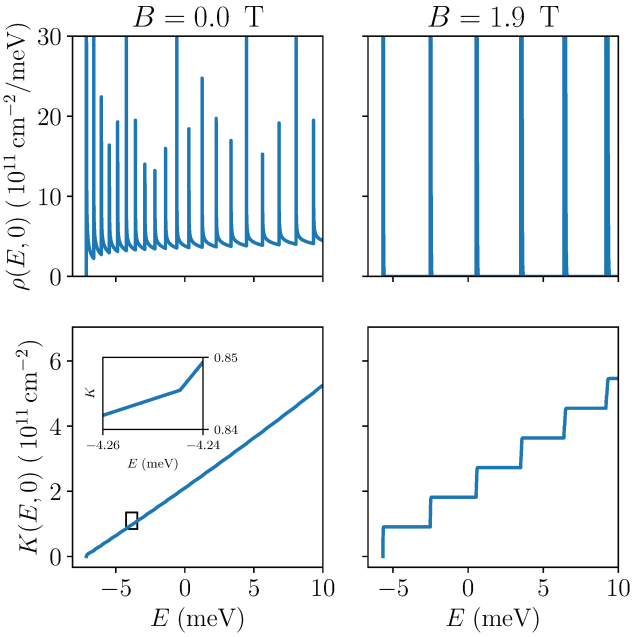

Figure 2.2: Top: Local density of states $\rho_i(E)$ (LDOS) at the center of the gas ($x = 0$) at $B = 0$ T (left) and at $B = 1.86$ T (right) as a function of energy for the geometry of Fig. 4.1. Bottom: Integral of the local density of states (ILDOS) for the same magnetic fields. The gate voltage is $V_G = -1$ V. Inset: zoom of the main curve showing the cusp created by the $1/\sqrt{E}$ singularity of the DOS

Poisson Adiabatic Approximation (PAA)

The Poisson adiabatic approximation (PAA) maps the Poisson problem onto a local problem. The exact solution of the Poisson problem can be formally written as

$$U_i = \sum_j G_{ij} n_j + U_i^s \tag{2.7}$$

with $i, j \in \mathcal{Q}$. The matrix G is (a discretized version) of the Green function of the Poisson equation and U_i^s accounts for the source terms in the problem. It is important to note that Eq.(2.7) is defined only on the sites $i \in \mathcal{Q}$ where the quantum system lies, i.e. the extra sites $\mu \in \mathcal{P} \setminus \mathcal{Q}$ have been integrated out. In the continuum G is essentially $e^2/(4\pi\epsilon|r - r'|)$ although it may decay faster at long distances due to the screening effect of the electrostatic gates. We invert the matrix G and get,

$$n_i = \sum_{j \in \mathcal{Q}} C_{ij} U_j + n_i^s \tag{2.8}$$

where $C = G^{-1}$ is the capacitance matrix and $n^s = -CU^s$ accounts for the source terms. Eq.(2.8) has a very similar structure to the Poisson equation (2.1). However, it is only defined on the site $i \in \mathcal{Q}$. The C matrix is a central object of our approach. How to compute its relevant elements will be explained in Sec.2.4.

Fig. 2.3 shows the elements of the G and C matrices calculated for the geometry in Fig. 4.1b. As expected, the Green function G is highly non local: a change in n_i has an effect on U_j over a large distance. In sharp contrast, the C matrix is extremely local. Indeed, to a good approximation, the C matrix is the discretized version of the Laplacian, hence a local operator. This statement would be mathematically exact if we had not integrated out any sites, i.e. $\mathcal{Q} = \mathcal{P}$. The locality of the capacitance matrix C is the central property on which PAA is based. In the Poisson Adiabatic Approximation (PAA), we assume that the change δU_i is smooth so that we can approximate Eq.(2.8) with,

$$n_i[U + \delta U] \approx n_i[U] + C_i \delta U_i \tag{2.9}$$

where the local capacitance C_i is defined as,

$$C_i = \sum_j C_{ij} \tag{2.10}$$

Eq.(2.9) is exact in the limit where δU_i can be considered as constant on the scale of the support of C. As we shall see, PAA is generally an excellent approximation, with a small caveat explained in Sec. 2.3.

Solving the local self-consistent problems

Together, Eq.(2.5) and (2.9) form a local self-consistent problem on every site $i \in \mathcal{Q}$. This is the adiabatic self-consistent problem. Solving this set of equation simply

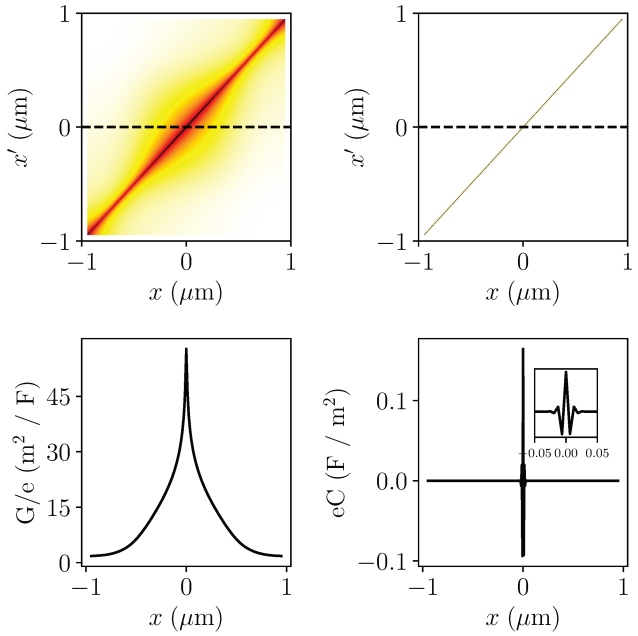

Figure 2.3: Green's function G (left) and Capacitance matrix C (right) for the geometry shown in Fig. 4.1b. Top panels: 2D colormaps of $G_{xx'}$ (left) and $C_{xx'}$ (right). Lower panels: 1D cuts $G_{x,0}$ (left) and $C_{x,0}$ (right). Inset: zoom of the lower right panel. The C matrix is very local while the G matrix is not.

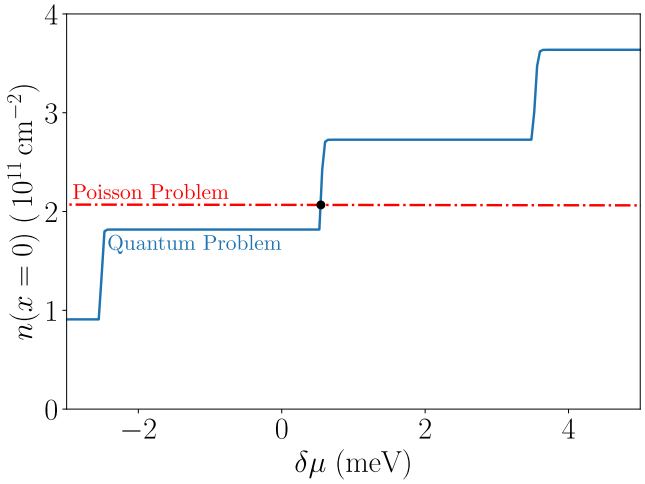

Figure 2.4: Solution of the local self-consistent problem at $x = 0$, $B = 1.87\,T$ and with $V_G = -1$ V for the geometry of Fig. 4.1b. Blue line: ILDOS Eq.(2.6) versus chemical potential $\delta\mu$. Orange dashed line: local Poisson problem Eq.(2.9) versus $\delta\mu = -\delta U$. The intersection of the two curves is the solution of the local self-consistent problem.

amounts to finding the intersection of the Poisson and Quantum curves for every site, which can be done extremely efficiently. More importantly, the solution always exist and can always be found with exponential accuracy. In practice, any one-dimensional root finding routine works very efficiently.

Fig. 2.4 shows an example of the adiabatic self-consistent problem for a given site $i \in \mathcal{Q}$ where we have used the bulk DOS Eq.(2.4) as the LDOS. This problem and the zero-dimensional model of Sec. 2.1 are solved in a similar way. The only difference is that in the adiabatic self-consistent problem a different intersection must be found for each site $i \in \mathcal{Q}$. Observe that the electrostatic Eq.2.9 is almost an horizontal line, i.e. the density depends only weakly on the potential on this scale. This is a consequence of the electrostatic energy being much larger than the kinetic energy. A direct consequence is that the convergence of the density is achieved very rapidly, before one obtains the converged potential. A secondary consequence is that one should chiefly monitor the convergence of the potential, a more sensitive quantity than the density.

2.3 Relaxing the Adiabatic self-consistent problem

The PAA and QAA approximations have been designed so that the initial global self consistent problem can be reduced to a set of local problems that can be exactly and efficiently solved. In this section we propose an algorithm to relax these two

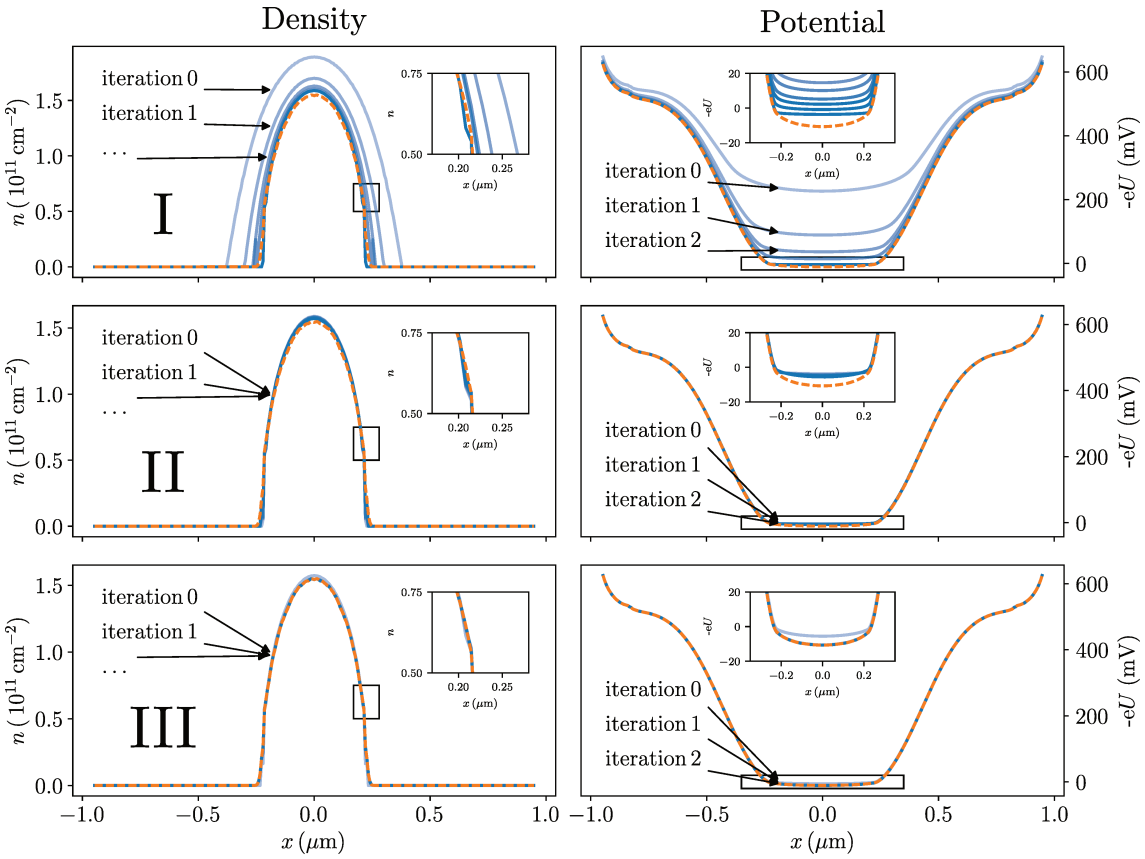

Figure 2.5: Relaxation of the different approximations for the geometry of Fig. 4.1b. Left panels: density versus position. Right panels: electric potential versus position. Top panels: step I (excluding the sites with zero density). Middle panel: step II (relaxing the Poisson adiabatic approximation). Bottom panels: step III (relaxing the quantum adiabatic approximation). Blue lines: various iterations. Thick orange dashed line: final converged result (FSC). Insets: zooms of the main curves.

approximations, and thus obtain the FSC solution of the full quantum-electrostatic problem. The convergence towards the exact solution is achieved by iteratively improving the local problems until they match the global one. Although this relaxation is iterative, one iterates on the adiabatic self-consistent *problem*, in contrast to iterating on the *solution* as is usually done. In practice, we observe extremely fast convergence, typically in a single iteration of the quantum problem (the computational bottleneck calculation). The relaxation of PAA and QAA is done using three relaxation steps, I, II and III, which will be now detailed.

I. In Sec. 2.2 we have argued that the Poisson approximation is generally accurate. There is, nonetheless, a caveat to this argument. In fact, the PAA is of very high accuracy inside the electronic gas where screening occurs. However, in regions where the electronic gas has been depleted ($n_i = 0$), there is no screening, hence the electric potential changes abruptly and the PAA fails. This problem is readily solved however: since we already know the density on these sites (it is zero), we do not need to solve a local adiabatic problem there. The first type of relaxation step, i.e. Step I, thus aims to detect such regions and remove them from the list of sites where the local self consistent problem is solved. More precisely, we define the set $\mathcal{Q}' \subset \mathcal{Q}$ of sites where the density is non-zero and restrict the adiabatic self-consistent problem to $\mathcal{Q}'$. This has a strong influence on the electrostatic since the local capacitances C_i strongly depend on the partitioning of $\mathcal{Q}$ into $\mathcal{Q}'$ and $\mathcal{Q} \setminus \mathcal{Q}'$. Indeed, the PAA approximation is no longer performed on the sites belonging to $\mathcal{Q} \setminus \mathcal{Q}'$, their electrostatic is treated exactly. Hence the solution of the new adiabatic self-consistent problem on $\mathcal{Q}'$ results in an updated solution. Note that in the new solution some sites i may become depleted and hence the set $\mathcal{Q}'$ must be updated again. This is achieved by performing step I once again. The procedure is repeated a few times until the set $\mathcal{Q}'$ no longer evolves. We emphasize that only a finite number of step I iterations are needed to obtain the final set $\mathcal{Q}'$ (typically less than 5). These iterations are computationally non-demanding since the same LDOS is used for all of them. As we shall see, the electronic density obtained after completion of these steps I is almost indistinguishable from the FSC solution of the exact problem.

II. In order to relax PAA on the remaining sites $i \in \mathcal{Q}'$, we introduce a second type of relaxation step, step II. This is achieved by solving the exact Poisson problem: given a potential U (such as the one that we obtained at the end of the steps I), one calculates the exact density $n = CU$, solution of the Poisson equation. This new density is the new source term $n_i[U_i]$ in Eq.(2.9). Once Eq.(2.9) has been updated, we can solve the corresponding adiabatic self-consistent problem. Step II can be repeated until convergence. Note that, in practice, we do not perform a matrix vector product $n = CU$. Instead, we solve the Mixed Poisson problem as explained below in Sec. 2.4. Typically very precise convergence is obtained within one or two step II iterations.

III. In order to relax the QAA on the sites $i \in \mathcal{Q}'$, we introduce a third type of relaxation step, step III. This is achieved by re-solving the quantum problem to update the LDOS. The new LDOS is integrated to update Eq.(2.5). Once Eq.(2.5) has been updated, we can solve the corresponding adiabatic self-consistent problem.

Typically, we find that performing a single step III is sufficient. Calculating the ILDOS is the computational bottleneck of the calculation.

We emphasize that the relaxation steps I, II and III can, in principle, be performed in any order or even simultaneously. The most important one is step I, which is also the cheapest computationally. Hence, it should be performed first until convergence. Step III is far more computationally demanding than I or II since it implies solving the quantum problem. Hence, to optimize the number of step III iterations, it is efficient to first achieve convergence of step II. After each step III iteration, several step II iterations should be performed. Also, after each step III iteration, we reset step I, i.e. set $\mathcal{Q}' \equiv \mathcal{Q}$ and perform the step I relaxation until convergence. This is usually not needed but guarantees that the algorithm does not get trapped in a wrong $\mathcal{Q}'$ partition. After this sequence of relaxation steps, the final (supposedly exact) result is the FSC (Full Self-Consistent) solution to the quantum-electrostatic problem and is free from any initial approximations. We note that we have used plain iteration steps II and III. The relaxation could possibly be further accelerated by using mixing schemes such as Anderson or Broyden algorithms.

Fig. 2.5 shows an example of performing several relaxation step I (upper panels), II (central panels) and III (lower panels) for the geometry of Fig. 4.1b. The left panels show the density while the right panels show the potential. After each step III, a few steps II are performed. In most panels the curves for various iterations are almost superposed. The insets show zooms of the main curves which are also mostly superposed. The final converged FSC result is shown by a dashed orange curve. For the initial LDOS, we used the bulk (constant) DOS that is known analytically. In this case, it does not depend on energy. As anticipated, we observe that the initial solution of the adiabatic self-consistent problem is of bad quality, an indication that the PAA is a bad approximation in the depleted regions where the electric potential varies abruptly. However, after the vanishing density sites have been removed from the set of active sites $\mathcal{Q}'$ (after convergence of the steps I cf. upper panels), we find that the density is almost indistinguishable from the final converged FSC result. We still observe a small (a couple of mV) discrepancy in the electric potential (see the zoom of the upper right panel). While this discrepancy is small on the global scale of Fig. 2.5, it is still important for quantitative transport calculations (cf. Sec.3). The central panels illustrate the evolution of the solution upon performing several steps II. One observes that by relaxing the PAA, the results only change very slightly. This confirms that the PAA is an extremely good approximation inside the 2DEG. Since the bulk DOS was initially used, the results obtained after the steps II correspond to a self-consistent Thomas-Fermi calculation. The last (lower) panels show the application of the step III where the ILDOS is recalculated to relax the QAA. We find that one unique step is sufficient to obtain a fully converged result.

2.4 A mixed Neuman-Dirichlet Poisson solver

In usual electrostatic problems, one calculates some elements of the Green's function G. Indeed, in the standard Poison problem one uses the density n_μ as an input and calculates the potential $U = Gn$ as an output. The Poisson problems that are repeatedly solved in our algorithm, however, involve elements of the *capacitance* matrix C. In this section, we explain how to formulate and solve a generalized Poisson problem that provides direct access to the relevant elements of the capacitance matrix C.

Problem formulation

We begin by sorting the sites of the set $\mathcal{P} = \mathcal{D} \cup \mathcal{N}$ into two categories that we call "Dirichlet" sites (set $\mathcal{D}$) and "Neumann sites" (set $\mathcal{N}$) in reference to the corresponding boundary conditions. The set $\mathcal{N}$ contains the sites where the density is an input and we want to calculate the potential. Therefore, $\mathcal{N}$ contains all the sites inside the dielectric (zero density) as well as the sites with dopants (known density). The depleted sites of the quantum problem $\mathcal{Q} \setminus \mathcal{Q}'$ are also elements of $\mathcal{N}$. The set $\mathcal{D}$ contains the sites where the potential is an input and we want to calculate the density. Hence, $\mathcal{D}$ contains all the sites where the adiabatic self-consistent problem is defined $\mathcal{Q}' \subset \mathcal{D}$. Moreover, the sites that correspond to electrostatic gates (standard Dirichlet boundary conditions) also belong to $\mathcal{D}$.

Writing Eq.(1.5) in a block form for the Dirichlet (D) and Neumann (N) blocks, it reads,

$$\begin{bmatrix} \Delta_{NN} & \Delta_{ND} \\ \Delta_{DN} & \Delta_{DD} \end{bmatrix} \cdot \begin{bmatrix} U_N \\ U_D \end{bmatrix} = \begin{bmatrix} n_N \\ n_D \end{bmatrix} \tag{2.11}$$

In the above equation n_N and U_D are the known inputs of the problem while n_D and U_N are yet to be determined. After reshuffling the above equation, we arrive at the "mixed Neumann-Dirichlet Poisson problem",

$$\begin{bmatrix} \Delta_{NN} & 0 \\ \Delta_{DN} & -\mathbb{1} \end{bmatrix} \cdot \begin{bmatrix} U_N \\ n_D \end{bmatrix} = \begin{bmatrix} \mathbb{1} & -\Delta_{ND} \\ 0 & -\Delta_{DD} \end{bmatrix} \cdot \begin{bmatrix} n_N \\ U_D \end{bmatrix} \tag{2.12}$$

Solving this problem amounts to solving a set of linear equations with the right-hand side as a source term. This is readily achieved with sparse solvers such as the MUMPS package. Two different quantities must be calculated with the mixed Poisson solver, respectively the source term $n_i[U]$ and the local capacitance C_i.

To calculate $n_i[U]$, one sets n_N and U_D to their known values. The density n_N is zero except on sites where there are dopants. U_D is the current value of the potential for sites $i \in \mathcal{Q}'$. U_D is equal to the input gate potential at the electrostatic gates.

To calculate the vector C_i for $i \in \mathcal{Q}'$, one sets $n_N = 0$ and $U_D = 0$ except for sites $i \in \mathcal{Q}'$ where $U_i = 1$. The output vector n_D (projected on $\mathcal{Q}'$) contains the needed elements $C_i = (n_D)_i$.

Finite volume discretization

In order to obtain the $\Delta_{\mu\nu}$ matrix from the continuum problem, a discretization scheme of some sort must be used. Many approaches could be employed, including finite-difference and finite-elements methods. Here we use a finite-volume approach that has the advantage of solving a problem which is physically meaningful for any finite value of the discretization length a. In particular, this method has the advantage of respecting charge conservation inside the Neumann sites independently of the discretization length a. As the quantum-electrostatic is extremely sensitive to any variation of the charge, strict charge conservation is very important to ensure a fast convergence of the results with respect to a.

One starts by meshing the simulation box to obtain the $\mathcal{P}$ sites. one includes all the sites $\mathcal{Q}$ of the quantum system (this important to avoid any interpolation difficulty between the quantum and Poisson problem). Then one adds a regular grid around the quantum sites. This grid matches the lattice of the quantum system to avoid introducing artificial noise due to lattice mismatch. Another grid with a larger value of a can be used far away from the quantum system.

In a second step one construct the Voronoi cells associated with our mesh using the Qhull algorithm [28]. An example of the final discretized geometry with the Voronoi cells is shown in Fig. 2.6 for the system of Fig. 4.1b. for clarity Fig. 2.6 shows very few cells. Actual calculations were performed with typically 10^4 sites in 2D and 10^6 sites in 3D.

To calculate the $\Delta_{\mu\nu}$ matrix, we apply the Gauss theorem to each volume cell. One obtains, without approximation,

$$n_\mu = \sum_\nu \Phi_{\mu\nu} \tag{2.13}$$

with n_μ the total charge inside the cell.

$$\Phi_{\mu\nu} = \int_{S_{\mu\nu}} \epsilon(\vec{r})\vec{E}(\vec{r}).\vec{n}dS \tag{2.14}$$

is the flux of the electric field $\vec{E}$ through the planar surface $S_{\mu\nu}$ that connects cell μ with cell ν ($\vec{n}$ is the unit vector point perpendicular to this surface). In the electrostatic limit, the electric field is irrotational which reads,

$$\oint_{\vec{r}_\mu}^{\vec{r}_\nu} d\vec{r}.\vec{E} = U_\mu - U_\nu \tag{2.15}$$

To close our system of equations, we suppose that the electric field varies smoothly on the scales of the Voronoi cell. Up to $O(a^3)$ corrections one gets:

$$\Phi_{\mu\nu} = \frac{\epsilon_{\mu\nu} S_{\mu\nu}}{d_{\mu\nu}} (U_\mu - U_\nu) \tag{2.16}$$

where $d_{\mu\nu}$ is the distance between the center of the two cells and $\epsilon_{\mu\nu} = 2\epsilon_\mu\epsilon_\nu/(\epsilon_\mu+\epsilon_\nu)$ is an averaged dielectric constant obtained from the conservation of the flux through the surface. Together, Eq.(2.13) and Eq.2.16 define the $\Delta_{\mu\nu}$ matrix.

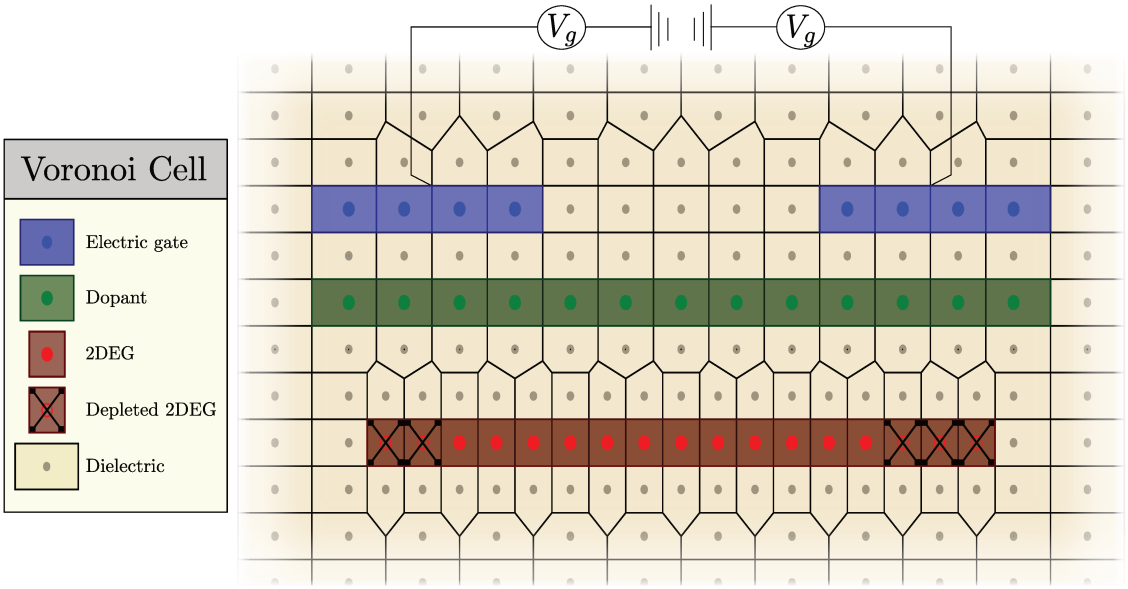

Figure 2.6: sketch of the discretized Poisson problem for the geometry of Fig. 4.1b. The 2DEG and depleted 2DEG Voronoi cells belong to the sites in $\mathcal{Q}'$ and $\mathcal{Q} \setminus \mathcal{Q}'$ respectively. The dopant and dielectric cells are Neumann sites, i.e. belong to $\mathcal{N} \subset \mathcal{P}$. The cells forming the electric gate belong to $\mathcal{D} \subset \mathcal{P}$.

2.5 Calculation of the integrated local density of states

Solving the local quantum problem obtained with the Quantum adiabatic approximation implies calculating the ILDOS as a function of the chemical potential for every site of the quantum system $\mathcal{Q}$. The numerical integration of the LDOS, in some situations, can be difficult. Indeed, one example is shown in Fig. 2.2. There, the LDOS has singularities at zero fields and Dirac functions in presence of magnetic field. A direct calculation of the integral of Dirac functions using quadrature rules is bound to failure. In this section we explain how to circumvent this problem using quadrature methods over momentum instead of energy. We note that a popular approach to calculate the density uses complex contour integration with, for instance, the so-called Ozaki contour [29]. Although such method works very well at equilibrium (but not out-of-equilibrium), it is unsuitable for our purpose as it provides the density for a single value of the chemical potential. Indeed, we require the full function ILDOS versus chemical potential to solve the adiabatic self-consistent problems.

For simplicity, we restrict ourselves to calculations at zero temperature (the method is readily extended to arbitrary temperatures). The ILDOS on site $i \in \mathcal{Q}$ is defined as

$$n_i[\mu] = \int^{\mu} dE\ \rho_i(E) \tag{2.17}$$

where the lower bound of the integral is the beginning of the spectrum. The LDOS $\rho_i(E)$ is itself defined in terms of the wave-functions of the system with momentum k as,

$$\rho_i(E) = \int_{-\pi}^{\pi} \frac{dk}{2\pi} |\psi_{\alpha k}(i)|^2 \delta[E - E_\alpha(k)] \tag{2.18}$$

where $E_\alpha(k)$ is the dispersion relation of the corresponding band. The above expression is valid for translational invariant systems such as the geometry of Fig. 4.1b. For more general geometries, such as Fig. 4.1c, the momentum k is to be understood as the momentum in the semi-infinite electrodes. To calculate the ILDOS, we insert Eq.(2.18) into Eq.(2.17) and invert the order of the integrals. The integral over energy can be performed exactly and we arrive at,

$$n_i[\mu] = \int_{-\pi}^{\pi} \frac{dk}{2\pi} \sum_\alpha |\psi_{\alpha k}(i)|^2 \theta[\mu - E_\alpha(k)] \tag{2.19}$$

where $\theta(x)$ is the Heaviside function. Eq.(2.19) can now be evaluated by standard quadrature techniques that sample the k points. One can readily understand why this change of variable $E = E_\alpha(k)$ is particularly advantageous in the case of the quantum Hall effect. There, the dispersion relation $E_\alpha(k)$ is extremely flat due to the presence of the dispersive-less Landau levels. By sampling the E space, one is almost certain not to sample correctly these Landau levels. By sampling the k space, however, the points get automatically positioned where they are needed. Furthermore, the integral for many values of μ is done simultaneously at no additional computational cost. *More details about the integration techniques that we used can be found in appendix C.*

2.6 Conclusion

We have developed a new algorithm that can solve the quantum-electrostatic problem even in highly non-linear situations. Perhaps more importantly, the algorithm converges extremely rapidly without requiring any parameter tunning. This is true even at zero temperature and/or under high magnetic field. This opens the possibility for direct and detailed comparisons between experiments and simulations, a prerequisite for using simulations at the design stage of quantum devices.

3

Applications to a quantum point contact

We now turn to a first application, the study of the quantum point contact (QPC) geometry of Fig.4.1c. QPCs are important historically as the first device where conductance quantization was observed [30, 31]. They can be considered as the electronic equivalent of the optical beam splitter and as such play a central role in electronic quantum optics [32].

Fig.3.1 shows colormaps of the density and electric potential around the QPC for different values of the confining gate potential V_g applied to the QPC. These FSC results correspond to a 2D quantum problem with around 10^4 active quantum sites ($\mathcal{Q}$ sites) embedded in a 3D Poisson problem with around 10^6 electrostatic sites ($\mathcal{P}$ sites). Fig.3.2 shows cuts of the colormap at various positions. The electron gas is present in regions where the electric potential is negative. Typical values of the potential in these regions is of a few mV. Convergence with an accuracy better than 10μV is needed around the QPC to obtain reliable results for transport calculations.

We end this section with the calculation of the conductance versus gate voltage, the actual observable measured in most experiments. The results are shown in Fig.3.3 for various iterations of step III. Each iteration corresponds to a new calculation of the ILDOS. Iteration 0 is the Thomas-Fermi approximation. It provides an accurate density but the $g(V_g)$ curve is not quantitative (offset of the pinch voltage of 0.2V and wrong size of the conductance plateaus). The results are fully converged after a single iteration of the ILDOS. These calculations, which map the input experimental parameters to the experimental observables, are directly comparable to experiments.

We present next some more informations that can be extracted from the self-consistent result through Kwant. While not being new per. se. , they serve to illustrate the analytical power given by a self-consistent solver coupled to a transport analysis tool such as kwant. In Fig. 3.4, the conductance at the Thomas-Fermi approximation level (blue dotted) and fully converged (red dotted) is compared to the density (top) and potential (bottom) at the center of the QPC. It is clearly visible

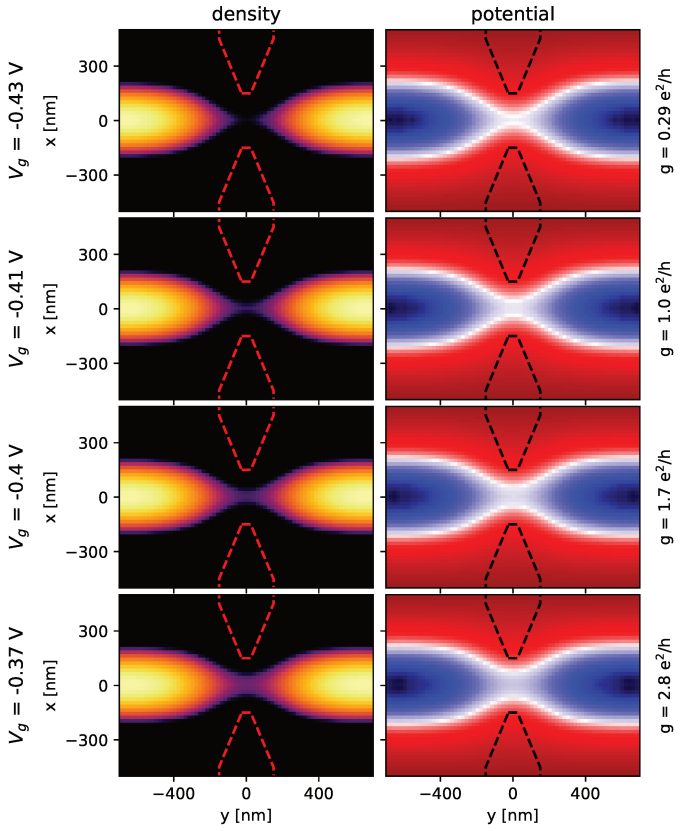

Figure 3.1: 2D maps of the density (left) and electric potential (right) for four different gate voltages $V_g = -0.43, -0.41, -0.4$ and -0.37V (top to bottom) for a QPC. Left: density of the 2DEG. (black corresponds to zero density). Right: electric potential (blue corresponds to negative potential where the 2DEG lies, white is zero and red corresponds to positive potential where the 2DEG is depleted). An additional side gate $V_s = -0.8$ depletes the gas far away from the QPC. The dashed lines indicate the gates of the QPC.

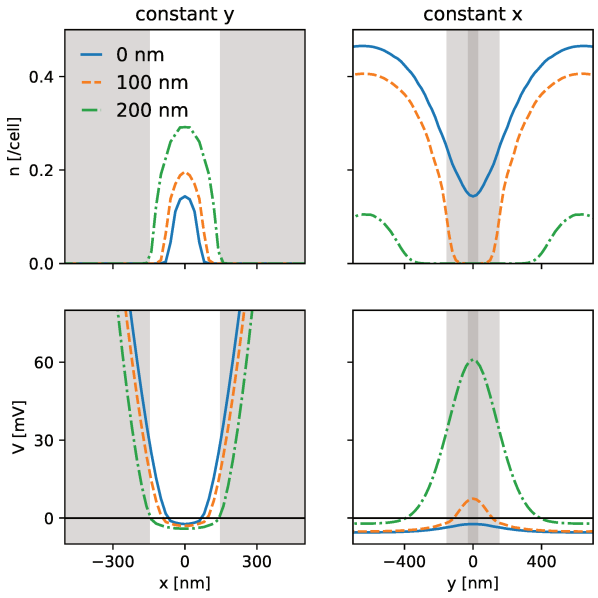

Figure 3.2: Cut of Fig.3.1 at constant x (left) and y (right) for the density (upper panels) and potential (lower panels). The cut correspond to $x, y = 0$ (blue), 100 (dashed orange) and 200 nm (dot dashed green). The gray area corresponds to the border of the metallic gates of the QPC. (bottom) Right: cut along y (parallel to the propagation) at different constant x of the density (top) and potential (bottom). The gray areas represent the QPC gates. The QPC gate voltage is set at $V_g = -0.37$ V

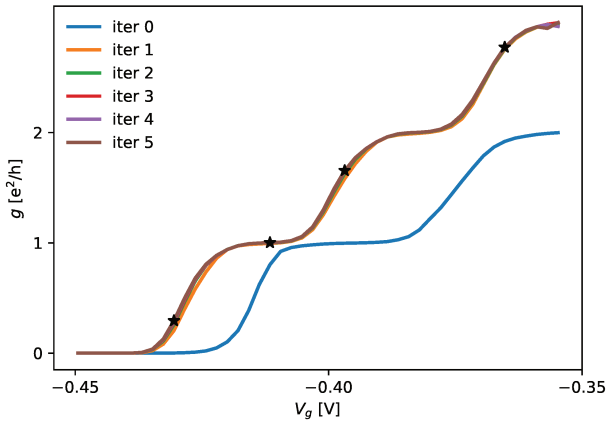

Figure 3.3: Conductance of a QPC in unit of e^2/h as a function of the gate voltage V_g for different quantum iterations (QAA). The zeroth iteration (blue line) corresponding to Thomas Fermi calculations. The black star indicate the chosen voltages and conductances for Fig 3.1.

that the density is not drastically modified by the step III iterations, whereas the potential is, which has an strong impact on the conductance.

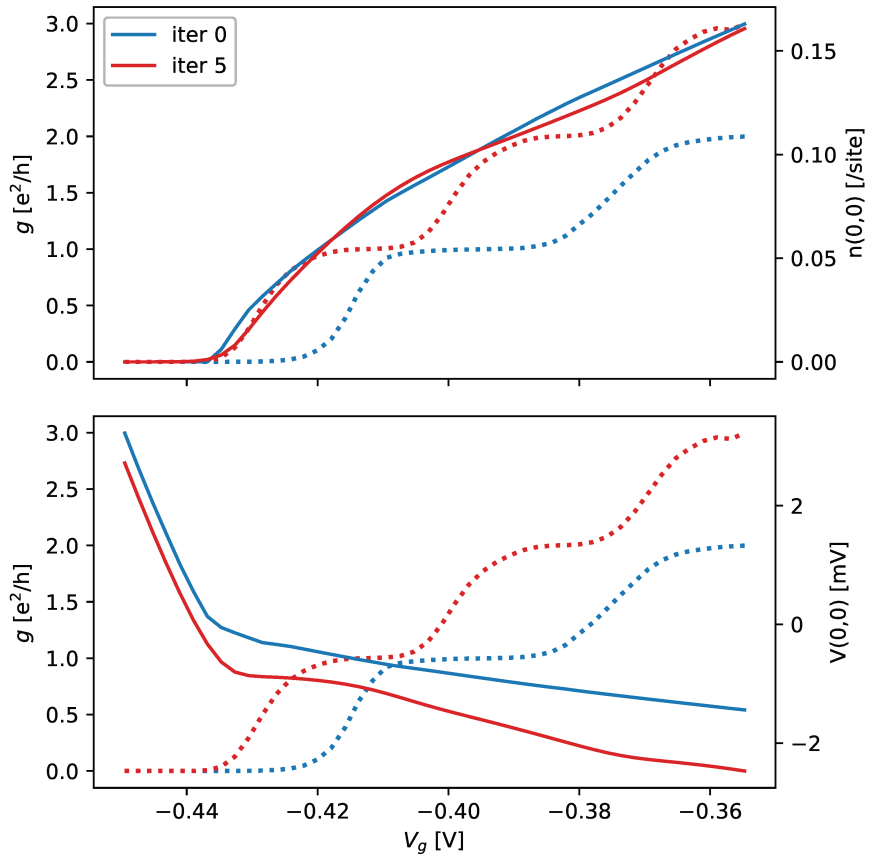

Figure 3.4: Conductance and density(potential) at the center as function of the QPC gate voltage V_g. Top: the solid lines are conductance (same as 3.3) and the dashed lines are the charge densities in the center respectively at iteration 0 (blue) and iteration 5 (red). Bottom: the solid lines are the conductances and the dashed line are the potentials in the center. The same color code is used.

Informations about the structure of the conductance plateau can also be obtained. Indeed it is possible to calculate the share of each propagative mode in the conductance. In Fig. 3.5, one sees that the modes open one by one, and once opened, are perfecty transmitted.

This can also be seen in the spatial map of the transmitted current (Fig. 3.6), where we plotted the first (ψ_0) second (ψ_1) and third (ψ_2) modes spatial density for different gate voltage, corresponding to conductances of $g = 0.29, 1., 1.7$ and 2.8 e^2/h. The different gate voltages are the rows, the different modes are the columns. The sum over all the modes $\sum_i \psi_i$ is shown in the last column. One sees that for $g < 1e^2/h$, only the fist mode is transmitting, then the second modes opens, and finally the third one.

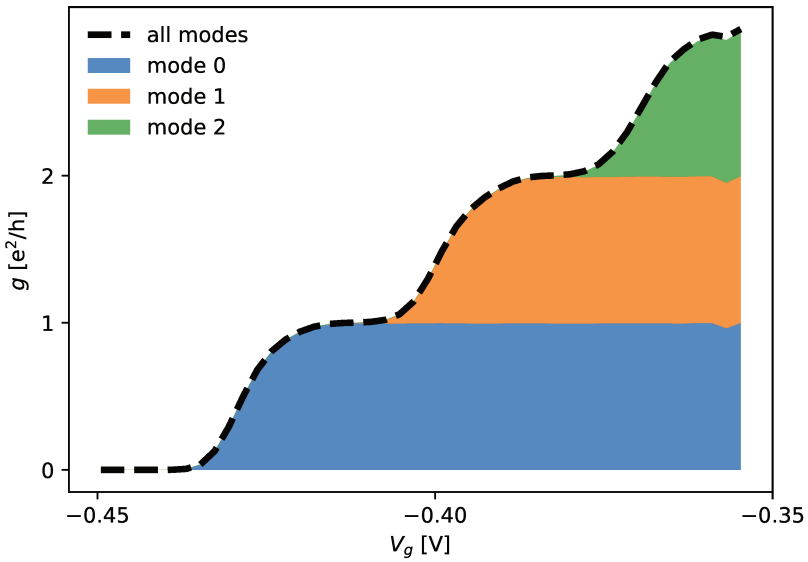

Figure 3.5: Decomposition of the total conductance (dashed black line) into the conductances due to the three first modes of the leads respectively in blue, orange and green.

Another very important tool is the possibility to analyze the band structure (Fig. 3.7), both in the leads and in the center of the QPC considered as a lead. We see that while 16 modes are opened in the leads, only 1, 2 or 3 are opened in the center, which correspond to the quantized conductance observed.

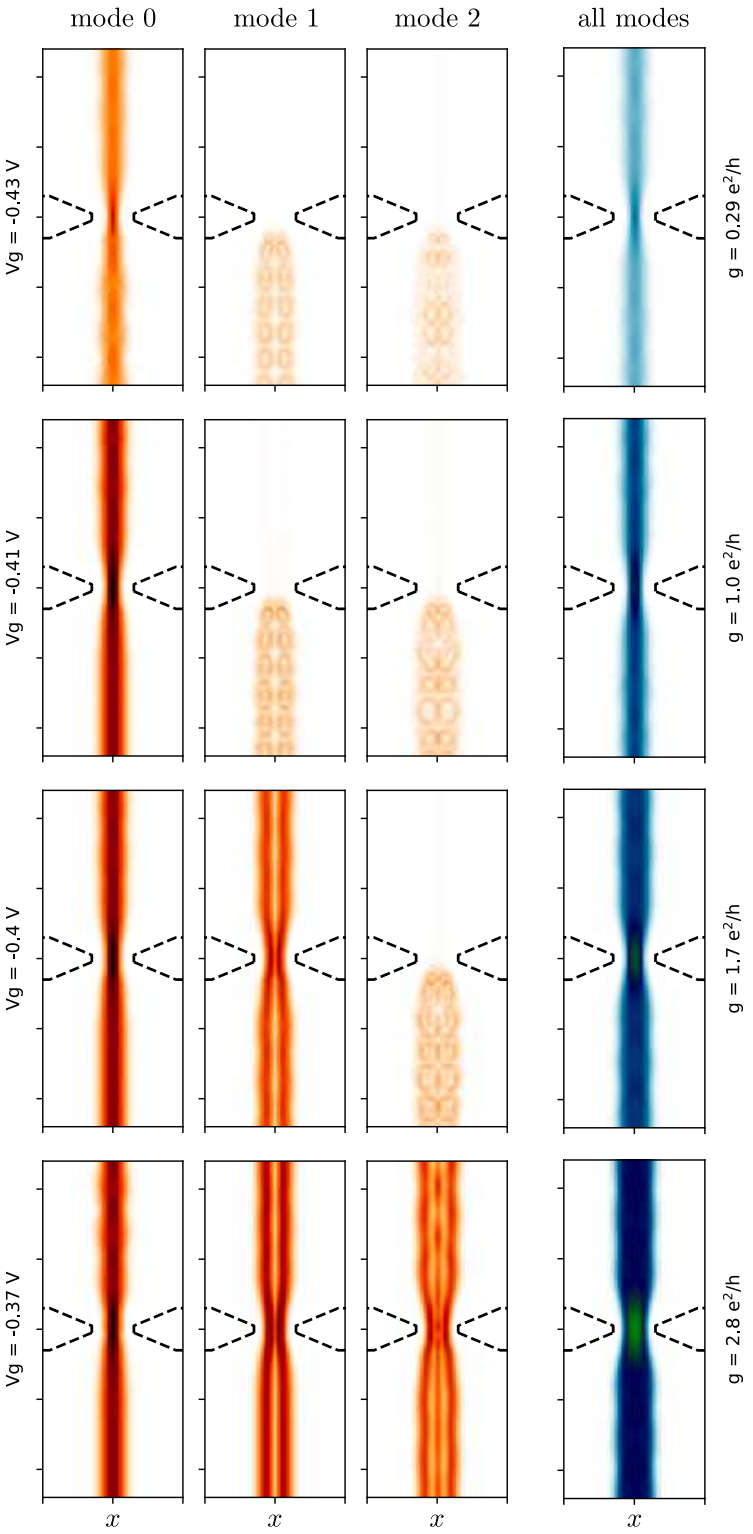

Figure 3.6: Map of the current transmitted from the bottom to the top at the Fermi energy in the 2DEG for different gate potential V_g. The 3 first columns are the maps of the current from the 3 first channels of the lead. The last column is the total current due to all the channels.

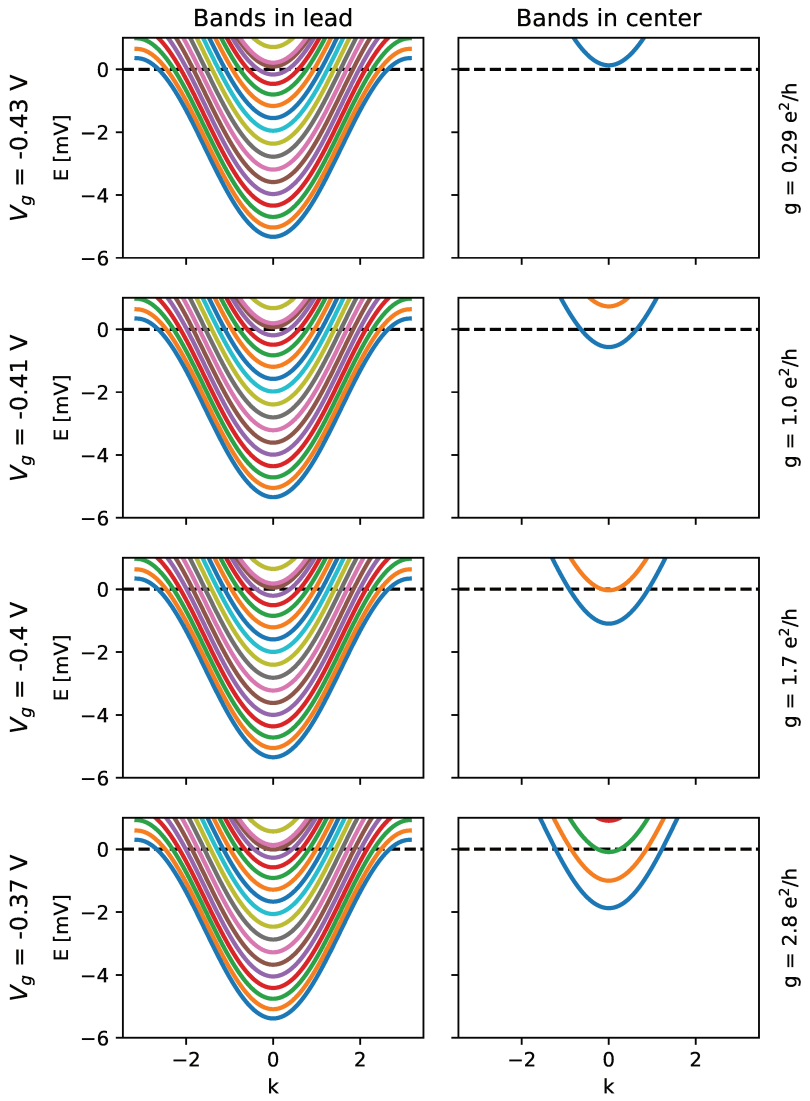

Figure 3.7: Band structures in the lead (left) and in the center of the QPC (right) for different gate voltage V_g.

4

Application to the quantum Hall effect

Finally to conclude this first part, we apply our algorithm to situations where the density of state varies abruptly which renders the quantum-electrostatic problem highly non-linear. A rather extreme situation is the quantum Hall effect where the ILDOS has the staircase shape shown in Fig. 2.2. Contrarily to the application to the QPC, we discuss here the new physical insights that have been given by the self-consistent solutions. We consider the geometry of Fig. 4.1b in presence of a perpendicular magnetic field. The physics contained in this chapter is taken from reference [3]. We start by introducing the theoretical aspect of the quantum hall effect, that is the compressible and incompressible stripes, and then extend it using our self-consistent results. Readers not familiar with the integer quantum Hall effect and/or the picture of compressible and incompressible stripes can get an introduction to the subject in D.

4.1 Introduction

Electrostatic energy is very often the largest energy scale in a physical situation. Yet, the electrostatic landscape is equally often taken for granted as an external potential, which may result in a wrong physical picture. A well known example is the quantum Hall effect [33] (QHE) that has been largely discussed using the concept of edge states in a non-interacting Landauer-Buttiker (LB) picture [34, 35]. Despite being very successful for the understanding of e.g. the quantification of the Hall resistance and the vanishing longitudinal resistance, the LB picture also fails spectacularly to describe basic physics such as the density profile of the electron gas. In a series of articles [36–38] that culminated with the work of Chklovskii, Shklovskii and Glazman (CSG) [8, 39, 40], it was recognized that the LB picture should be revisited. It was shown that the interplay between quantum mechanics

and electrostatics leads to the emergence of compressible and incompressible stripes, a concept related, yet somehow different, to the original edge states. An important effort has been devoted to the experimental observation of these stripes [41–51]. CSG work, as well as a large fraction of the subsequent literature [52–61] was based on the Thomas-Fermi approximation which is suitable at high magnetic field but inadequate at low field where the LB approach is expected to work well. More recent works improved on Thomas-Fermi by incorporating a Gaussian broadening of the Landau levels [21, 62, 63]. Solving the full self-consistent electrostatic-quantum problem, beyond the above approximations, is a difficult task however, as the presence of the Landau levels (and the associated Dirac comb for the density of states) makes the set of equations highly non-linear. In this letter, we use a newly developed numerical technique capable of handling this problem [3] and explore how the LB channels present at low field evolve into CSG compressible stripes at high magnetic field. Using the solution of the full self-consistent problem, we find that in a large region of the parameter space the system is in an "hybrid" phase that borrows features from both the LB and CSG pictures.

4.2 The LB picture of the QHE regime (and its failure)

We consider the infinite wire geometry of Fig. 4.1a: a two dimensional electron gas at the interface between GaAs and GaAlAs is placed under a perpendicular magnetic field B and confined to quasi-1D through two gates situated a few tens of nm above the gas. In the effective mass approximation, the electronic wave function $\psi(x, y)$ is described by a simple Schrödinger equation,

$$\frac{1}{2m^\star}\left(i\hbar\vec{\nabla} - e\vec{A}\right)^2 \psi(x,y) - eU(x)\psi(x,y) = E\psi(x,y) \tag{4.1}$$

where the vector potential takes the form $\vec{A} = Bx\vec{y}$ (Landau gauge) and $U(x)$ is the electrostatic potential (m^*: effective mass, e: electron charge). In the LB picture, the function $U(x)$ is an external input of the problem. The general solution of Eq.(4.1) takes the form of plane waves $\psi_n(x, y) = \psi_n(x)e^{iky}$ along the y-direction with momentum k. In the absence of $U(x)$, these states are simply the Landau levels [64]: equally spaced highly degenerate dispersiveless levels $E_n(k) = \hbar\omega_c(n+1/2)$ with states $\psi_n(x)$ that are exponentially localized along the x-direction around $x_k = kl_B^2$ ($l_B = \sqrt{\hbar/(eB)}$: magnetic length, $\omega_c = eB/m^\star$: cyclotron frequency, n integer). Applying an external confining potential $U(x)$ around the edges of the sample (such as the one shown in the inset of Fig. 4.1c) provides the usual Landauer-Buttiker (LB) picture for the edge states of the QHE. For a slowly varying $U(x)$ (Thomas-Fermi approximation), the spectrum becomes dispersive and follows the potential

$$E_n(k) \approx \hbar\omega_c(n + 1/2) - eU(x_k) \tag{4.2}$$

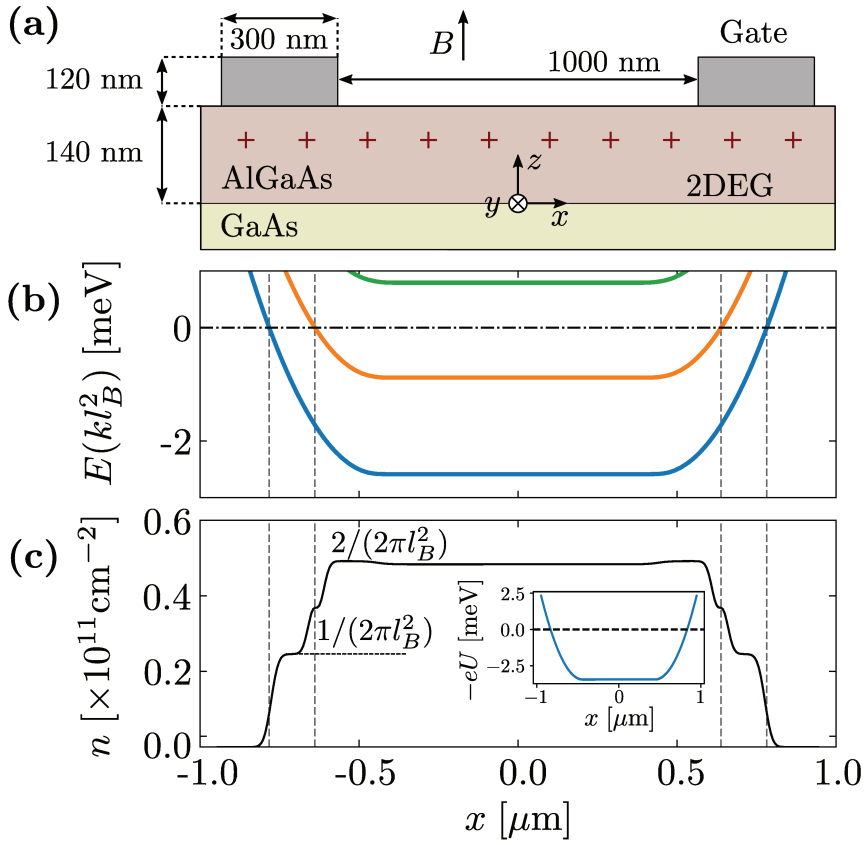

Figure 4.1: Non-interacting picture of QHE. a) side view of the system (infinite along the y direction). b) Dispersion relation $E_n(x = kl_B^2)$ for the three lowest Landau levels. c) density profile $n(x)$ (thin line) with Fermi level $E_F = 0$ and $B = 1T$. The results of b) and c) have been calculated using a direct numerical solution of Eq.(4.1) with the external potential $U(x)$ shown in the inset of c).

$E_n(k)$ crosses the Fermi energy ($E_F = 0$) and provides conducting LB channels. The localized channels are the edge states of the system. The corresponding band structure is shown in Fig. 4.1b. These edge states are localized around x_k and chiral (the velocity $v_k = (1/\hbar)dE/dk$ is positive for the edge states on the right of the sample and negative on the other edge). The associated velocity is directly linked to the confining potential $v_k \approx (l_B^2/\hbar)dU(x)/dx$.

The main problem with the LB picture can be seen in Fig. 4.1c) where the associated electronic density profile $n(x)$ is shown. In the bulk of the system there are exactly two filled Landau levels, hence the electronic density is given by their corresponding degeneracy $n(x) = 2/(2\pi l_B^2) = 2eB/h$. As one moves towards the edge of the sample, one reaches the point where the second Landau level is not filled any more and the density drops to $n(x) = 1/(2\pi l_B^2)$ and eventually to $n(x) = 0$. In this picture, the density is essentially set by the magnetic field B. However, the typical energy associated with the field $\hbar\omega_c$ is of the order of 10meV which is several order of magnitude smaller than the electrostatic energy that would be needed to

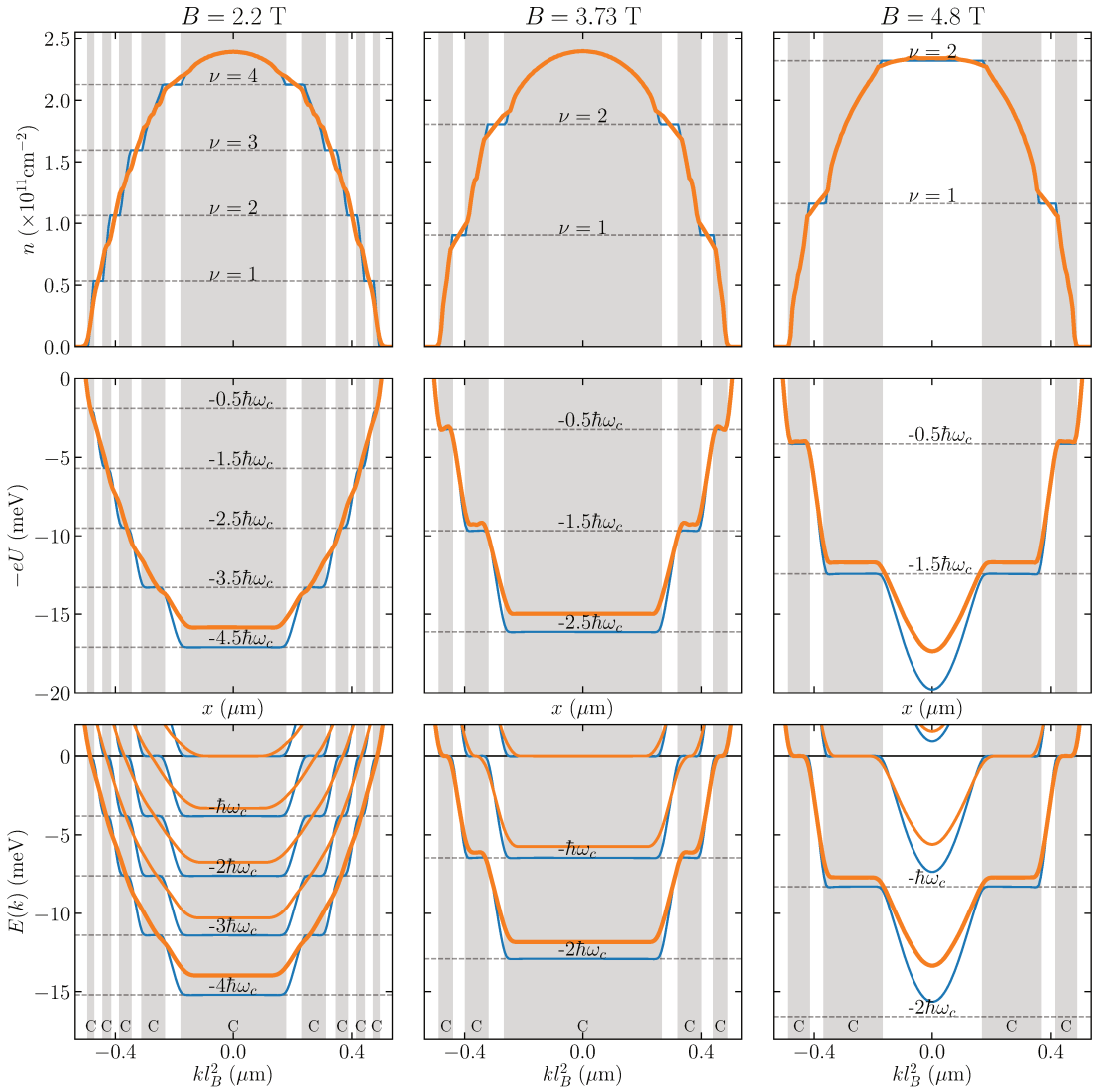

Figure 4.2: Electronic density $n(x)$ (top), potential $U(x)$ (middle) and band structure $E_n(k)$ (bottom) for three different values of the magnetic field at confinement $V_g = -0.75$V. Blue line: self-consistent Thomas-Fermi calculation; orange lines: full self consistent solution of the quantum-Poisson problem Eqs.(4.1), (4.3), (4.4) and (4.5). The gray "C" regions indicate the compressible stripes while the white regions are incompressible.

deform whatever electronic density $n(X, B = 0)$ was there at $B = 0$ into the one of Fig. 4.1c). One concludes that the potential $U(x)$ should not be considered as an external input but rather as the solution of the Poisson equation,

$$\Delta U(\vec{r}) = -\frac{e}{\epsilon} n^{\mathrm{d}}(\vec{r}) \tag{4.3}$$

$$\frac{dU}{dz}(z=0^+) - \frac{dU}{dz}(z=0^-) = -\frac{e}{\epsilon}n(x) \tag{4.4}$$

where $n^{\mathrm{d}}(\vec{r})$ is the (3D) dopant density and $n(x)$ the (2D) density of the electronic gas. In our wire geometry, the electronic density is given by

$$n(x) = \sum_n \int \frac{dk}{2\pi} |\psi_{nk}(x)|^2 f(E) \tag{4.5}$$

which closes our system of equation ($f(E) = 1/(e^{E/k_BT}+1)$ is the Fermi function). In the QHE regime, Eqs.(4.1), (4.3), (4.4) and (4.5) form a highly non-linear set of equations.

4.3 The CSG picture of compressible and incompressible stripes

The strength of CSG argument is that the entire physical picture can be constructed from simple considerations, essentially from the dispersion relation Eq.(4.2) that relates the energy of the Landau level $E_n(k)$ to its spatial position x_k. Let us suppose that we know the density profile $n(x, B = 0)$ in the absence of magnetic field. We further assume that this profile (which results from the interplay between the electrostatic and kinetic energy) is only weakly affected by the presence of the magnetic field (as argued above the cyclotron energy $\hbar\omega_c$ is small compared to the electrostatic energy needed to strongly modify the density profile). For a generic value of the field, it follows that the filling fraction $\nu \equiv n_0 2\pi l_B^2$ of the Landau levels in the bulk of the sample ($n_0 = n(x = 0, B = 0)$ has generically a non-integer value e.g. $\nu = 2.4$. From that statement, it follows that a Landau level (in this example the third one) *lies exactly at* the Fermi energy since it is only partially occupied. This is a very different situation from the non-interacting picture discussed above. As one gets away from the center of the sample towards the edge, the filling factor $\nu(x) \equiv n(x, B = 0)2\pi l_B^2$ decreases until the third Landau level is totally depleted and one starts to deplete the second Landau level. Depleting the second Landau level implies that it sits at the Fermi energy, hence a sharp rise of the electrostatic energy (of amplitude $\hbar\omega_c$). In the small region where this sharp rise occurs, the density is constant (no available level at the Fermi energy). This region is an incompressible stripe. Continuing towards the edge, we hence obtain a set of compressible stripes separated by incompressible stripes. The blue lines of Fig. 4.2 shows the resulting dispersion relation (lower panels) and density profile (upper panels) for three different value of the magnetic field. The blue lines of Fig. 4.2 ressemble very strongly the cartoon shown in Fig.1 of the CSG paper. However, they correspond to a full self-consistent calculation in the Thomas-Fermi approximation.

4.4 New results

Hybrid phase at intermediate fields

We now turn to the full self-consistent solution of the problem Eqs.(4.1), (4.3), (4.4) and (4.5) without using the Thomas-Fermi approximation. Note that in what follows, the Landau levels are supposed to be fully spin polarized, we do not discuss the magnetic instabilities. The results are shown with orange lines in Fig. 4.2. At high field (middle and right panels), the full solution bears strong similarities with the Thomas-Fermi result and one gets alternated compressible and incompressible stripes with the middle of the sample being compressible (middle panels) or incompressible (right panel, corresponds to a quantized plateau of conductance) [40]. One qualitative differences is the absence of well defined plateaus of the density in the incompressible region. This is due to the fact that the Landau levels spread over a width l_B which is not infinitely small compared to the width of the incompressible stripes (e.g. $l_B \approx 13$ nm at $B = 3.73$ T). At very low magnetic fields (not shown), one fully recover the LB picture with well defined propagating channels that cross the Fermi level. We find that the transition between the LB picture and the CSG one at high field happens in two stages: first, the formation of Landau levels that get pinned at the Fermi level; secondly the evolution of the edge states into compressible stripes. In the corresponding intermediate field range, the system is in an intermediate "hybrid" phase with well defined edge states (similar to those shown in Fig. 4.1) yet with a central compressible stripe that remains pinned at the Fermi level. This situation is illustrated in the left panel of Fig. 4.2 ($B = 2.2$ T, corresponding to $\nu \approx 4.5$).

Magneto-conductance of ballistic wires

To gain further insight, we now turn to a discussion of the current that flows upon applying a small bias voltage across the wire. Note that the question of where does the current flow is ill defined in the Thomas-Fermi approximation, at least at very small temperature. Indeed the current must flow in the compressible regions since transport requires available states at the Fermi level. Yet in the compressible regions, the velocity $v_k = (1/\hbar)dE/dk$ vanishes, hence one would expect the current to do the same. This small paradox (which points to the current being concentrated to the edge of the compressible stripes) is resolved by using the full self-consistent solution.

In a perfectly ballistic system where all conducting channels are perfectly transmitted, the conductance g is given by a simple form of the Landauer formula,

$$g = e^2 \sum_n \int \frac{\mathrm{dk}}{2\pi}\, \theta(v_{nk}) v_{nk} \left(-\frac{\partial f}{\partial E}[E_n(k)] \right) \tag{4.6}$$

where the Heaviside function $\theta(x)$ selects the channels with positive velocities. At

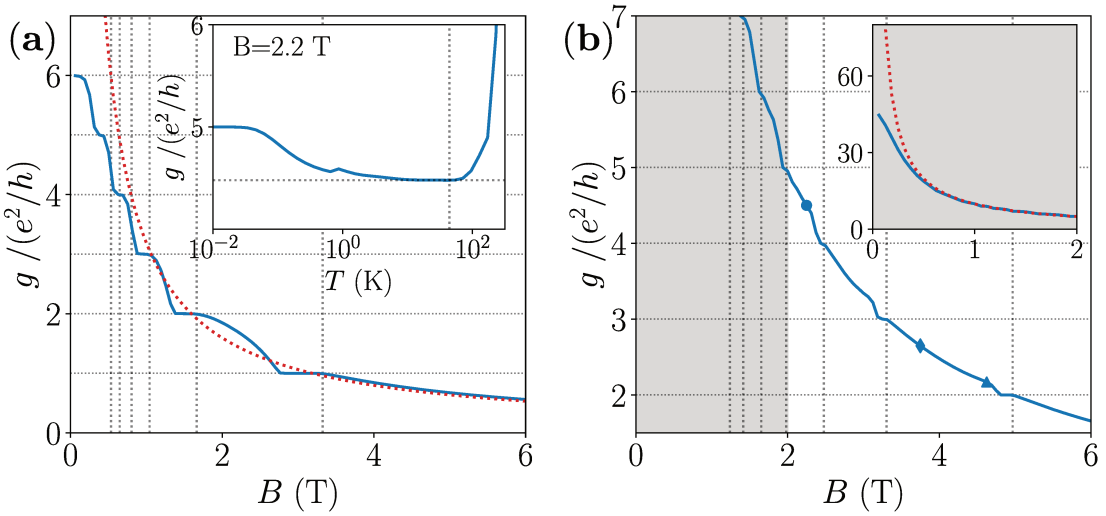

Figure 4.3: **(a)** Conductance $g(B)$as a function of the magnetic field for a confinement $V_g = -1.6$V at $T = 1$K (thin blue line). The dotted line indicates the $g = n_0 e/B$ law, horizontal lines indicate quantized values of the conductance while the vertical lines the expected position of the Hall plateaus from the bulk density n_0: $B_\nu = n_0 h/(e\nu)$. Inset: $g(T)$ as a function of the temperature (log scale) for a confinement $V_g = -0.75$ V. The vertical line indicates $k_B T = \hbar\omega_c$. **(b)** Same as (a) for $V_g = -0.75$ V. The round, diamond and triangle symbols mark respectively the conductance at $B = 2.2, 3.73$ and 4.8T of Fig. 4.2. Inset: zoom of the main panel at small field.

zero temperature, this formula provides the well-known quantization of conductance: using $v_k = (1/\hbar)dE/dk$ and the fact that $df/dE \to -\delta(E)$ one finds that g simply counts the number of bands that cross the Fermi level (in unit of e^2/h). The CSG situation where there is a degenerate band exactly at the Fermi level is a new situation as it can lead to *non-quantized* conductance even in a ballistic conductor. Indeed, assuming that $E_n(k)$ is a (very slowly) increasing function of k from $k = 0$ to $k = \infty$, one gets $g = (e^2/h)\sum_n f[E(k=0)] - f[E(k=\infty)]$ which translates into $g = (e^2/h)\nu$. Since the central stripe is in general not fully filled, this results in a non quantized conductance that scales as $\sim 1/B$ except for the plateaus occurring when the central region is incompressible. This situation corresponds to a regime where the temperature is very small compared to the cyclotron frequency, yet large compared to the small variations of the electric potential in the central Landau level. It is in sharp contrast with the zero temperature limit where quantization is always expected.

This is illustrated in the inset of Fig. 4.3a where we plot the conductance versus temperature in the hybrid phase: We identify three regimes: a regime of large temperature (with respect to $\hbar\omega_c$) and accordingly large conductance; a regime of low temperature where one recovers the LB quantization; and an intermediate regime without quantization $g = (e^2/h)\nu(B)$. The crossover between the later two is

strongly system dependent: it depends on the small curvature of the electric field in the bulk of the sample, hence on the strength of the gate voltage and magnetic field. It is interesting to note that even for moderate confinement (here $V_g = -0.75$V and the gas still occupies most of the space in between the two electrodes, this crossover takes place at $T \sim 100mK$, i.e. much higher than typical dilution fridge temperatures. The transition from the LB to the CSG regime can also be seen as a function of magnetic field, see Fig. 4.3a (strong confinement) and Fig. 4.3b (weak confinement). At low field, one observes the LB plateaus of conductance which are replaced at higher field by a general $1/B$ law intertwined with the Hall plateaus. The crossover between the two regimes can be identified from the deviation of the conductance with respect to the $g = (e^2/h)\nu(B) = n_0 e/B$ law (dotted line). Note that the $g = n_0 e/B$ law can be extracted directly from the experiment since the bulk density n_0 can be extracted from the B-position $B_n = n_0 h/(en)$ $(n = 1, 2 \dots)$ of a Hall plateau at high field.

Discussion

The full self-consistent approach of the quantum-electrostatic problem allows one to treat on the same footing the low field LB regime and the large field CSG regime. Likewise, it allows to understand how one crossovers from well defined conducting channels at zero temperature to the CSG quantum Hall regime. Our most surprising result is that the quantum Hall effect appears in two stages which leads to the hybrid phase described above. A rough estimate of the parametric regime where this hybrid phase is expected goes as follows. The typical width w of a compressible stripe is set by the density profile $n(x, B = 0)$. If x_0 defines the position of an integer filling $\nu = n(x_0, B = 0)2\pi l_B^2$, then $n(x_0 + w, B = 0)2\pi l_B^2 = \nu - 1$. Noting d the typical distance with which $n(x_0, B = 0)$ falls from its bulk value to zero, we get $w \sim (d/\nu)$. d depends strongly on the electrostatics of the problem; it is of the order of the distance between the gate and the gas, $d \sim 140nm$ in our example. The crossover from the compressible stripe behavior to the LB like edge state is expected when quantum fluctuations are large enough, i.e. $w \sim l_B$. This translates into $\nu_0 \sim (n_0 d^2)^{1/3}$. Hence, for filling fraction larger than $\nu_0 \sim (n_0 d^2)^{1/3}$ one expects LB like edge states while for higher magnetic field, one recovers the CSG stripes. In our (rather typical) example, the hybrid scenario corresponds to most Hall plateaus $\nu > (n_0 d^2)^{1/3} \approx 3$.

As the LB edge states and CSG stripes are both associated with one quantum of conductance, it remains to discuss the difference between the two situations in actual observables. We expect an important difference in the propagation of voltage pulses [65] (edge magneto-plasmons). Indeed, the plasmon velocity is proportional to the Fermi velocity (up to a renormalization factor due to Coulomb interaction [6,66]) of the corresponding mode. For a LB edge state, this velocity $v_k = (1/\hbar)dE/dk$ is a well defined quantity that depends on the confining potential i.e. $v_k \sim \hbar/(dm^*)$. We find typical values $v_k \sim 10^5$ m.s^{-1} consistent with the values quoted in the literature. The situation is drastically different for a CSG compressible stripe where the velocity

vanishes in the middle of the stripe and sharply rises on its boundaries. If follows that the average velocity in the stripe drops down upon entering the CSG regime. Perhaps more importantly, the velocity now strongly depends on k which results in an important spreading of the excitation between the slow part in the middle of the stripe and the faster part toward its edges. Hence, we expect that at high field, voltage pulses will get highly distorted in sharp contrast with the behavior in the hybrid phase at lower field. We anticipate that the hybrid phase is more favorable for the propagation of pulses than the CSG phase.

4.5 Complementary informations

The positions x_ν of the center of the incompressible stripes can be estimated from the electronic density calculated at zero field $n(x, B = 0)$ since, with very good approximation, $n(x_\nu, B = 0) = \nu eB/h$ ($\nu = 1, 2, \dots$). *Complementary details about this calculations can be found in appendix D.* The width δx_ν of these plateaus can also be estimated using a simple energetic argument. The creation of the incompressible stripe involves the creation of the small electric dipole of charge δq_ν with respect to the $B = 0$ density. On one hand, we have $\delta q_\nu \approx e\partial_x n(x_\nu, B = 0)\delta x_\nu$. On the other hand, electrostatics imposes $\delta q_\nu \approx c(\epsilon/\delta x_\nu)(\hbar\omega_c/e)$. Here $c(\epsilon/d)$ is the effective capacitance of the problem and $(\hbar\omega_c/e)$ is the kinetic energy gained by creating the stripe which compensates the corresponding electric energy ($\omega_c = eB/m^\star$ is the cyclotron frequency). We arrive at [8],

$$\delta x_\nu \approx \sqrt{\frac{c\epsilon\hbar B}{em^*\partial_x n(x_\nu, B = 0)}} \tag{4.7}$$

with the constant given by $c \approx 5.1$ for our particular geometry. To verify the above expression, Fig. 4.4 plots the gradient of the density $\partial_x n$ (top panels) and of the electric potential $\partial_x U$ (bottom panels) as a function of position x and magnetic field B. The gradients vanish for the incompressible and compressible stripes respectively. Left and right panels correspond respectively to Thomas-Fermi and FSC which are difficult to distinguish at this scale. The different types of stripes are easy to identify. The dashed line corresponds to the width predicted with Eq.(D.9) which match the numerics quantitatively.

We now proceed to the calculation of the conductance of a ballistic conductor. Assuming all channels are perfectly transmitted (no reflection), the Landauer formula takes a particularly simple form

$$g = -2e^2 \sum_\alpha \int \frac{dk}{2\pi}\, \theta(v_{\alpha k}) v_{\alpha k} \frac{\partial f}{\partial E}[E_\alpha(k)] \tag{4.8}$$

where $v_{\alpha k} = \partial_k E_\alpha(k)/\hbar$ is the velocity of the mode α at the Fermi energy and the Heavyside function selects channels with positive velocity. The obtained conductance as a function of the gate voltage for two temperatures and magnetic fields are

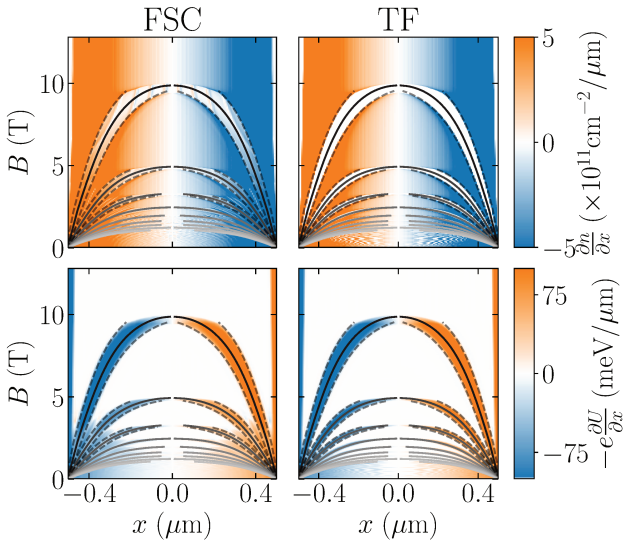

Figure 4.4: Gradient of the density (top) and potential (bottom) as a function of the magnetic field B at $V_g = -0.75$V for the geometry of Fig.4.1b. Left panel: FSC, right panels: Thomas-Fermi. The black lines correspond to the theoretical estimate for x_ν while the dashed lines correspond to $x_\nu \pm \delta x_\nu/2$ for the first three Landau levels $\nu = 1, 2, 3$.

shown in Fig. 4.5. These calculations show the crossover between channel quantization at low field and the quantum Hall effect at high field. It is interesting to note that the presence of a degenerate band at the Fermi level in the quantum Hall regime leads to a non quantized conductance even though the system is perfectly ballistic. The dashed orange line shows the corresponding estimate $g = n(x = 0, B = 0)e/B$ which fits fairly well the conductance outside of the plateaus.

We proceed with the calculation of the local density of current $J(x)$ which is given by,

$$J(i) = -2e^2 \sum_\alpha \int \frac{\mathrm{dk}}{2\pi} |\psi_{\alpha k}(i)|^2 \theta(v_{\alpha k}) v_{\alpha k} \frac{\partial f}{\partial E}[E_\alpha(k)] \tag{4.9}$$

The dependance of $J(x)$ as a function of position and magnetic field is shown in the colormap in Fig. 4.6. Note that we only discuss the out-of-equilibrium current. In the quantum Hall regime there is also an equilibrium current flowing in the incompressible stripes. Here, it has been subtracted. Fig. 4.6 provides the answer to a small paradox: in incompressible stripes there is no available states at the Fermi level, and thus no out-of-equilibrium current can flow in these zones. Therefore, the current can only flow in the compressible regions. However, in the latter the dispersion relation is flat, hence the states have vanishing velocity, and thus vanishing currents. Therefore it would naively seem that no out-of-equilibrium current can flow in the system. This paradox is only present in the Thomas-Fermi picture. Indeed, the FSC calculations clarify the question of where the current flows. Un-

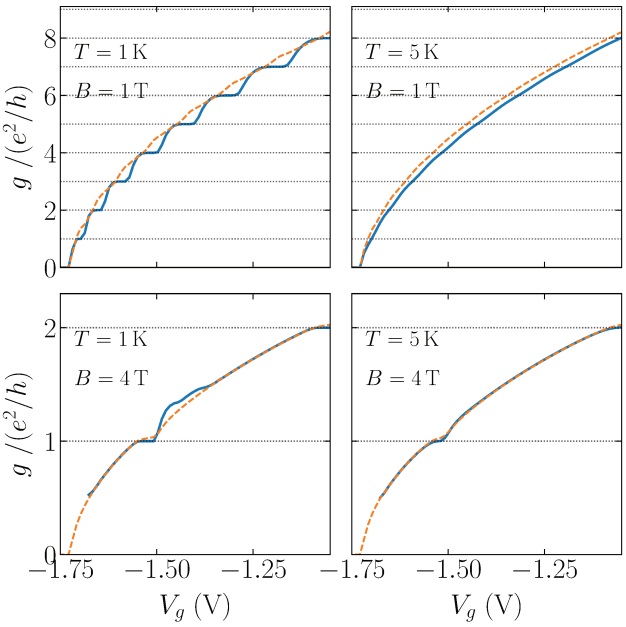

Figure 4.5: Conductance g in units of e^2/h as a function of the gate voltage Vg for two different magnetic field ($B = 1$ T and 4 T (up and bottom panels) and 2 different temperatures ($T = 1$ K and 5 K (left and right panels). Solid blue line: FSC calculation, Dashed orange line: $g = n(x = 0, B = 0)e/B$. Horizontal thin dotted lines correspond to quantized values of the conductance.

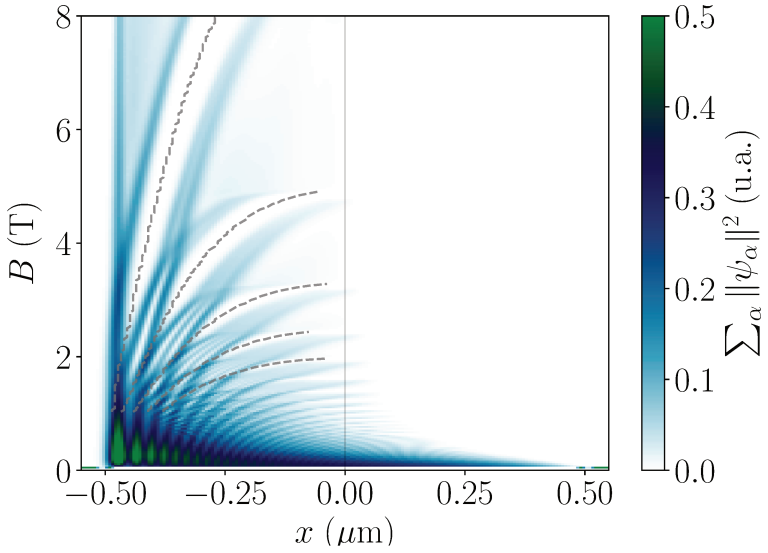

Figure 4.6: Map of the current density $J(x)$ as a function of the position x and the magnetic field B. Dotted line indicate the centers of the incompressible stripes.

surprisingly, we find that the current density lies mostly at the boundary between compressible and incompressible stripes.

One can confront the spatial profile of the current to the gradient of the density and potential to identify the compressible and incompressible stripes. This is shown is Fig. 4.7.

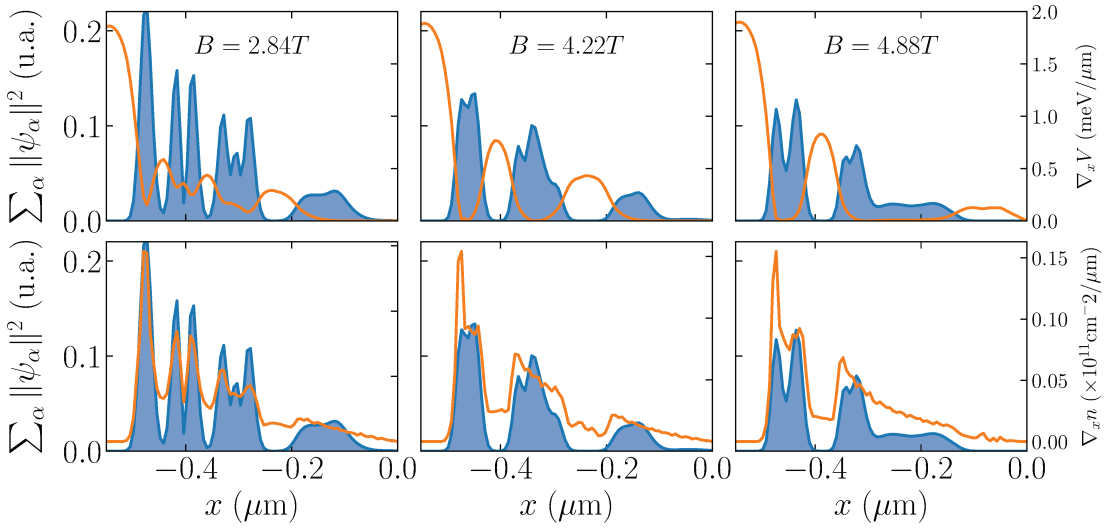

Figure 4.7: Current profile (full blue) in x for different magentic fields and gradient of the corresponding self-consistent potential (top rown orangle line) and the density (bottom row, orange line). The currents flows in the whole compressible strip (potential is constant and density varies).

Part II

The flying qubit project

SUMMARY OF PART II

The second part of this thesis is dedicated to our calculation of the velocity of surface plasmons that can be used as flying (propagating) qubits. One usually thinks of quantum bits (qubits) in the form of static qubits, i.e two (or more) levels physical systems which states allows to encode information. But it is also possible to conceive flying qubits, as two conduction lines representing the two pure states of the qubits. Operations can be realized on such qubits by allowing the two lines to interfere with each other. It is therefore of crucial importance to be able to predict and control the different experimental parameter, starting with characterizing the interferometer and establishing the velocity of these qubits.

We will show that a spectroscopy of such an interferometer can be performed and simulated using only static quantities. These results where obtained by B. Rossignol, using the self-consistent algorithm used in part I [5]. The flying qubits propagate on the conduction lines in the form of charged collective excitations (surface plasmons). Due to electrostatic interactions, these pulses propagate at velocities typically five times greater than the Fermi velocities of the individual propagating modes of the conduction line. Reference [6] is a joined work between the group of C. Bauerle in institut Neel who measured these velocities experimentally and us who made the corresponding calculations. To reproduce these measurements in simulations we first established a multichannel Luttinger theory that allows one to directly connect the velocity to the microscopic details of the system, without the need of many-body theory. The effect of the electrostatic interactions is to mix the different individual modes propagating in the wire without interaction into collective channels. Thus, the plasmon velocity is found to be the eigenvalue of a linear problem. Using this theory we reproduced accurately the experimental results for velocities without any adjustable parameter.

5

The flying qubit project

One of the largest application domain of nano-electronic systems is quantum computing. Indeed, the theoretical proof has been made that some algorithm can be accelerated (the most known example being Shor's algorithm for factorization in prime numbers [67]) by doing computation on quantum superposition of states instead of classical two level systems. This has raised the interest of researcher in the nano-electronic field but also of private actors of the computing industry. Several implementations of these quantum bits (qubits) have been proposed and realized (supraconducting qubits [68–70], spin states [71–73], quantum dots [74, 75], etc.). These qubits as well as the computation operations between them are directly implemented into the hardware. However, here we will discuss another type of qubit: a flying qubit propagating along a circuit as opposed to the static qubits discussed above. In principle, one would be able to generate these qubit at will, stock them for some time and act upon them if necessary. This approach is totally different from the static one and we must stress here that it currently is at a much earlier development stage that the static one. After quickly introducing the flying qubits, we propose here two contributions to this emerging field through self-consistent calculations that will help to better understand and design these flying qubits.

First: one student in our group (B. Rossignol) developed a theoretical spectroscopy technique for Mach-Zender Interferometer (MZI). However, this theoretical work is based on an effective potential seen by the electrons. Using our self-consistent technique we could calculate this self-consistent potential, therefore enabling us to connect his predictions to the geometry and gate voltages used in experiments. This illustrate the strength of our approach: we can predict the electrostatic environment seen by the electrons in an experimental setup. Second: the group of C. Bauerle has been performing preliminary experiments in view of building a flying qubit. One of these experiments consists in measuring the velocity at which a voltage pulse propagates in a quasi one-dimensional geometry. We will develop a theory to predict these velocities (extension of the Luttinger liquid) and we will use our self-consistent

solver to connect this theory to the macroscopic experimental world. Again this will allow us to make predictions without any adjustable parameter.

5.1 What is a flying qubit and why is it interesting

In this short section, we aim to introduce the context in which flying qubits could be used. We first introduce the concept of the flying qubits, then show theoretical propositions to realize the necessary elements to build a flying qubit computer. This is mostly a summary of reference [32].

What is a flying qubit ?

Before focusing on the flying part, let us first remind that a qubit state is a superposition of two states, by convention $|0\rangle$ and $|1\rangle$. By analogy with the spin, one give it an arrow representation on the Bloch sphere. Performing operations on the qubit amounts to rotate the arrow on the Bloch sphere. A schematic example of an implementation of rotations of a flying qubit in the Bloch sphere are shown in Fig. 5.1. We suppose two parallel ballistic single electron channels (or rails) with the same energy. A short pulse containing one electron is injected in either of the rails. We call $|0\rangle$ the presence of an electron in the upper path and $|1\rangle$ the presence of an electron in the lower path, and any superposition of $|0\rangle$ and $|1\rangle$ gets a representation on the Bloch sphere. The system made of both rails in which an electron propagates is effectively a two level system, however it has the particularity that the information it carries propagates. This we call the flying qubit. As shown in Fig. 5.1 (a) and (b), one can manipulate this qubit. Rotation around the x-axis can be performed by contacting the two rails through, for example a tunnel barrier, and letting them interfere (see Fig. 5.1 (a) and references [76–79]). In analogy with its optical counterpart, this device is called a Mach-Zender interferometer (MZI). The rotation angle can be controlled by the interaction distance and the magnitude of the potential serving as a barrier. One can also realize a rotation along the z-axis using the Aharonov-Bohm effect [80, 81]. To do so, one connects the two branches to a ring traversed by a magnetic field (see Fig. 5.1 (b)). Upon traversing the ring, the two rails pick up a phase difference given by the Aharonov-Bohm flux traversing the ring.

How to theoretically build a flying qubit quantum computer

As we have seen, manipulating single flying qubits is at least possible. Two qubits operation can also be realized, for example through Coulomb coupling of two qubits (see Fig5.2). In this proposition, the phase of the second branch of a first qubit is

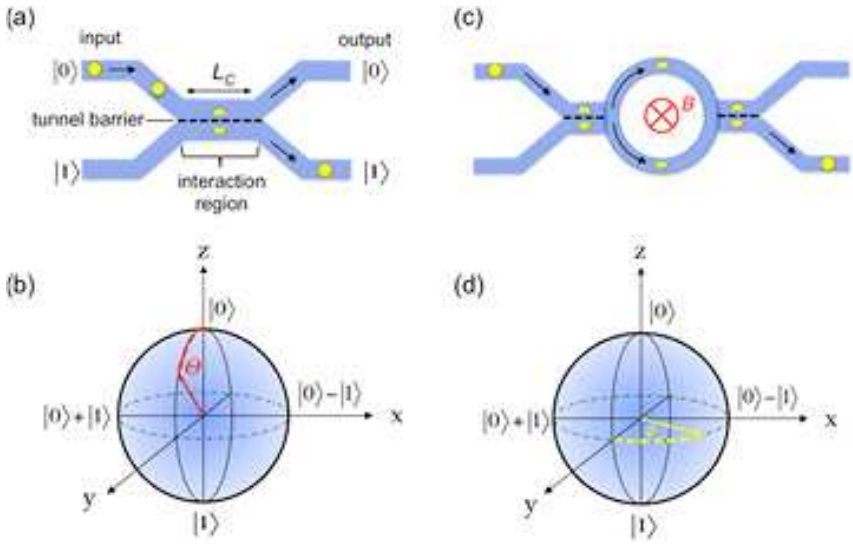

Figure 5.1: Exemple of implementation for single flying qubit operations. (a) a qubit in the $|0\rangle$ state is injected on the left. As it reaches the interaction region, the upper and lower rails can interact through a tunnel barrier before being separated again. (b) This interaction produces a rotation along the x-axis of the Bloch sphere. (c) The two rails are now brought to an Aharonov-Bohm ring applying a phase difference between the two rails. (d) This amounts to a rotation around the z-axis. (from reference [32])

influenced by the potential created by the presence of an electron in the first branch of a second qubit through Coulomb interaction (coulomb coupler CC in the figure). For additional control, 4 tunnel-coupling regions tunned to act as beam spliters (BS in the figure) are added. Other designs for two electrons operations can be found in references [82–84].

In principle, the single qubits rotations and the two qubit operation are the only logical block needed to build any type of logical operations. Then, one can imagine building a flying qubit quantum computer as shown in Fig5.3. On the left side, one injects qubits one by one. These qubits then enter a loop. During the travel on the loop, they can be directed to logic units, where for example their state can be modified or two qubits operation can be performed. It is also possible to use delay lines to change the order of the pulses. If needed, new qubits can be injected in the loop. After all the calculations that are needed have been done, a final measurement is performed giving the result of the calculation, or the qubits can be sent to another system.

Advantages of a flying qubit

One of the main advantages of the flying qubits compared to the static ones is that they can be generated at will. As a consequence, the hardware footprint of the flying qubit quantum computer does not depend on the number of qubits and thus

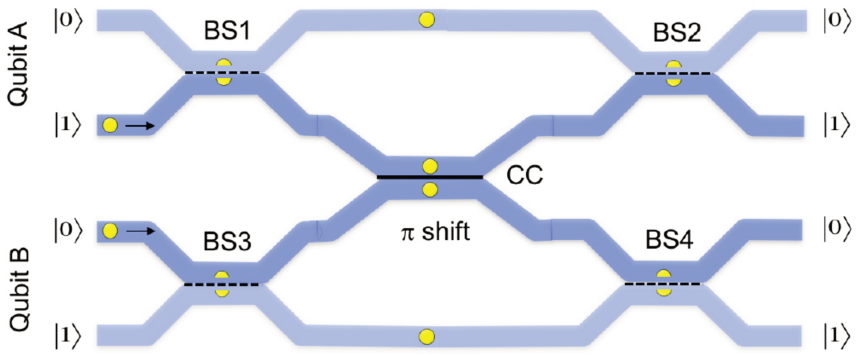

Figure 5.2: Example of implementation for a two flying qubit operation. In the presence of an electron in the rail $|0\rangle$ of qubit B, the phase of the rail $|1\rangle$ of qubit A is modified through coulomb interaction (coulomb coupler CC symbolized with a black line). For added control, 4 beam splitters (BS, black dashed lines) are also present. (from reference [32])

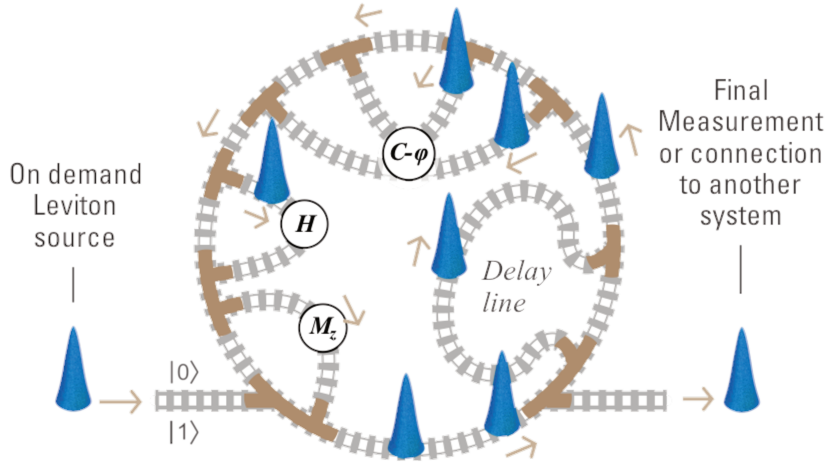

Figure 5.3: Schema of an hypothetical flying qubit quantum computer. Single electron pulses are injected from the left into a main loop. Along the loop, switches allow to direct the pulses into the different logical components to perform operations on qubits (rotation on the Bloch sphere: H or M_z) or between two qubits (C-φ). The order of the qubits can be changed using delay lines. After the calculations are done, the qubit is released to the right and can be measured of connected to another system. (Figure courtesy of X. Waintal)

on the quantity of information entering the loop and circulating inside. In principle any flying qubit can be made to interact with any qubit simply by using secondary loops (these means no need for Tgate factories as are needed in surface-code [85]). Since new qubits can be generated and old qubits can be thrown away, flying qubits can in principle be refreshed. Flying qubits can also be used as probes to check the hardware. Then, if a segment (for example a logic unit) is detected as faulty, the

user could be able to exclude this segment from the loop and redirect the qubits on alternative path. In general flying qubits rely on a totally different concept as the static qubits: the quantum information is separated from the hardware, which mostly consists of gates.

Coherence and the lost of it is at the center of trouble concerning quantum computing. Indeed, the loss of coherence is synonymous with loss of information which leads to the appearance of errors. Promising DC experiment in 2DEG have measured coherence length around 50 μm without magnetic field and up to 200 μm in the quantum hall regime [86]. The corresponding coherence length for levitons are still unknown. This length has to be compared to the length necessary to perform operation which is currently around 1 μm. On top of that, error correction is also also possible.

In conclusion, Flying qubits propose a totally different paradigm to do quantum calculations. Since flying qubits are mostly independent of hardware, they offer a great flexibility in term of architecture, one example being shown in the figure 5.3. However the research is still at the very beginning, with the first step being the understanding, realization and characterization of the MZI flying qubit beyond the DC measurements.

5.2 Toward flying qubit spectroscopy

We now focus on the MZI and present the result of reference [5]. The bulk of the work has been performed by another PhD student Benoit Rossignol but is presented to be able to understand my participation in this paper. I provided the self-consistent potential that serves as an input to the spectroscopy theory. This work on flying qubit is the continuation of the work done by B. Gaury and J. Weston (see references [79, 87]). They studied the charge oscillations between two wires coupled through a tunnel barrier. Some of their results are shown in Fig. 5.4 and Fig. 5.5. They simulate the propagation of a gaussian pulse through the couple wire system. Fig. 5.4 shows snapshots of the difference between the local density and the equilibrium density for two different values of the tunnel gate voltage. Spreading and oscillations of the propagating pulse between the two wires is clearly visible. To measure a quantity than can be more easily compared to experiment, they raised abruptly the tunnel barrier at a time t_{cut} after the injection of the pulse in order to completely separate the two wires (see Fig. 5.5). By measuring the (normalized) number of particle received at the end of each separated wire as a function of t_{cut}, one can reconstruct a snapshot of the propagation of the pulse in the interferometer. One observes clean sinusoidal oscillations.

However there are two problems if one wants to apply these results to experiments. First, one needs to be able to create extremely sharp pulse (smaller than 10 ps) which is both expensive and challenging. Second, this theoretical is limited to simple systems. This works aims to solve these two problems. By replacing

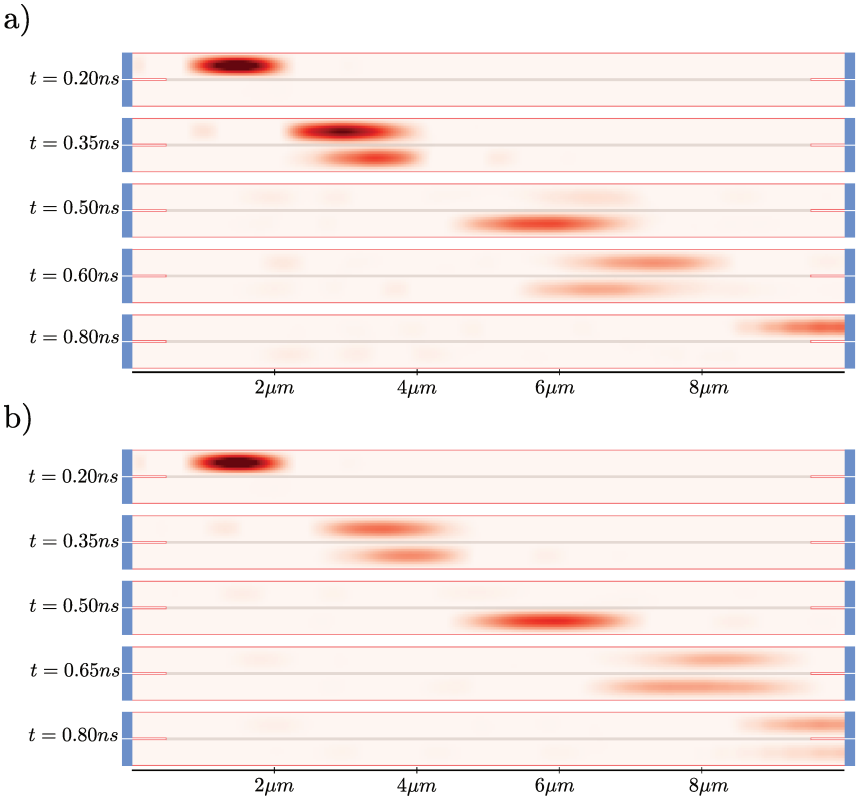

Figure 5.4: Propagation of a pulse through two tunnel coupled wires. A gaussian pulse is sent on the left of the top wire. It then propagates and oscillates between the two wires, which can be seen through snapshots of the difference between the local density and the density at equilibrium. a) and b) correspond to two different values (0.24 mV and 0.34 mV) of the tunneling gate voltage. (From reference [79])

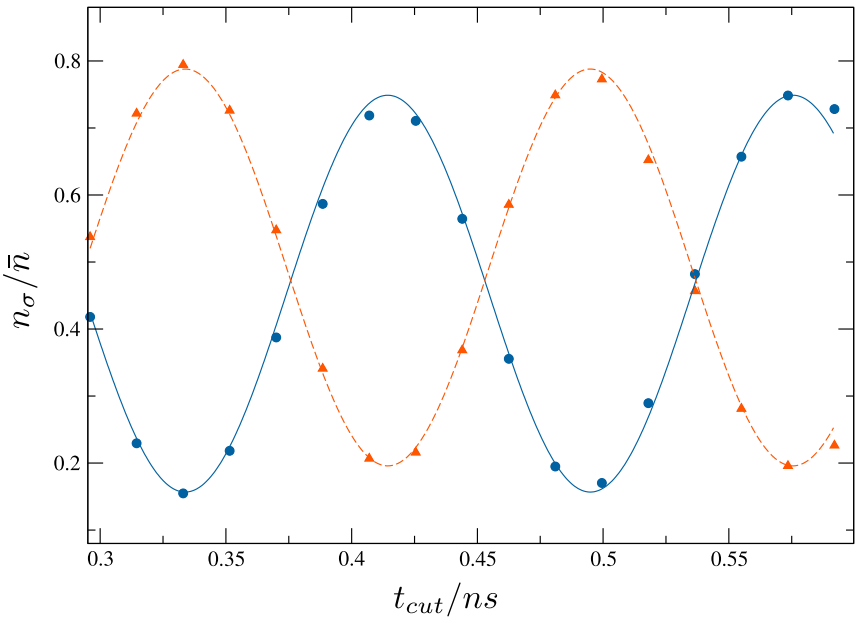

Figure 5.5: Oscillation of the number of particle measured at the end of the top (orange triangles) and bottom (blue circles) normalized by the number of particle injected, as a function of the time at which the coupling between the two wires was cut t_{cut}. The blue and orange cosine line are here to guide the eye. (From reference [79])

short pulses by a sinusoidal drive, one has access to a spectroscopy tool which is both doable experimentally and much simpler numerically. Using the self-consistent solver one can calculate the realistic electrostatic environment of the electrons and thus simulate real systems.

Mach-Zender interferometer for electrons

We focus this study on the tunneling wire flying qubitgeometry sketched in Fig. 5.6 and studied experimentally in reference [5]. The device consists of two quasi-one dimensional wires labeled $\uparrow$ (upper) and $\downarrow$ (lower) connected to four electrodes: two on the left $L_\uparrow, L_\downarrow$ and two on the right $R_\uparrow, R_\downarrow$. Close to the electrodes, the wires are disconnected. However, in a central region of length $\mathcal{L}$, the two wires are in contact so that an electron can tunnel back and forth from the upper and lower part. A capacitive top gate V_g controls the intensity of the tunnel coupling between the wires. The coherent oscillation that takes place in the tunneling region between the upper and lower wire can be interpreted as a quantum gate operated on the flying qubit. Equivalently, an electron entering the upper wire decomposes into a superposition of a symmetric and antisymmetric propagating states which forms a two-path interferometer.

To quickly understand the effect of such an interferometer, lets focus first on DC characteristics (which has already been studied experimentally and theoretically [5]).

An electron injected along ↑ on the left decomposes on the interaction region into Symmetrical and Anti-symmetrical (S/A) components as follow:

$$|\uparrow\rangle = \frac{1}{2}\left(|\uparrow\rangle + |\downarrow\rangle\right) + \frac{1}{2}\left(|\uparrow\rangle - |\downarrow\rangle\right) \rightarrow \frac{1}{\sqrt{2}}\left(|A\rangle + |S\rangle\right) \tag{5.1}$$

The symmetrical and anti-symmetrical components then take-up different phases ϕ_S and ϕ_A while the electron travels in interaction region. As they reach the end of the interaction region, they are projected back to the (↑ / ↓) basis and one can see that a rotation in the Bloch sphere has been performed. In order to be able to use this system as an operational qubit, on first need to understand and predict its behavior when submitted to voltage pulses. What is proposed here is to perform a high frequency spectroscopy of the MZI.

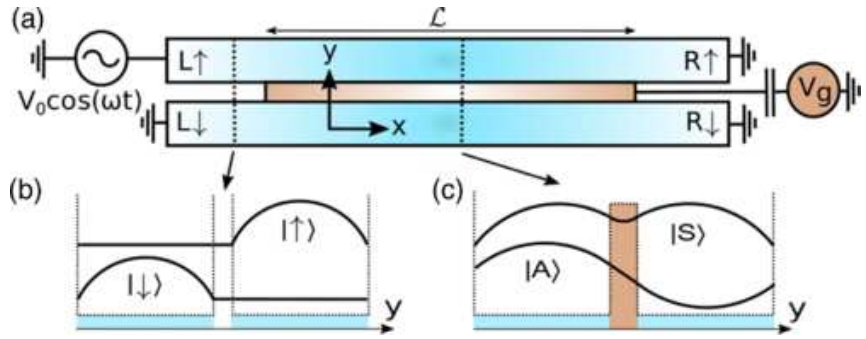

Figure 5.6: (a) Schema of a Mach-Zender interferometer/ flying qubit experiment. A ac voltage drive is imposed on the $L\uparrow$ lead. As it reaches the central region it is coupled to the $L\downarrow$ lead through a tunnel barrier and decomposes into symmetric (S) and anti-symmetric (A) components for a length $\mathcal{L}$. Is is then measured on the $R\uparrow$ and $R\downarrow$ leads. (b) and (c) show the shape of the eigenmodes ($|\uparrow\rangle$ and $|\downarrow\rangle$) in the lead region (b) and ($|S\rangle$ and $|A\rangle$) in the central tunnel region (c). Fig 1 from reference [5]

Introduction to rectification currents

Let us first derive quickly the rectification current that will be used for the spectroscopy. The effect of the time dependent voltage is to dress an incoming wave function of the form $e^{ikx-Et/\hbar}$ with an extra phase factor $e^{-i\Phi(t)}$ (with $\Phi(t) \equiv \int_0^t dt' eV(t')/hbar$) that accounts for the variation of the electric potential. Decomposing this phase into its Fourier components P_n,

$$e^{i\Phi(i)} = \sum_n P_n e^{-i\omega nt} \tag{5.2}$$

the net effect of V(t) is that the incoming wave function is now a coherent superposition $\sum_n P_n e^{ikx-iEt/\hbar-i\omega nt}$ of plane waves at different energy. As different energy

get transmitted into different channels, we arrive at the following time dependent transmission amplitude for an incoming energy E,

$$d_{ba}(tE) = \sum_n P_n d_{ba}(E + n\hbar\omega) e^{-iEt/\hbar - i\omega nt} \tag{5.3}$$

where $d_{ba}(t, E)$ is the Fourier transform with respect to E' of $d_{ba}(E', E)$ which is itself the inelastic amplitude to be transmitted from energy E, lead a toward energy E', lead b. The generalization of the Landauer formula of time dependent currents provides the time dependent current $I_b(t)$ as

$$I_b(t) = \frac{e}{\hbar} \int \frac{\mathrm{d}E}{2\pi} \left[|d_{ba}(t, E)|^2 - |d_{ba}(E)|^2 \right] f_a(E) \tag{5.4}$$

where $f_a(E)$ is the Fermi function of the lead a subjected to the time dependant voltage. The second term in the previous equation subtracts the current sent from the lead a in the absence of time-dependent voltage which is a convenient way to ensure the overall current conservation. Focusing on the DC (rectification) current $\bar{I}_b = 2\pi \int_0^{2\pi/\omega} \mathrm{d}t\, I_b(t)$ we arrive at,

$$\bar{I}_b(t) = \frac{e}{\hbar} \sum_n |P_n|^2 \int \mathrm{D}E\, |d_{ba}(E)|^2 [f_a(E + n\hbar\omega) - f_a(E)] \tag{5.5}$$

equation 5.5 is very general and relates the rectification properties of an arbitrary mesoscopic system to its scattering matrix $d_{ba}(E)$, a well known DC object. In particular, it can be easily evaluated numerically for a large class of microscopic models using readily available numerical packages (in our case the Kwant package) for arbitrary periodic pulses.

However in order to simulate realistic systems, one needs first to calculate accurately the electrostatics of this model, which is where our algorithm comes into play.

Realistic model of the MZI and self consistent calculations

Geometry

The model is defined solely by the position of the top gates that are deposited on the surface of the GaAs heterostructure. It consists of a central region (defined by two lateral gates and a central tunneling gate) which smoothly evolves into two disconnected wires on the left and on the right of the central region. A top view of the layout of the gates is shown in Fig. 5.7. A cut at $x = 0$ (left panel) and $x > 10\,\mu$m (right panel) is shown in the upper panel of Fig. 5.8.

The dimensions of the device (with a central region $13.8\,\mu$m long and $0.92\,\mu$m large) are fully compatible with standard e-beam lithography techniques. The different gates are grouped into three categories: the three interior gates (green) are set to the same potential V_t, the two outer gates of the central region are set to V_m and the four outer gates of the electrodes are set to V_l. The transition region

between the central region and the lead ($x \in [-9.2, -6.9]$ and $x \in [6.9, 9.2]$ μm) is defined by an interpolation described later in this section.

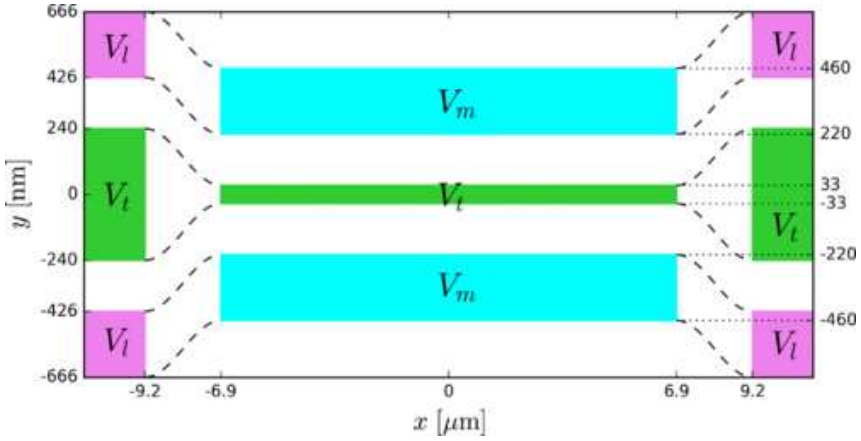

Figure 5.7: Top view of the gates of the realistic model. Two regions can be identified: the leads on the left and right, and the central region. Each region is supposed to be infinite. For the current calculations, interpolation is performed between the regions (dashed lines). Fig 5 from reference [5]

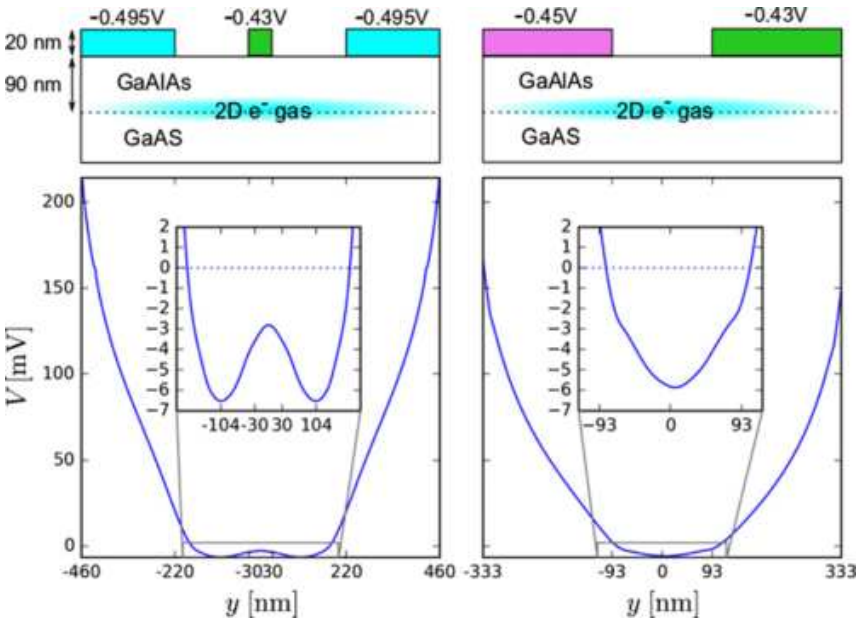

Figure 5.8: Side view of the simulation system, in the center region (left) and in the lead (right). The bottoms show the self consistent potential with a zoom around the Fermi level $V = 0$V as inset. Fig 6 from reference [5]

Self-consistent model

In order to calculate the electrostatic potential seen by the two-dimensional electron gas, we work in the effective mass ($m^* = 0.067\, m_e$, m_e: bare electron mass) approximation for the Schrödinger equation which is solved self-consistently with Poisson equation. The Hamiltonian of the two dimensional electron gas,

$$H = \frac{P_x^2 + P_y^2}{2m^*} - eV(x, y, z = 0), \tag{5.6}$$

is discretized on a square grid with lattice constant $a = 3\,\mathrm{nm}$ (approximately $2{\times}10^6 \approx 300 \times 6000$ sites). The Schrödinger equation

$$H\Psi_{\alpha E} = E\Psi_{\alpha E} \tag{5.7}$$

is solved using the Kwant package [2]. The electrodes are taken to be semi-infinite so that the spectrum is actually continuous and the eigenfunctions labeled by an energy E and a mode index α. The density of electrons $n(x, y)$ is given by the integral over energy of the local density of states,

$$n(x, y) = \sum_\alpha \int \frac{dE}{2\pi} |\Psi_{\alpha E}(x, y)|^2 f(E) \tag{5.8}$$

where $f(E) = 1/(e^{E/k_BT} + 1)$ is the Fermi function at temperature T (and we have set the Fermi energy $E_F = 0$ as our reference energy point). The Poisson equation away from the electron gas reads

$$\Delta V(x, y, z) = 0 \tag{5.9}$$

while close to the gas the discontinuity of the electric field is set by $n(x, y)$:

$$\partial_z V(x, y, 0^+) - \partial_z V(x, y, 0^-) = -\frac{e}{\epsilon}[n(x, y) + n_d] \tag{5.10}$$

where the dopant density n_d sets the actual density of the gas and $\epsilon \approx 12\epsilon_0$ is the dielectric constant. The Poisson equation is solved using the FEniCS package [88]. (These calculation were performed before we developed our own Poisson solver. To obtain a mixed solver as needed for our algorithm, we calculate the capacitance matrix of the system as the inverse of the Greens function of the Poisson equation).

In order to solve the set of self-consistent equations (5.7, 5.8, 5.9, 5.10), we perform one approximation which considerably lowers the computational effort while retaining good accuracy. In a first step, we solve the self-consistent problem deep in the lead region where the system is invariant by translation along x (hence effectively maps onto a 2D problem for the Poisson equation and 1D for the quantum problem). We obtain $V(|x| \gg 10, y, 0) \equiv V_A(y)$. Secondly, we solve the problem deep inside the central region, assuming that the potential is not affected by the leads (hence also invariant by translation along x). We obtain $V(|x| \ll 10, y, 0) \equiv V_B(y)$. An example

of the obtained self-consistent potentials $V_B(y)$ (left) and $V_A(y)$ (right) is shown in Fig. 5.8 for $V_t = -0.43\,\mathrm{V}$, $V_m = -0.495\,\mathrm{V}$ and $V_l = -0.45\,\mathrm{V}$. In the last step, we describe the potential in the transition regions ($x \in [-9.2, -6.9]$ and $x \in [6.9, 9.2]$) by performing an interpolation between $V_A(y)$ and $V_B(y)$. The density of the gas is $\sim 3.2 \times 10^{11}\,\mathrm{cm}^{-2}$ which corresponds to a Fermi wave length $\lambda_F \approx 45\,\mathrm{nm}$.

Spectroscopy of the Flying qubit

We do not discuss here the result of the spectroscopy as it was done by the author of the article (complete discussion in [5]). We just show here some of the result that were obtained by using the self-consistent potential into the Kwant solver to calculate the scattering matrix of the system. From this scattering matrix, the rectification current $\bar{I}$ and its derivative can be obtained. A color map of this derivative is shown in Fig. 5.9 first for a simple analytical case and for the realistic geometry. (Time dependant calculations where also performed in the article which matched with static theory). One observes oscillations of the rectified current with the tunnel voltage or of the frequency of the sinusoidal drive. The period of these oscillations corresponds to the time of flight τ of the flying qubit. One period can be identified in the plot of the realistic system (bottom of Fig. 5.9) corresponding to the slowest channel with $\tau = 220$ ps. Another much smaller period can be identified in the inset, corresponding to $\tau = 19$ ps. It is possible to obtain the same type of curve from experimental measurement, and thus caracterize the MZI in view of creating a flying qubit.

Conclusion

In this section we have seen that the correct treatment of the electrostatics is the link that allows one to directly connect the microscopic model with the effective model used in quantum transport theories. In this particular example, we linked directly the experimental parameters (gate voltages) to the high frequency transport calculations. In the next chapters, we will use this same link on a quantity that is experimentally measured: the propagation velocity of plasmon excitations.

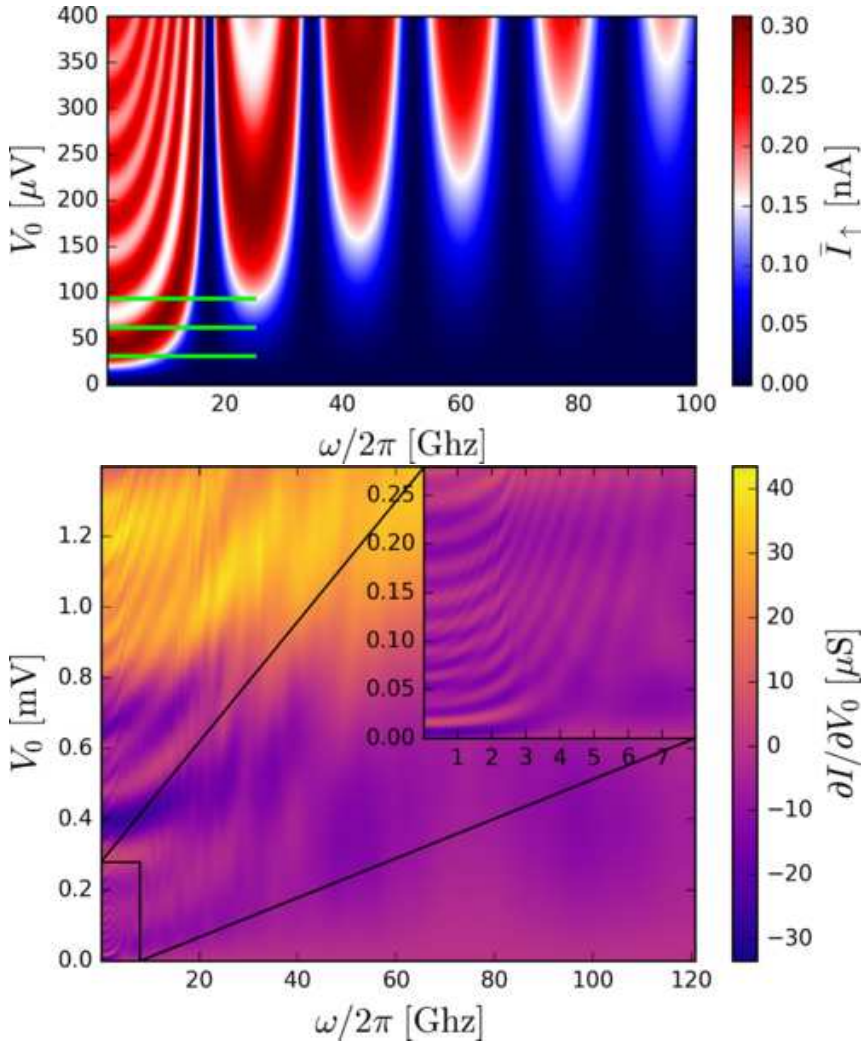

Figure 5.9: Rectified current derivative $\partial \bar{I}/\partial V_0$ as a function of the frequency of the drive $\omega/2\pi$ and the voltage in the tunnel gate V_0. The inset is a zoom on the lower left part. The oscillation pattern allows to extract the time of flight difference τ. The top panel shows analytical calculations on a simplified model for comparison (see reference [5]). Rectified current Fig 2 Vs 10 from reference [5]

6

Time of flight experiment

One important step toward the experimental realization of a flying qubit is to understand how a flying qubit propagates. More precisely in our case, how fast the collective excitation created by a short tension pulse propagates inside a quasi one-dimensional wire. This chapter summarizes the findings of the article [6] where they measured experimentally the velocity of a surface plasmon inside a narrow channel. These observed velocities were also calculated analytically in the two next chapter. We will show a good agreement between the calculated velocities and experimental ones.

6.1 Description of the experiment

In this experiment, the objective is to measure the velocity of a surface plasmon propagating in wire. In order to access it, they measured the time that it takes for a pulse to travel a known distance (time of flight). To do so, they use quantum point contacts (QPCs) as dynamical switches. In a nutshell: if the switch is closed when a pulse arrives, it is blocked and no current is measured at the end of the wire. Conversely if the switch is opened for the pulse, a current is measured. By playing with the delay between the injection of a pulse and the closing of the switch, they can extract a time of flight.

The sample

The sample in this experiment is once again based on a GaAs/AlGaAs wafer producing a high mobility 2DEG at the interface. A schema of the experiment is shown in Fig. 6.1. Two ohmic contacts at the extremities allow to inject and receive voltage pulses. Two long side gates with adjustable voltages V_{SG} allow to create a quasi-one

dimensional wire with adjustable width (the width depends on the gate voltage). Along the wire, 3 measurement QPC ($QPC_1, QPC_2 \,\&\, QPC_3$) used as fast switch, situated at $15, 30, 70$ μm of the left ohmic contact allow to perform the time of flight measurement. Another QPC, QPC_0 at $6\,\mu$m of the ohmic contact can be used for mode selection. An arbitrary wave generator allows to send short pulses (~ 70 ps) simultaneously in the injection ohmic contact and in the measurement QPC ($QPC_1, QPC_2 \,\&\, QPC_3$) with an adjustable delay.

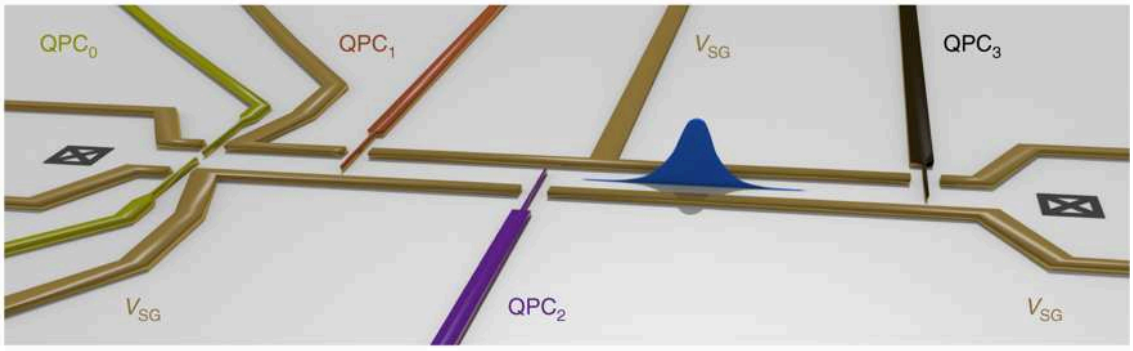

Figure 6.1: Schematic of the time of flight measurement experiment (surface view). Short pulses are injected on a left ohmic contact, then propagate along a wire created by two site gates. Along the wire are quantum point contacts allowing for the velocity measurements. Finally the pulse is received at right ohmic contact. From Roussely2018

The time resolved method

Surface plasmons in a wire are fast, typically of the order of 10^5 m.s^{-1}. Since typical experiment have a size of around $100\,\mu$m, the propagation time will be of the order 100 ps. Hence, the pulse needs to be extremely short (l100 ps or 0.01 THz) not to cover the entire experiment. Direct time resolved measument is possible up to the Ghz frequencies. At the scale corresponding to this experiment (almost THz), one needs to use indirect measures. The strategy of reference [6] for the precise measurement of the velocity is the following. A voltage pulse is produced at the left ohmic contact (left cross in Fig. 6.1) at time $t = 0$. At this moment tuned bellow the pinch off regime (closed QPC) by applying a constant negative voltage V_{DC}. If nothing is done, the pulse will bounce back as it reaches the QPC and no differential conductance will be measured. After a time t, a short pulse (~ 70 ps) V_{AC} is sent the QPC. As a result, the QPC is opened for a short amount of time $\ll 70$ ps (see Fig. 6.2). If the time t coincides with the time of flight of the pulse between the ohmic contact and the QPC, a fraction of the pulse we pass throught the QPC, otherwise it will be totally reflected. By sweeping the delay between the emission at the ohmic contact and the emission of the V_{AC} pulse, one can reconstruct the shape of the pulse at the QPC (see Fig6.3 for a plot of the normalized amplitude of

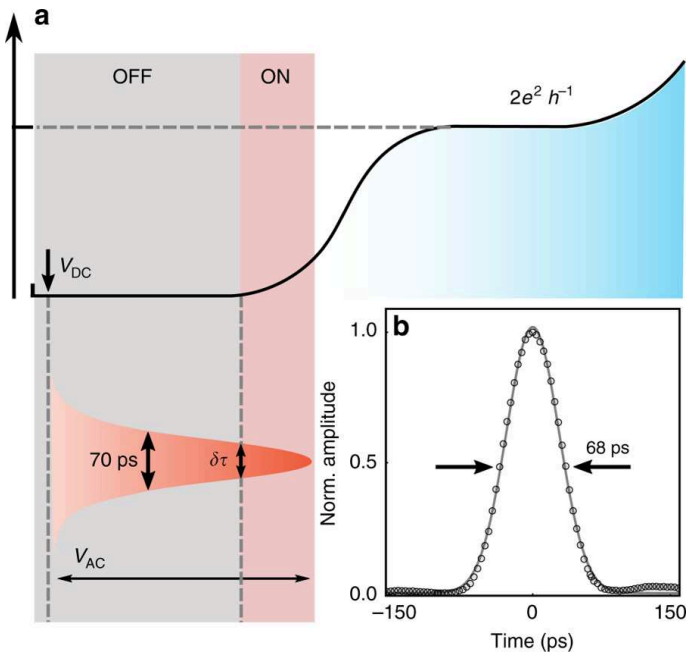

Figure 6.2: Operating the QPC fast switch for pulse reconstruction. (a) the QPC is tuned bellow the pinch off with V_{DC}. A fast pulse V_{AC} is applied, that opens shortly the QPC allowing current to flow through. top: conductance of the QPC as a function of the gate voltage, bottom: shape of the fast pulse sent to the QPC (time Vs magnitude). (b) varying the delay between the pulse in the ohmic contact and the V_{AC} short pulse, on can reconstruct the shape of the pulse at the QPC. (from [6])

the pulse as a function of time). By plotting the time corresponding to a maximum of amplitude for all three QPCs, as a function of the distance between the ohmic contact and the QPCs, one can extract the velocity of the plasmons.

6.2 Results : measurement of the renormalized velocities

As explained above, the propagation velocity of the charged collective mode can be extracted from the experiment. They are found to be dependent on the gate voltage (Fig. 6.4 (a)). These velocity are shown as a function for the side gate voltage V_{SG} and compared with numerical simulations (see blue curve of Fig. 6.4 (b)). We found a very good agreement between experiment and the parameter-free simulations. Compared to the theoretical Fermi velocity (see the chapters 7 and 8) presented in black dashed lines, they appear to be around 5 time larger. One also sees that these velocities decrease with a decreasing voltage (increasing magnitude

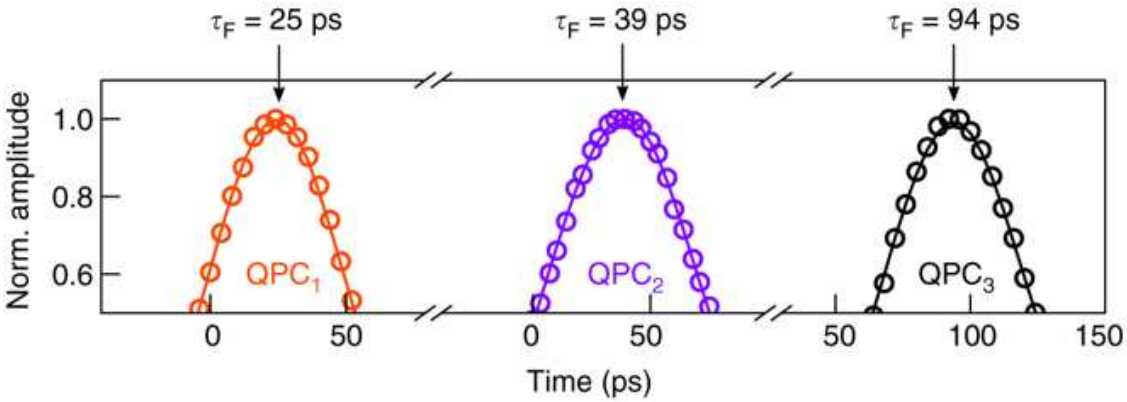

Figure 6.3: Pulse reconstruction at the 3 QPC. The time of flight is measured as the delay between the pulse send to the ohmic contact and the pulse sent to the QPCs. Knowing the distances between the ohmic contact and the QPCs, the velocity can be extracted. (from reference [6])

of the negative voltage), which corresponds to a decrease of the number of open channels in the wire.

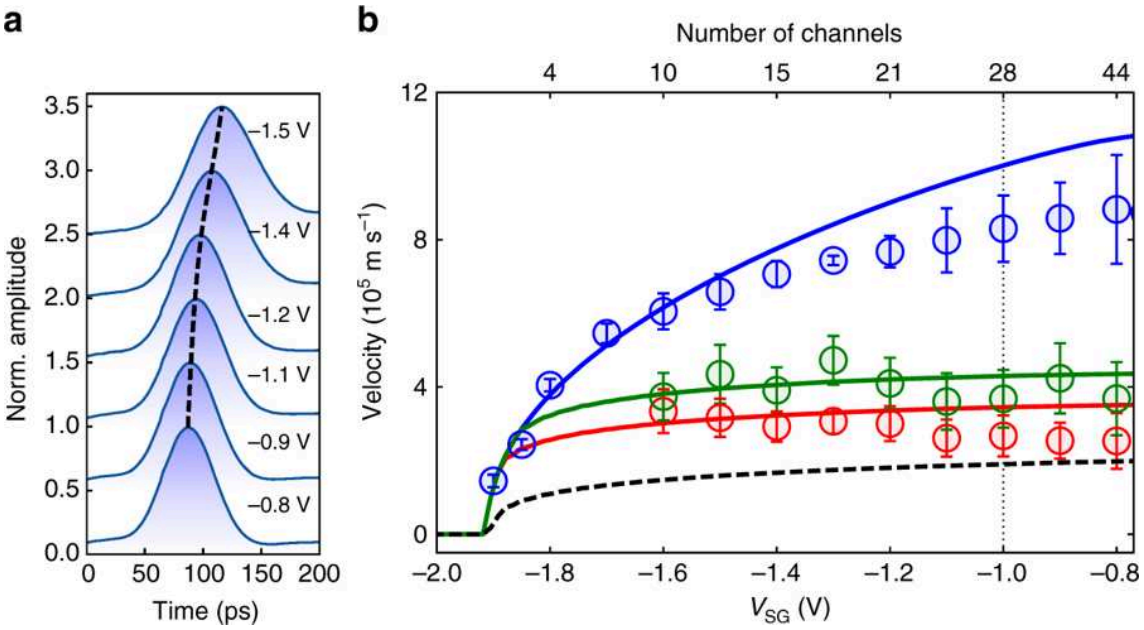

Figure 6.4: (a) Reconstruction of the pulses in time for different gate voltages. (b) Plasmon velocities as a function of the gate confinement. The circles are the experimental measurements with their error bars, the solid lines are the results from our parameter free theory calculations. In blue the QPC_0 is opened, in red and green the QPC_0 is respectively at the first and second plateau. The dashed black lines shows the Fermi velocity calculated from the simulations. (from reference [6])

In order to investigate the effect of mode selection on the plasmon velocity, a QPC (QPC_0) has been placed just after (6 nm) the left ohmic contact. The characteristic curve of QPC_0 is shown in Fig. 6.5 (a). By sitting in the first (second) conductance plateau one can select to inject only the first (two first) modes in term of kinetic energy. This changes the velocity and is shown in the red (green) experimental points in Fig. 6.4 (b) with once again a good agreement with the theory. The more modes are included, the highest the velocity is. Moreover, when the modes are selected, the velocity is more or less independent of the gate voltage. Measure have also been made at fixed $V_{SG} = -1$V, continuously changing the QPC_0 voltage (c), once again with a good agreement with theory. They corroborate the previous observation that the velocity increases with increasing gate voltage (less confinement, so fewer modes can pass).

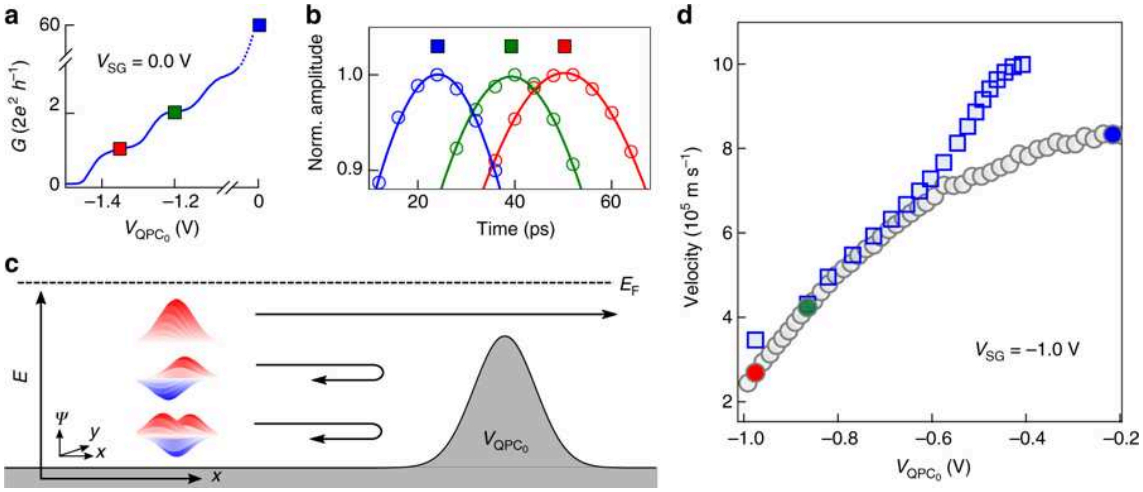

Figure 6.5: Mode selection at QPC_0. By changing the voltage applied to QPC_0 one can select the number of modes (a), as the low energy modes can not pass through the potential barrier (c). The reconstructed pulse for one, two and all modes are shown in (b). In (d), the velocity as a function of the QPC_0 voltage is shown at fixed gate voltage $V_{SG} = -1$V, experimental measures are the gray circles and the results of our parameter free simulations are in blue squares. (from reference [6])

conclusion

We have seen in this chapter that the group of C. Bauerle were able to measure the velocity at which a tension pulse propagates as a function of the gate induced latteral confinement. As we showed, we could also predict accurately these velocities. In the next two chapters, we will explain how these predictions were made

7

Theory of plasmon propagation

In this chapter, we describe a simple microscopic theory for the collective excitations of an electron gas. The electrons are described by a collisionless Boltzmann equation subject to an electric field that is self-consistently generated by the electrons themselves. Despite its simplicity, this semi-classical theory captures the salient features of many differnet regimes. In two dimension, we recover the standard theory for surface plasmons. In one dimension, we recover the correct expression for the dispersion relation of the Luttinger liquid, its intrinsic conductance and the phenomena of spin charge separation. In quasi-one dimension, we obtain a multi-channel theory that describes the crossover between the above two limits. An important aspect of our semi-classical theory is that it is expressed in term of microscopic (not effective) parameters, and is therefore amenable to ab-initio numerical calculations that can be directly compared to experiments.

7.1 Formulation of the Self-consistent Boltzmann-Poisson problem

Let us introduce the semi-classical probability distribution $f(\vec{x}, \vec{k}, t)$ for an electron to be at position $\vec{x}$ and momentum $\vec{k}$ at time t. We consider ballistic samples, so that $f(x, k, t)$ satisfies a collisionless Boltzmann (Liouville) equation, which expresses the conservation of the probability to find an electron at position x and k plan:

$$\frac{\partial f}{\partial t} = -\vec{v}_{\vec{k}}.\vec{\nabla}_{\vec{x}} f - \frac{e}{\hbar}\vec{\mathcal{E}}(\vec{x}, t).\vec{\nabla}_{\vec{k}} f \tag{7.1}$$

where the group velocity $\vec{v}_{\vec{k}} \equiv (1/\hbar)\vec{\nabla}_{\vec{k}} E(\vec{k})$ arises from the non-interacting dispersion relation of the electrons and $\vec{\mathcal{E}}$ is the electric field in the sample. The electronic density (per spin) is given by

$$n(\vec{x}) = \int \frac{d^d k}{(2\pi)^d} f(\vec{x}, \vec{k}, t) \tag{7.2}$$

The set of equations is made non trivial by the Poisson equation that self-consistently links the electric field to the electronic density, hence making the problem non-linear: $\vec{\mathcal{E}} = \vec{\nabla} V$ where the electric potential verifies,

$$\Delta V = \frac{se}{\epsilon} n(\vec{x}, t). \tag{7.3}$$

where $s = 2$ is the spin degeneracy. Note that while we will concentrate on $1 \leq d \leq 2$ for the electronic degrees of freedom, the Poisson equation should always be understood as a 3D problem.

To study plasmon propagation, we will focus on situations where the system is initially described by a Fermi distribution and the plasmons induces a small perturbation:

$$f(\vec{x}, \vec{k}, t) = f_0[E(\vec{k})] + f_1(\vec{x}, \vec{k}, t) \tag{7.4}$$

where $f_0(E) = 1/[e^{(E-E_F)/kT} + 1]$ (E_F: Fermi energy) and $f_1(\vec{x}, \vec{k}, t) \ll f_0$ vanishes in equilibrium. Likewise, the electronic density $n(\vec{x}, t) = n_0(\vec{x}) + n_1(\vec{x}, t)$ decomposes into an equilibrium $n_0(\vec{x})$ and out-of equilibrium $n_1(\vec{x}, t)$ part.

Equations (7.1),(7.2),(7.3) and (7.4) form the self-consistent Boltzmann-Poisson problem

7.2 Application to plasmons in one and two dimensions

Our first example is a 2D electron gas in the $\vec{x} = (x, y)$ plane ($z = 0$). We suppose that two infinite metallic gates are present in the $z = \pm d$ plane and screens the charged electronic excitations. We seek solutions of the form

$$\begin{aligned} f_1(\vec{x}, \vec{k}, t) &= f_1(\vec{k}) e^{i\vec{q}.\vec{x} - i\omega t} \\ n_1(\vec{x}, t) &= n_1 e^{i\vec{q}.\vec{x} - i\omega t} \end{aligned} \tag{7.5}$$

It should be stressed that $\vec{k}$ and $\vec{q}$ refer to totally different concepts. $\vec{k}$ is the usual momentum of the electrons wave functions whereas $\vec{q}$ is the momentum of the plasmon (the momentum of the oscillating probability of presence of electrons).

Electrostatic problem

Supposing that there is no static charge in the system, the electric potential takes the form

$$V(\vec{x},t) = V_1 e^{i\vec{q}.\vec{x}-i\omega t}u(z). \tag{7.6}$$

Poisson equation imposes $-q^2u(z)+u''(z)=0$ which implies $u(z) = \mp\sinh(qz\mp qd)/\sinh(qd)$ where $\pm$ refers to the upper ($z>0$) and lower ($z<0$) half space. The boundary condition at $z=0$ reads $V_1[u'(z=0^+)-u'(z=0^-) = sen_1/\epsilon$ so that we arrive at $V_1 = -(sen_1)\tanh(qd)/(2\epsilon q)$. The electric field in the $z=0$ plane eventually reads,

$$\vec{\mathcal{E}}_1 = -i\frac{\vec{q}}{q}\frac{sen_1}{2\epsilon}\tanh(qd) \tag{7.7}$$

If the two metallic gates are situated at two different distances d_1 and d_2, one simply substitutes $2/\tanh(qd)$ by $1/\tanh(qd_1)+1/\tanh(qd_2)$ in the above expressions as well as in all that follows.

In 3D,

$$\vec{\mathcal{E}}_1 = -i\frac{\vec{q}}{q^2}\frac{sen_1}{\epsilon} \tag{7.8}$$

Capacitive limit $sen_1 = CV_1$. With $C=\epsilon/d$ for a planar capacitor.

$$\vec{\mathcal{E}}_1 = -i\vec{q}\frac{sen_1}{C} \tag{7.9}$$

Which can also be obtained directly from the long wave length limit of Eq.(7.7).

Boltzman problem.

Using the ansatz Eq.(7.5) and linearizing the Boltzmann equation to first order in f_1, we arrive at the explicit form

$$f_1(\vec{k}) = i\frac{e\ \vec{\mathcal{E}}_1.\vec{v}_{\vec{k}}}{\omega-\vec{v}_{\vec{k}}.\vec{q}}\left(-\frac{\partial f_0}{\partial E}\right) \tag{7.10}$$

At zero temperature, which we assume from now on $-\partial f_0/\partial E$ is simply a Dirac function and one can perform the integral over $\vec{k}$. Noting θ the angle between $\vec{q}$ (or $\vec{\mathcal{E}}$) and $\vec{k}$, we get for an isotropic band dispersion in two dimensions:

$$\begin{aligned} n_1 &= i\frac{e\mathcal{E}_1 k_F}{\hbar(2\pi)^2}\int_0^{2\pi}\frac{d\theta\cos\theta}{\omega-v_F q\cos\theta} \\ &= i\frac{e\mathcal{E}_1 k_F}{\hbar 4\pi v_F q}\left(\frac{1}{\sqrt{1-(v_F q/\omega)^2}}-1\right) \end{aligned} \tag{7.11}$$

And in one dimension:

$$n_1 = i\frac{e\mathcal{E}}{\hbar 2\pi}\frac{2v_F q}{\omega^2 - (v_F q)^2} \tag{7.12}$$

Self-consistent problem in two dimensions

Putting together the Boltzmann condition in 2d (equation 7.11) and the Poisson condition for one gate (equation 7.7), we arrive at the self-consistent condition,

$$\frac{se^2 k_F}{4\pi\epsilon\hbar v_F q}\tanh(qd)\left(\frac{1}{\sqrt{1-(v_F q/\omega)^2}} - 1\right) = 1 \tag{7.13}$$

Introducing the fine structure constant $\alpha_F = e^2/(4\pi\epsilon\hbar v_F)$ and the plasmon velocity $v_P = \omega/q$, one arrives at

$$\frac{v_P}{v_F} = \frac{\xi + 1}{\sqrt{2\xi + 1}} \tag{7.14}$$

where we introduced ξ

$$\xi = s\alpha_F k_F \frac{\tanh(qd)}{q} \tag{7.15}$$

When screening is possible (d is small) this expression has two limited values. At large wave length $qd \ll 1$ we find $\xi = s\alpha_F k_F d$ and the plasmon velocity is enhanced with respect to the Fermi velocity. At short wave length $qd \gg 1$ $\xi \to 0$ and $v_P \to v_F$. Except for $qd \sim 1$ the dispersion relation is well represented by a linear dispersion relation $\omega = v_P q$. Another interesting limit is when $d \to \infty$. This corresponds to the absence of metallic gate, which is relevant for bulk 2D experiment. In that case, in the long wave length limit, $\xi \to \infty$ and the plasmon velocity diverges. Therefore, in order to get reasonable velocities, one needs to confine the system in order to create a quasi one-dimensional system.

7.3 Application to quasi-one dimensional plasmons

We now seek to extend our previous findings to the case of quasi-one dimensional plasmons, which is the relevant case for the experiment of C. Bauerle's group (chapter 6). To do so we explicitly break the translational invariance along y by confining the 2D system in the y direction, perpendicular to the plasmon propagation x. This open independent modes in the y direction that we label by α.

self-consistent calculations

The non equilibrium density can be separated between longitudinal (x) and transverse (y) directions:

$$n^1(x,y) = \sum_\alpha |\psi_\alpha(y)|^2 n^1_\alpha(x) \tag{7.16}$$

where $\psi_\alpha(x)$ is the wave function in the of the 1D problem in the y direction and $n^1_\alpha(x) = \int \frac{\mathrm{d}k}{2\pi}\ f^1_\alpha(x,k)$. We obtain a list of the independent Boltzmann problems similar to the previous section and get a solution for all modes

$$n^1_\alpha = i\frac{e\mathcal{E}_\alpha}{\hbar 2\pi}\frac{2v_\alpha q}{\omega^2 - (v^F_\alpha q)^2} \tag{7.17}$$

where v_α is the Fermi velocity of the mode α. In presence of an electrostatic gate and in the long wave length limit ($qd \gg 1$) the density is fully screened on a scale $1/q$. This translated into the fact that the capacitance was independent of q (see 7.2.1). In the same limit we can write the following equation as a definition of a Green's function of the Poisson equation:

$$V_1(y) = \int \mathrm{d}y\ G(y,y')\, s\, n_1(y) \tag{7.18}$$

where the Green's function $G(y,y')$ is independent of q. Finally we arrive at an expression for the average electric field felt by a mode α:

$$\mathcal{E}_\alpha = s\sum_\beta \mathcal{G}_{\alpha\beta}\ n^1_\beta \tag{7.19}$$

where we defined the integrated Green matrix

$$\mathcal{G}_{\alpha\beta} \equiv \int \mathrm{d}y\mathrm{d}y'\, |\psi_\alpha(y)|^2 G(y,y') |\psi_\beta(y')|^2 \tag{7.20}$$

The self consistency is found by injecting $\mathcal{E}_\alpha$ into equation 7.17. After some algebra this gives

$$\frac{\omega^2}{q^2} n^1_\alpha = \sum_\beta \left(v^2_\alpha \delta_{\alpha\beta} + \frac{se}{2\pi\hbar} v_\alpha \mathcal{G}_{\alpha\beta} \right)\ n^1_\beta \tag{7.21}$$

where $\delta_{\alpha\beta}$ is the Kronecker symbol. The plasmon velocities ω/q are then given by getting the eigenvalue of the matrix in the right hand side. By introducing $\widetilde{n}_\alpha$ such that $n_\alpha = \widetilde{n}_\alpha\sqrt{v_\alpha}$, we recover a similar equation as the equation Eq. (11) of Matveev and Glazman [66].

Infinite range interaction limit

To get an intuitive understanding of this equation let us look at the limit where $se/(2\pi\hbar)\mathcal{G}_{\alpha\beta} = g,\ \forall\alpha,\beta$ with g the interaction strength. This corresponds to an interaction with an infinite range, that is, where each electrons interact with all electrons in the same way. Dropping the exponent for the densities for readability, equation 7.21 reads:

$$v_p^2 n_\alpha = \sum_\beta \left(v_\alpha^2 \delta_{\alpha\beta} + g v_\alpha X_\beta^T\right)\ n_\beta \tag{7.22}$$

where $v_p = \omega/q$ is the plasmon velocity, $X^T = (1, \ldots, 1)$ is the constant diagonal vector. By introducing the eigenvector P and $a = X^T P = \sum_\alpha P_\alpha$ and replacing into Eq. 7.22 we arrive at the following equation for the eigenvector P

$$P_\alpha = \frac{g a v_\alpha}{v_p^2 - v_\alpha^2} \tag{7.23}$$

Summing on all α we finally obtain:

$$\sum_\alpha \frac{v_\alpha}{v_p^2 - v_\alpha^2} = \frac{1}{g} \tag{7.24}$$

This equation can be solved graphically. Lets define $F(v) = \sum_\alpha v_\alpha/(v^2 - v_\alpha^2)$. As shown in fig. 7.1, F is a piecewise continuous function on intervals $]-\infty, v_0]$, $[v_\alpha, v_{\alpha+1}]$ and $[v_N, \infty[$ that diverges as v_p reaches v_α. The equation $F(v) = 1/g$ has one solution on each closed interval which is therefor bounded. For example on the interval α: $v_p l v_\alpha l v_{\alpha+1}$. The solution on the last semi-open interval is not bounded. This means that one eigenvalue of the problem can be much bigger (and in practice is) than the other, that are very close to the non interacting velocities v_α. The large one is the plasmon velocity.

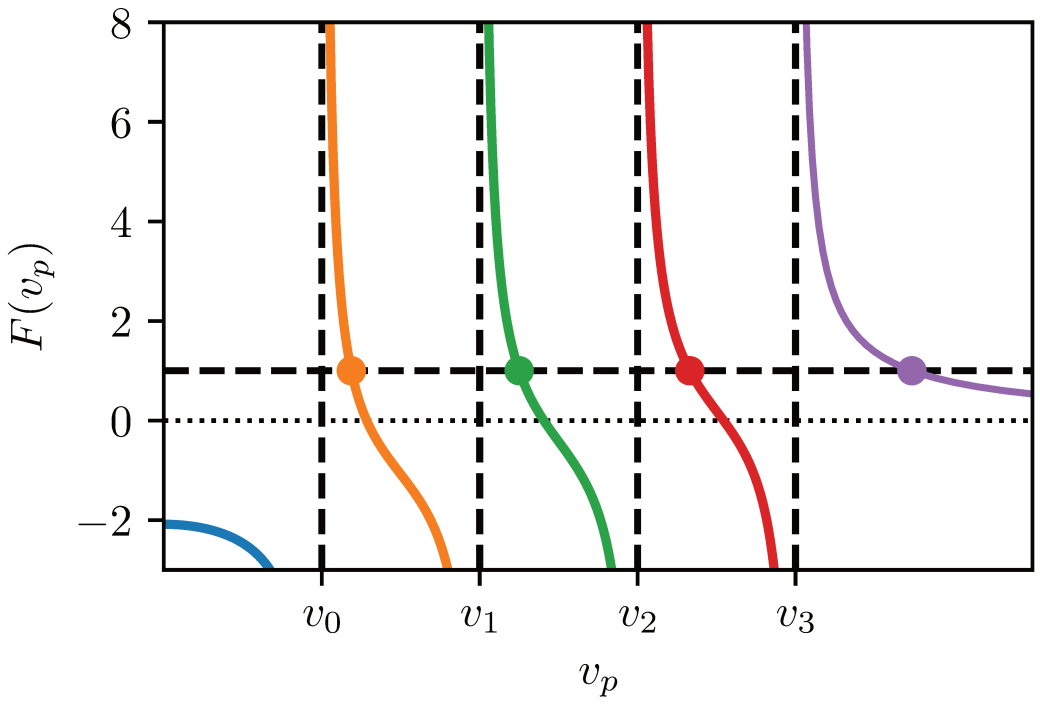

Figure 7.1: Graphical resolution of the equation $F(v_p) \equiv \sum_{\alpha=0}^{4} v_\alpha/(v_p^2 - v_\alpha^2) = 1/g$ (Eq. 7.24), here with $\{v_\alpha\} = \{1, 2, 3, 4\}$ and $g = 1$. The solution of the equation are the intersection of between the curve of F and the horizontal dashed line $1/g = 1$. This equation has 4 solutions, the three first being respectively bounded by $[v_0, v_1], [v_1, v_2], [v_2, v_3]$. The last solution can be arbitrarily large for large g.

8

Numerical calculation of plasmons velocity

We summarize here the method and result of the simulation of the plasmon velocity (from the supplementary material of [6].)

8.1 Self consistent calculations

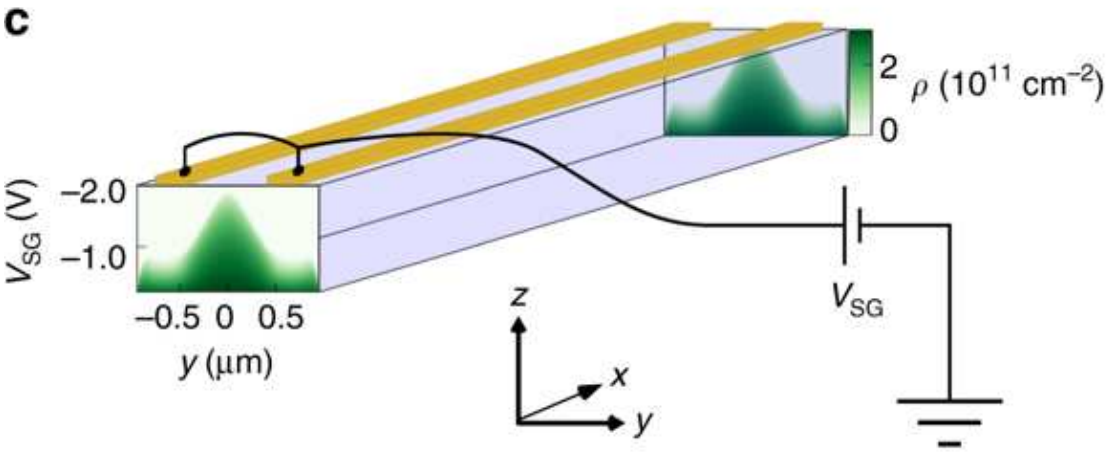

Figure 8.1: Illustration of the sample geometry used for the self-consistent calculations. The quasi one-dimensional quantum wire is defined by two long electrostatic gates at potential V_{SG} and considered as infinite in the x direction. The colored images, one at the beginning of the wire and another at the end, are cross sections of the electron density profile along the y-axis as a function fo te gate voltage. From reference [6]

A sketch of the system used in our simulations is shown in Fig. 8.1. We consider a 3D system with translational invariance along the x direction and with the 2D electron gas situated at $z = 0$. The two top gates, situated at $z = 140\,\mathrm{nm}$ are used for defining the quasi-one dimensional wire, but also provide screening to the electron gas.

Our starting point is a many-body Hamiltonian that describes our 2D electron gas,

$$H = -\frac{\hbar^2}{2m^*}\sum_\sigma \int d^2\vec{r}\; c^\dagger_{\vec{r}\sigma}\Delta c_{\vec{r}\sigma} + \sum_\sigma \int d^2\vec{r}\; U(\vec{r}) c^\dagger_{\vec{r}\sigma} c_{\vec{r}\sigma} + \sum_{\sigma\sigma'}\int d^2\vec{r} d^2\vec{r}' c^\dagger_{\vec{r}\sigma} c_{\vec{r}\sigma} G(\vec{r},\vec{r}') c^\dagger_{\vec{r}'\sigma'} c_{\vec{r}'\sigma'} \tag{8.1}$$

where the fermionic operator $c^\dagger_{\vec{r}\sigma}$ ($c_{\vec{r}\sigma}$) creates (destroys) an electron at position $\vec{r} = (x, y)$ and with spin σ, m^* is the effective mass, Δ the 2D Laplacian operator, $U(\vec{r})$ an electrostatic potential and $G(\vec{r}, \vec{r}')$ the electron-electron interaction. In free space, $G(\vec{r}, \vec{r}')$ is simply given by the bare Coulomb repulsion $G(\vec{r}, \vec{r}') = \frac{e^2}{4\pi\epsilon|\vec{r}-\vec{r}'|}$. However, here, the presence of the electrostatic gates provides some screening, and $G(\vec{r}, \vec{r}')$ is the solution of the 3D Poisson equation (restricted to the 2D gas),

$$\Delta_{3D} G(\hat{r}, \hat{r}') = -\frac{e^2}{\epsilon}\delta(\hat{r} - \hat{r}') \tag{8.2}$$

with the boundary condition $G(\hat{r}, \hat{r}') = 0$ when the 3D vector $\hat{r} = (x, y, z)$ coincides with the position of a gate. $e > 0$ is the electron charge and ϵ the dielectric constant.

Self-consistent electrostatic-quantum problem

The first step in our calculation is a mean field (self-consistent Hartree) treatment of Eq.(8.1), in which we aim at solving together the following equations,

$$\Delta_{3D} U(\hat{r}) = -\frac{e\rho(\hat{r})}{\epsilon} + \frac{e\rho_0(\hat{r})}{\epsilon} \tag{8.3a}$$

$$\frac{-\hbar^2}{2m^\star}\Delta\Psi(\vec{r}) - eU(\vec{r})\Psi(\vec{r}) = E\Psi(\vec{r}) \tag{8.3b}$$

$$\rho(\vec{r}) = \sum_E f(E)|\Psi(E, \vec{r})|^2 \tag{8.3c}$$

where $U(\vec{r})$ is the restriction of $U(\hat{r})$ to the 2D plane of the electron gas, $\rho(\hat{r}) = \rho(\vec{r})\delta(z)$, Ψ the electronic wave function, f the Fermi function and the continuum sum in Eq.(8.3c) spans over all the eigenstates of the Schrödinger equation (8.3b). The density ρ_0 accounts for the layer of dopants present above the 2D gas; we use $U(\hat{r}) = V_{\mathrm{SG}}$ in the top gate and Von Neumann boundary conditions otherwise. We have explicitly verified that the finite width of the 2D gas along z does not

play a role in these calculations. Translational invariance along x implies that the Poisson equation can be solved in the 2D (y,z) plane while the wave-function is a plane wave, which can be separated into a transverse and a longitudinal component $\Psi(E, \vec{r}) = e^{ik_\alpha(E)x}\psi_\alpha(y)$. Performing an explicit integration along the longitudinal direction at zero temperature, we arrive at,

$$\Delta U(y,z) = -\frac{e\rho(y)}{\epsilon}\delta(z) + \frac{e\rho_0(y,z)}{\epsilon} \tag{8.4a}$$

$$-\frac{\hbar^2}{2m^\star}\frac{\partial^2}{\partial y^2}\psi_\alpha(y) - eU(y,0)\psi_\alpha(y) = E_\alpha\psi_\alpha(y) \tag{8.4b}$$

$$\rho(y) = \frac{2}{\pi}\sqrt{\frac{2m^\star}{\hbar^2}}\sum_\alpha |\psi_\alpha(y)|^2\sqrt{E_F - E_\alpha} \tag{8.4c}$$

where we have introduced the Fermi energy E_F. The factor 2 accounts for spin degeneracy. The Poisson equation for the potential $U(y,z)$ is solved on the (y,z) plane by using finite elements in a rectangular box with Von Neumann boundary conditions on the sides and fixed Dirichlet boundary conditions for the side-gate voltage V_SG. The size of the box has been chosen such that the results are free from finite size effects. An example of calculation of the Green's function $G(y,y') \equiv G(y, z=0; y', z'=0)$ is shown in Fig. 8.2 for illustration.

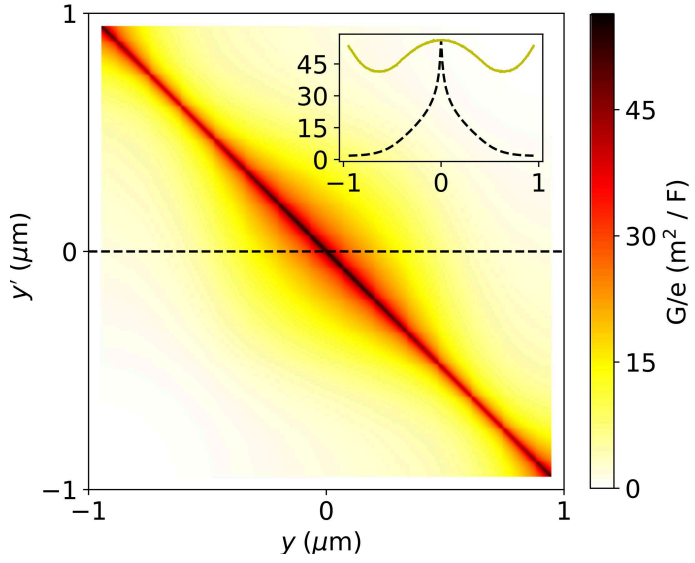

Figure 8.2: The Green's function G(y,y') of the Poisson equation calculated with the finite element method. The two thin regions in the diagonal of the figure at $y, y' = \pm 0.5$ coincide with the positions underneath the electrostatic gate. In the inset, the black dashed line represents a horizontal cut $G(y, y'=0)$ while the solid yellow line is the diagonal part of the matrix $G(y,y)$.

The Schrödinger equation is discretized using a simple finite difference scheme and solved using the Kwant package [2]. Solving the sequence of equations (8.4a), (8.4b) and (8.4c) for an input density ρ results to a new density ρ^{out}.

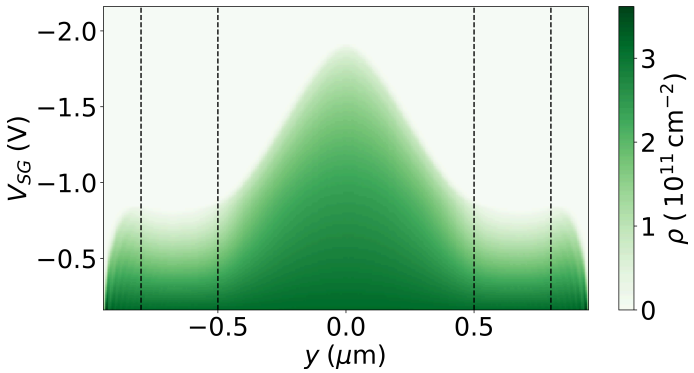

Figure 8.3: Colormap: density as a function of the transverse direction of the wire y (μm) and external gate voltage V_{SG} (V). The vertical black dashed lines show the positions of the two top gates.

The self consistency is reached when $\rho = \rho^{out}$ (see Fig. 8.4 for an example of convergence of our iterative procedure). The self-consistent solutions are obtained using a Newton-Raphson scheme [22]. *Note that this Newton-Raphson technique was used in the early stage of this thesis and proved cumbersome to make it converged, especially at low temperature. This convergence difficulties were one the motivation to develop our adiabatic approach. With the new method, these calculations would be easier to perform and orders of magnitude faster.* We use the following parameters: effective mass $m^\star = 0.067 m_e$, dielectric constant $\epsilon = 12\epsilon_0$ and a fixed dopant density of $n_d = 3.16 \cdot 10^{11}$ cm^{-2}. Note that this density is higher than the bulk 2D density of the gas. We have checked that our results are in fact independent of this value since the actual electronic density is controlled by V_{SG}. However, using a lower dopant density prevents us from exploring the high density regime ($V_{\mathrm{SG}} > -1V$) where the quasi-1D wire is not defined anymore.

Figure 8.3 shows a color map of the electronic density as a function of the transverse direction of the wire y and V_{SG}. The critical values of the gate voltage where the wire forms ($V_{\mathrm{SG}} \sim -0.8V$, the gas is depleted beneath the gates) and the pinch-off ($V_{\mathrm{SG}} \sim -1.8V$, full depletion) can be clearly identified.

8.2 velocity calculations

To proceed, we follow Matveev and Glazman [66] (see also a simpler construction [89]) and construct the bosonized theory for the plasmon excitations of the quasi-1D wire. Bosonization theory predicts that the plasmons have a linear dispersion relation $\omega = v_P q$, where ω is the plasmon energy, v_P the plasmon velocity and q the plasmon wave vector. The values of v_P are obtained from an eigenvalue problem described below.

In the presence of N propagating channels, we introduce the $N \times N$ diagonal

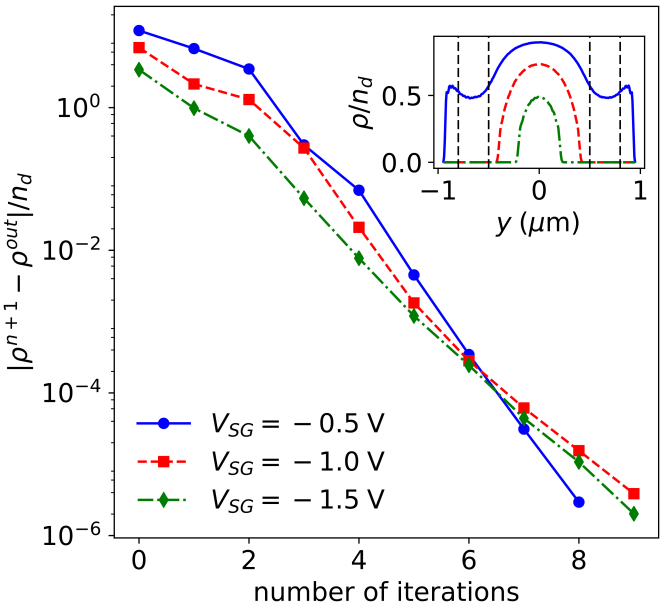

Figure 8.4: Convergence of the self-consistent algorithm for three different gate voltages (solid blue: -0.5 V, dashed red: -1.0 V and dash-dotted green: -1.5 V). At each iteration n we calculate from an input density ρ^n a new density ρ^{n+1}. Solving sequentially equation (8.4) we obtain ρ^{out} from which we can calculate the distance to the convergence and express it in terms of the dopant density $n_d = 3.16{\cdot}10^{11}$ cm^{-2}. The inset is the converged density for the 3 gate voltages in the same units.

velocity matrix $\tilde{V}$

$$\tilde{V}_{\alpha\beta} = \delta_{\alpha\beta} v_\alpha \tag{8.5}$$

where v_α is the non-interacting velocity of mode α. We also introduce the interaction matrix $\tilde{G}$ defined as,

$$\tilde{G}_{\alpha\beta} = \sqrt{v_\alpha v_\beta} \int \mathrm{d}y\mathrm{d}y' \, |\psi_\alpha(y)|^2 G(y,y') |\psi_\beta(y')|^2 \tag{8.6}$$

Figure 8.5 and 8.6a show examples of the different components of $\tilde{V}$ and $\tilde{G}$ for different values of the gate voltage. Once these objects have been defined, the plasmon velocities v_P can be obtained in a straightforward manner by diagonalizing the following matrix,

$$\left(\tilde{V}^2 + \frac{2}{h}\tilde{G}\right)\tilde{n} = v_P^2 \tilde{n} \tag{8.7}$$

where $\tilde{n}$ is a N-sized vector. Typically Eq.(8.7) has one large eigenvalue and $N-1$ small ones due to the low effective rank of the $\tilde{G}$ matrix (see Fig. 8.5). The plasmon velocity v_P is the chief outcome of this calculation and is shown in Fig. 8.6b.

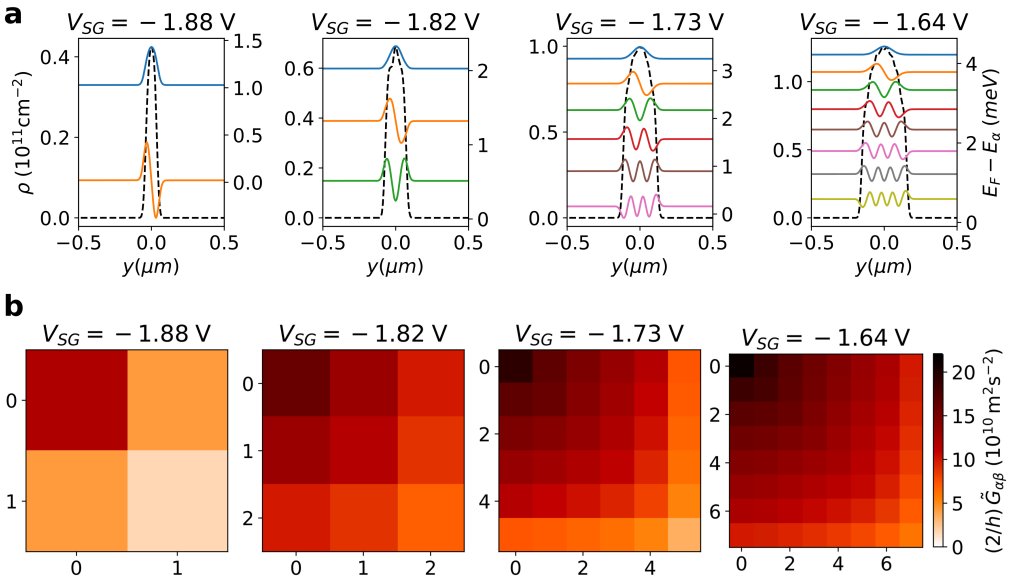

Figure 8.5: **a**, Density and wave functions for four different channel gate voltages (-1.88, -1.82, -1.73 and -1.64 V). In each plot the black dashed curve represents the self-consistent density ρ in cm^{-2} (left y axis). Each colored line sketches the shape of the wave function (in arbitrary units) of one open mode ψ_α, centered around its kinetic energy $E_F - E_\alpha$ (right y axis). **b**, Green function matrix $\tilde{G}$ from which we calculate the renormalized velocities, Eq. (8.7).

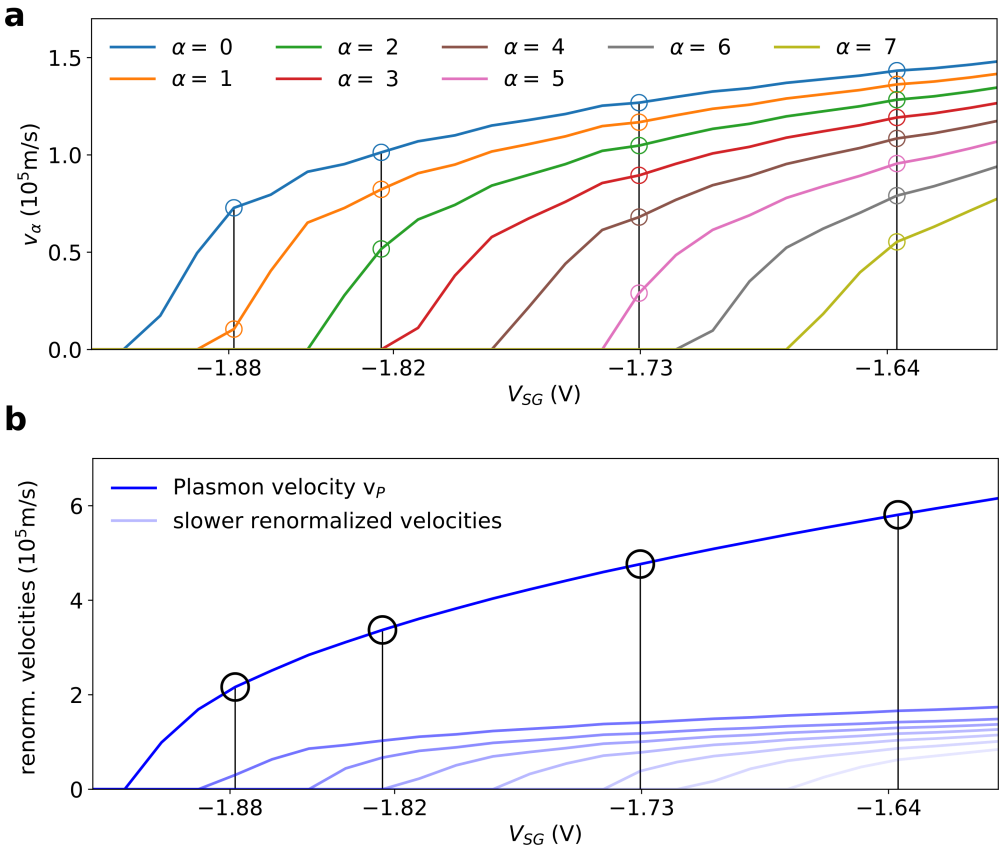

Figure 8.6: **a**, Non-interacting velocities v_α for the open modes as a function of gate voltage V_{SG}. The four gate voltages (-1.88, -1.82, -1.73 and -1.64 V) are marked with black vertical lines and the velocities of the corresponding open modes are marked with circles. **b**, Renormalized velocities calculated from Eq. 8.7 for each gate voltage V_{SG}. One velocity, indicated by the solid blue line, is considerably higher than the others. This fast collective mode, propagating with velocity v_{P}, corresponds to the plasmon mode shown in Fig. 6.5 (b)

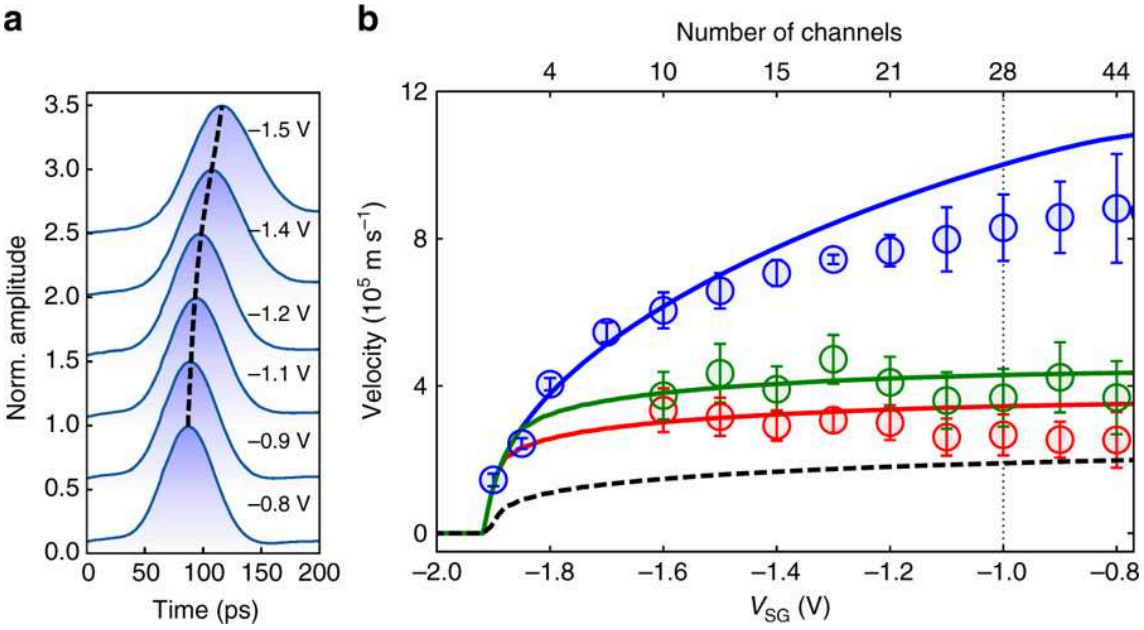

Figure 8.7: (a) reconstruction of the pulses in time for different gate voltages. (b) Plasmon velocities as a function of the gate confinement. The circles are the experimental measurements with their error bars, the solid lines are the results from our parameter free theory calculations. In blue the QPC_0 is opened, in red and green the QPC_0 is respectively at the first and second plateau. The dashed black lines shows the Fermi velocity calculated from the simulations.

9

Conclusion

The main result of this thesis was the development of a new algorithm to solve the self-consistent quantum-electrostatic problem. This made an important step in the direction of precision modeling for quantum nanoelectronics. This algorithm uses a new physics based approach: one starts by creating a simplified problem that can be solved exactly then one iteratively modifies the problem until convergence is reached. This approach allows to sequentially resolve the different energy scales, starting from the eV to the meV and beyond. Moreover and perhaps the most important point, since a problem is solved exactly at each iteration step, this method is intrinsically convergent, even when the density of state is a highly non-linear function of the energy. This gives our method essential qualities for an efficient simulation algorithm: it is **general**, **precise** and **robust**.

Using a prototyped implementation of the algorithm, we studied the integer quantum hall effect in a quasi one-dimensional wire. On top of it being a very hard test case for the convergence of the algorithm, this yields interesting physical results. After reproducing the Thomas-Fermi calculations of Chklovskii, Shklovskii and Glazman's (CSG) seminal paper [8], we produced - to our knowledge - the first fully self-consistent calculations of a quasi one-dimensional wire in the integer quantum Hall effect regime. Thanks to the robustness of our algorithm we were able to easily modify the parameters (gate voltage, magnetic field, temperature) and study their influence. We where able to resolve the apparent contradiction between the limits of zero and high magnetic field. On the one hand, at zero magnetic field, well defined Landauer-Büttiker (LB) like propagating channels are expected. On the other hand, deep in the quantum Hall effect regime, the density is characterized by alternating compressible and incompressible stripes and the current is carried by edge states. We found an hybrid phase that has both well defined LB-like edge states but also whose bulk density of state is pinned to the Fermi energy like in the CSG prediction.

The other novelty of this thesis was the calculation of the renormalized velocity of surface plasmons in 2DEG wires. We developed a technique that allows us to connect the Luttinger liquids to the microscopic problem, the later being obtained from the self-consistent calculations. We simulated the experimental setup of the measures by the group of C. Bäurle in Grenoble [6]. Using our technique, we calculated the plasmon velocities as a function of the confining gate potential. Very good agreement was found with the experimental results, without any adjustable parameter.

Future Perspectives

There is a strong need in the mesoscopic physics community for simple and efficient software solutions for solving the quantum-electrostatics problem. We believe that the new algorithm presented in this thesis could represent a great improvement in this respect.

In term of software development, the next step will be to make our code available to the community. We already implemented a mixed Poisson solver (including a simple geometry engine) as well as prototypes for the integration of the density of state and the self consistent solver. Making the transfer between these early stage implementations and a full autonomous library would greatly increase the impact of this work. It would mean going from a code that can only be used by trained specialists in quantum-electrostatics to a simple tool usable by all theorists that want to - for example - test an experiment proposal.

Finding relevant physical case for the application of this algorithm is not difficult. To pursue the work done in this thesis, it could be interesting to calculate the renormalized velocity of the edge magneto-plasmons in the quantum hall regime using an extension of our Boltzmann theory. Experiments are currently being done in this respect and comparison with the simulation should be possible. Another interesting case could be to study other material. Indeed the work in this thesis was limited to GaAs/AlGaAs 2DEG but one could do the same simulations in graphene or topological materials instead.

As we have proven to able to connect the microscopic world to the experimental observables, the next step is to systematically study an experimental system: a quantum point contact. The group of C. Bauerle is currently fabricating a hundred samples, with varying geometry. They will all be measured and systematically compared to predictions made with our algorithm. Once all the predictions match the experiment, we will have identified the relevant simulation parameters. We will then be able to use the simulation to optimize the design of any QPC. This would provide an interesting first real life example of precise modeling and benefit directly the experimentalist community.

Part III

Appendix

A

Calculation of the Lindhart function

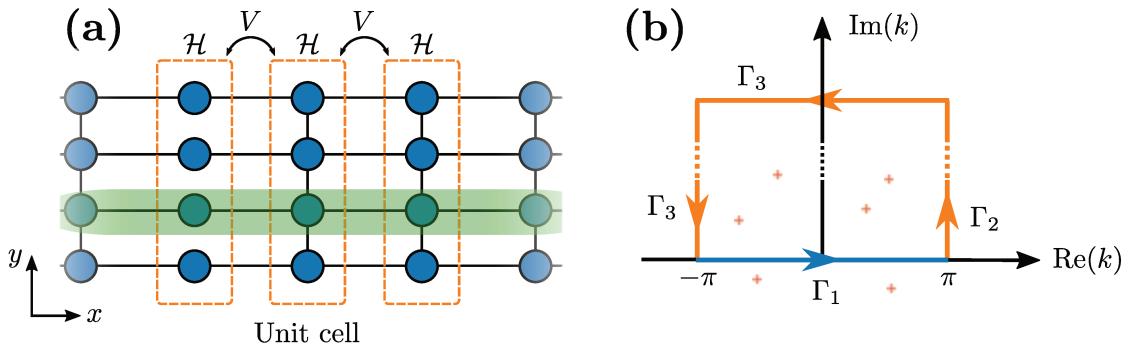

Figure A.1: (a) Schema of the quasi one-dimensional lead. It is made by infinite repetitions of a unit cell with Hamiltonian $\mathcal{H}$ coupled by hopping matrices V. The green zone corresponds to the region affected by a change of potential on one site $U \to U + \delta U_j$. (b) Complex contour for the integration of the product of Green's function. The poles p are represented with red crosses. The integral over the whole contour $\Gamma_0 \oplus \Gamma_1 \oplus \Gamma_2 \oplus \Gamma_3$ is equal to the sum over the poles in the contour of the corresponding residues

In this appendix we will show how the Lindhart function of section 1.2 can be calculated for a quasi one-dimensional system. The technique that we use is similar to the technique described in reference [90]. As this resolution is not a central part of this thesis, we will limit ourselves to giving the procedure and the main results. We suppose an infinite lead, invariant by translation along the y-axis. This system has been discretized so it can be seen as the repetition of unit cells of Hamiltonian $\mathcal{H}$ coupled by hopping matrices V or $V^\dagger$ (see Fig. A.1 (a)). The full Hamiltonian H

of the system can thus be written as blocks

$$H = \begin{bmatrix} \ddots & \ddots & \ddots & & & \\ & V^\dagger & \mathcal{H} & V & & \\ & & V^\dagger & \mathcal{H} & V & \\ & & & \ddots & \ddots & \ddots \end{bmatrix} \tag{A.1}$$

Let us recall that we want to calculate the derivative of the density at position i on the x-axis with respect to the potential U_j:

$$\frac{\partial n_i}{\partial U_j} = -\frac{1}{\pi} \int \mathrm{d}E \ \mathrm{Im} \left(\frac{\partial g_{ii}}{\partial V_j} \right) f(E) \tag{A.2}$$

where $(E - H)g = \mathbb{I}$. It is important to stress that the Green's function g here is the Green's function of the infinite quasi one-dimensional quantum system (or lead), let us call it g^{lead}. In a more explicit form, the local Green's function reads $g^{lead}_{ij;ij}$, where the i index spans the finite x-direction and the j index spans the y-direction. Since our system is supposed invariant along the y-direction, all j points are equivalents and one can choose $j = 0$. However, the change of potential that we want to impose on our system to calculate its derivative is on all sites of the y-direction (see Fig. A.1 (a)). As a consequence, we need to look at the Bloch picture.

A.1 Bloch picture and Dyson equation

The lead Green's function can be expressed as a function of the Green's function of the Bloch Hamiltonian $g^{1d}_{ii}(k)$ (which is defined on the x axis only):

$$g^{lead}_{i0,i0} = \int_{-\pi}^{\pi} \mathrm{d}k \ g^{1d}_{ii}(k) \tag{A.3}$$

This (retarded) Green's function has the following expression

$$g^{1d}(k) = \lim_{\eta \to 0} (E - \mathcal{H}(k) + i\eta) \tag{A.4}$$

where $\mathcal{H}$ is the Bloch Hamiltonian $\mathcal{H}(k) = (\mathcal{H} + V^\dagger e^{ik} + V e^{-ik})$. The cell Hamiltonian $\mathcal{H}$ can be separated into its free particle part $\mathcal{H}_0$ and its potential part U and we can explicitly write $\mathcal{H}(U) = \mathcal{H}_0 + U$, and for the green's function $g^{1D}_{ii}(U)$. We can calculate the new Green's function under a change of potential ϵ at site j through a Dyson equation:

$$g^{1D}_{ii}(U + \epsilon_j) = g^{1D}_{ii}(U) + \epsilon_j g^{1D}_{ij}(U) g^{1D}_{ji}(U) \tag{A.5}$$

where we supposed that there is only one degree of freedom per site, i.e. $g_{ij}^{1D}(U)$ is a scalar (otherwise one needs to take the trace of the matrix product). This allows to calculate the derivative (dropping the U dependency for readability):

$$\frac{\partial g_{ii}^{1D}(\epsilon_j)}{\partial U_j} \equiv \lim_{\epsilon_j \to 0} \frac{g_{ii}^{1D}(\epsilon_j) - g_{ii}^{1D}}{\epsilon_j} = g_{ij}^{1D} g_{ji}^{1D} \tag{A.6}$$

In order to perform the integral over k, one introduces a rectangular complex contour Γ (see Fig. A.1 (b)). Let us explicit the four intervals of this contour. The integral over Γ_1 spans the real axis between $-\pi$ and π. It corresponds to the integral that we want to calculate:

$$\frac{\partial g_{i0,i0}^{lead}(\epsilon_j)}{\partial U_j} = \int_{-\pi}^{\pi} \frac{\mathrm{d}k}{2\pi}\, g_{ij}^{1D}(k) g_{ji}^{1D}(k) \tag{A.7}$$

One can see that the integral over Γ_2 and Γ_4 respectively spanning $[\pi, \pi + iR]$ and $[-\pi + iR, -\pi]$ compensate each other because of the 2π periodicity of the Green's function. The final segment Γ_3 spans $[\pi + iR, -\pi + iR]$. In the case where the matrix V is invertible, the integral vanishes as R goes to ∞ due to the complex exponentials in the Bloch Hamiltonian. If V is not invertible, the calculation is more complicated and will be treated in the next section. We call this last integral I_3 so that the derivative of the lead Green's function can be written:

$$\frac{\partial g_{i0,i0}^{lead}}{\partial U_j} = -I_3 + \frac{2i\pi}{2\pi} \sum_{p \in \Gamma} \mathrm{Res}\left(g_{ij}^{1D} g_{ji}^{1D}(k)\right)\Big|_{k=p} \tag{A.8}$$

where the sum runs over all the poles p of the integrand inside the Γ contour. The two following sections will be dedicated to the calculation of the I_3 integral and the calculation of the residues. As we already mentioned, this calculation is done in great details in reference [90], where they calculate the integral of one Green's function. Our problem is very similar the only difference being that we need to integrate the product of two Green's function. For practicality and readability, in following sections we drop the explicit g^{1D} notations and just use g instead.

A.2 Calculation of the residues

In order to calculate the residues, we aim to calculate the Laurent series of the Green's functions around its poles: $g(\delta k) = g^{(-1)}\frac{1}{\delta k} + g^{(0)} + o(\delta k)$. The residues are the terms of order -1 of the Laurent expansion of the integrand:

$$\mathrm{Res}\left(g_{ij} g_{ji}(k)\right)\Big|_{k=p} = g_{ij}^{(-1)} g_{ji}^{(0)} + g_{ij}^{(0)} g_{ji}^{(-1)} \tag{A.9}$$

We introduce P the projector to $\mathrm{Ker}(E - \mathcal{H}(p))$ and its complementary $Q \equiv \mathbb{I} - P$. We also introduce the two first derivatives of the Hamiltonian: $\mathcal{H}_1(k) \equiv \partial_k \mathcal{H}(k)$ and

$\mathcal{H}_2(k) \equiv \partial_k^2 \mathcal{H}(k)$. Projecting the Laurent series on the kernel and image subspaces leads to the definition of $\bar{g}_0$ and $\bar{g}_0$

$$g^{(-1)} \equiv P\bar{g}_0 \qquad\qquad P\bar{g}_1 + Q\bar{g}_0 \tag{A.10}$$

After some algebra, one can prove the following expressions for each pole p, from which the residues can be calculated

$$\bar{g}_0 = ((E - \mathcal{H}(p)) - \mathcal{H}_1(p)P)^{-1} \tag{A.11}$$
$$\bar{g}_1 = \bar{g}_0 \left(\mathcal{H}_1(p)Q + \mathcal{H}_2(p)P\right) \bar{g}_0 \tag{A.12}$$

A.3 Calculation of the upper integral of the contour

Let us recall the definition of I_3 with an explicit form for the green's function:

$$I_3 = \lim_{R\to\infty} \int_{\pi+iR}^{-\pi+iR} \frac{\mathrm{d}k}{2\pi} \left(E - \mathcal{H}(k)\right)^{-1}_{ij} \left(E - \mathcal{H}(k)\right)^{-1}_{ji} \tag{A.13}$$

As we mentioned, this integral vanishes if V is full rank. If V is not full rank, we introduce P' and Q' respectively projector on the kernel and on the image of V. It can be proven that

$$\lim_{k\to i\infty} \frac{1}{E - \mathcal{H}(k)} = P' \frac{1}{(E - \mathcal{H})P' + V} \tag{A.14}$$

where $\mathcal{H}$ is the cell Hamiltonian and should not be confused with the Bloch Hamiltonian $\mathcal{H}(k)$. From here, it is straightforward to solve I_3:

$$I_3 = \left(P' \frac{1}{(E - \mathcal{H})P' + V}\right)_{ij} \left(P' \frac{1}{(E - \mathcal{H})P' + V}\right)_{ji} \tag{A.15}$$

B

On the ionization of dopants

Lets explicit our clame about the dopants in 2.1. We suppose a simple model for the dopants. On each site the dopants can be either ionized or not ionized depending on the local potential, and ionized dopant density follows:

$$n^{ion}(E) = \frac{n^d}{1 + ge^{\frac{E_\Delta - E}{k_B T}}} \tag{B.1}$$

where $n^{ion}(E)$ is the energy dependent number of ionized dopant, E is the energy, n^d is the constant dopant density, g the degeneracy of the dopant ionized level, E_Δ the activation energy of the dopants, k_B the Boltzmann constant and T the temperature. The bulk Poisson equation reads $n^{ion} = n^0 + (C/e)U$ and the electrochemical potential is externally fixed by V_g and $V_g = U + E/e$.

Solving the bulk self-consistent problem is finding the intersection between the Poisson equation and the dopant density equation (see Fig.B.1). At low temperature, the dopant distribution is as step function and there are three classes of solutions. Either no dopants are ionized, $n^{ion} = 0$ and the self-consistent potential $U > E_\Delta/e - V_g$. Or all the dopants are ionized, $n^{ion} = n^d$ and $U < E_\Delta/e - V_g$. Or some dopants are ionized, $0 < n^{ion} < n^d$ and the self-consistent potential is fixed at the activation energy. The case $n^{ion} = 0$ is equivalent to the case where there are no dopant at all and is not interesting. If not all dopants are ionized, it means that the potential is pined to the activation energy, so there is a range of gate voltage for which the dopant screen perfectly the gate. The dopants then behave as an effective gate. If this situation was found experimentally, no field effect due to the gate would be detected since the effective gate will entirely screen the real gate. As field effect is observed experimentally, one concludes that this is not the relevant situation. The only remaining solution is that the ionized density of dopant is constant and doesn't screen the gate, which is more compatible with the experiments. This justifies our choice of taking a constant dopant density n^d and consider that all the dopants

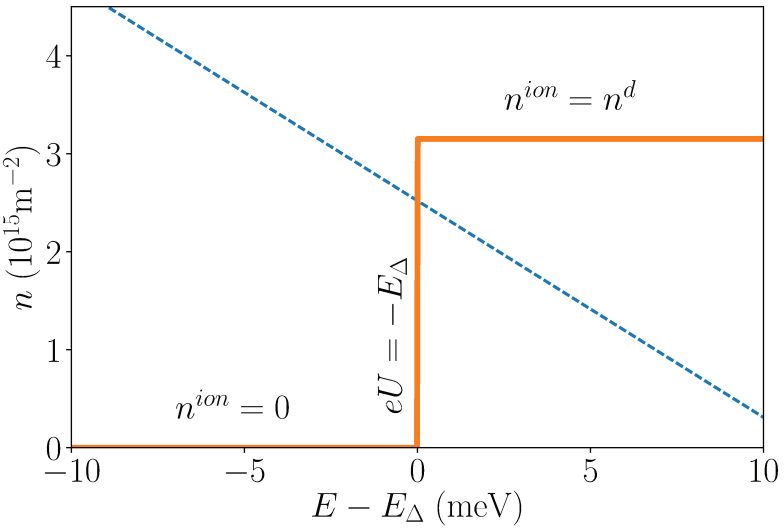

Figure B.1: self-consistent solution for the dopant density at $T = 0K$. In orange the dopant density as a function of the energy E. In blue the Poisson equation as a function of the energy. Three types of solution are visible: $n^{ion} = 0$ (lower left), $n^{ion} = n^d$ (upper right) and $eU = -E_\Delta$ (center).

are ionized. It has been remarked that the quantity of dopant is much larger than the quantity of charges in the 2DEG, i.e. $\sum n^d \gg \sum n$. If all dopants are ionized, there must be charges that are trapped at the surface of the sample, which we could observe in simulations.

C

Integrating the LDOS

A critical point in our algorithm is the integrated local density of state ILDOS. Indeed it is the only place where the quantum system appears in the solver. It is thus of particular importance to be able to determine it in the most precise way possible. It is also often the most time consuming computation to be done. We exclude here the case where an approximated analytical ILDOS can be calculated (Thomas Fermi approximation, wave function factorization) and focus on the cases where the local density of state needs to be numerically integrated. We recall

$$\rho_i(\mu) = \sum_\alpha \int \mathrm{dE}\ \rho_\alpha(\mathrm{E,i})\,\mathrm{f}(\mathrm{E},\mu) \tag{C.1}$$

where $\rho_\alpha(E,i) = |\psi_\alpha(E,i)|^2$ is the local density of state of the mode α at site i energy E. We first introduce the concept of numerical integration and then present some algorithms that we use to calculate ILDOS.

C.1 Generalities on interpolation

Direct integration and interpolation

Calculating numerically the integral of a function is in itself a whole branch of numerical computation, so this short introduction doesn't pretend to be general nor exhaustive, but rather, expose the tools that we need to explain our techniques. Suppose that one wants to calculate the following integral of a general function f between two real numbers a and b

$$I = \int_a^b f(x)\,\mathrm{d}x \tag{C.2}$$

To simplify, a and b are supposed to be finite. In the infinite case, one would usually use a change of variable to map the infinite interval to a finite one.

Gaussian quadratures

The usual way to compute such an integral is to use a Gaussian quadrature rule (GQR), that is to express this integral as a weighted sum of the value of the function evaluated at certain points called nodes:

$$I_0 = \int_{-1}^{1} f(x)\,\mathrm{d}x \approx \sum_{i=0}^{n} w_i f(x_i) \tag{C.3}$$

where w_i are the weights and $-1 \leq x_i \leq 1$ the nodes. The integration interval has been changed for reasons that will become clear later, but one can get back to the original $[a, b]$ interval through a change of variable $x_i \to (b-a)/2x_i + (a+b)/2$ and by multiplying by the relative width of the interval $(b-a)/2$. By definition a GQR with n nodes is exact for the integration of a polynomial of degree $2n-1$. The well known rectangle, trapezoidal and Simpson rule are respectively GQR with 1 node ($x_i = 0, w_i = 2$), 2 nodes ($\{x_i\} = \{-1, 1\}, \{w_i\} = \{1, 1\}$), and 3 nodes $\{x_i\} = \{-1, 0, 1\}, \{w_i\} = \{1/3, 4/3, 1/3\}$, and can integrate exactly polynomial functions of order 1, 2 and 3. For more complicated function to integrate, more advanced GQR are used. One can see here that the advantage of defining the weight and nodes on $[-1, 1]$ is that the weight and nodes are independent of the function to integrate and the interval, so they can be known in advance.

The integration error is evaluated by comparing the integration with two different GQR. If the error is not satisfactory, one can obviously cut the integration interval into two and integrate separately the two new intervals, and iterate this loop until convergence. It is also possible to change the number of nodes of the GQR instead of cutting the interval. These methods that adapt the number of nodes and/or cut the interval are called adaptive methods.

The nodes are chosen in order to optimize the interpolation on the interval $[-1, 1]$. The idea being to prevent missing oscillations of the integrand, it is unadvised to use regularly spaced points, and one would rather have more density of points at the exterior of the interval. The method that we used works with the zeros of a Tchebyschev polynomial defined bellow

$$x_k^N = \cos\left(\pi \frac{k+1}{N+1}\right) \tag{C.4}$$

where N is the number of nodes and k counts the nodes $0 \leq k \leq N-1$. An other advantage is that the nodes at order N are included in the nodes at order $2N+1$, which makes refining the number of points more efficient, since N points don't need to be recalculated.

Interpolation and Legendre quadratures

One remaining question after introducing the GQR is how are the weights calculated? One solution is to consider an interpolation on a basis of functions ϕ_j of a the function to integrate. Lets suppose that f can be approximated by a weighted sum of n functions ϕ_j and weights a_j, and that the interpolation is exact on n points x_i where the function is known $f(x_i) \equiv y_i$

$$f(x) \approx \sum_j^n a_j \phi_j(x), \qquad f(x_i) \equiv y_i = \sum_j^n a_j \phi_j(x_i) \tag{C.5}$$

The $\phi_j(x_i)$ are matrix elements of a Vandermonde like matrix Φ ($[\Phi]_{ji} = \phi_j(x_i)$), that can be inverted. By replacing f by its decomposition and identifying the points x_i to the nodes of a GQR we get for the integral of f

$$\begin{aligned}\int_{-1}^{1} f(x)\,\mathrm{d}x &\approx \sum_i w_i f(x_i) \\ &\approx \sum_i \left(\sum_j [\Phi^{-1}]_{ij} \int_{-1}^{1} \phi_j(x)\,\mathrm{d}x \right) f(x_i)\end{aligned}$$

from which one gets an implicit definition of the weights w_i.

In the particular case of Legendre polynomials (LP) for the interpolation basis, this can be simplified a lot. Lets first recall few properties of the LP. LP are orthogonal polynomial functions defined by recurrence

$$P_n(x) = \frac{1}{2^n} \sum_{k=0}^{n} \binom{n}{k}^2 (x-1)^{n-k}(x+1)^k, \tag{C.6}$$

$$\int_{-1}^{1} P_m(x) P_n(x) \mathrm{d}x = \frac{2}{2n+1} \delta_{nm} \tag{C.7}$$

from this properties, one easily gets that $P_0 = 1$ and that the integral in the definition can be simplified $\int_{-1}^{1} \mathrm{d}x P_j(x) = 2\delta_{j0}$. Finaly the weights are simply

$$w_i = 2 \left[P^{-1} \right]_{i0} \tag{C.8}$$

where P is the Vandermonde like matrix of LP ($[P]_{ji} = P_j(x_i)$). If the nodes are known in advance, this matrix and its inverse can be pre-calculated to decrease the computation time.

Let us go back to the initial problem of calculating ILDOS ($\rho(\mu) = \int_{E_0}^{E_{max}} \rho(E) f(E-\mu) \mathrm{d}E$), i.e. the whole primitive of the LDOS. In order to get good performances, we want to pre-calculate this functions, which means we need to construct an interpolation of it, which means evaluate this function on a number of chosen points. Since we have to calculate at least one integral of the LDOS, we can use the points where

the function is evaluated to compute the integral. Indeed, for each subintervals, these points are supposed to be sufficient to compute the integral. Thus by calculating the integral for one interval $[E_0, E_{max}]$ and keeping the information on the coefficients a_j on all subintervals, one gets the integral on all possible interval $[a, b]$ ($E_0 \leq a \leq b \leq E_{max}$). As a summary, we use an integration routine on one interval (the largest), to get the integral on any subintervals, with an optimized choice of point of interpolation.

C.2 Integration in the k space

The previous method for integration (and interpolation) is sufficient when the function to integrate (the LDOS) is smooth enough. With a smart integrator, such as the one we used ([91]), and with a smart choice for the integration interval, one can even calculate integrable divergences. However, it fails spectacularly when the LDOS exhibits (quasi-) Dirac peaks as it is the case in the QHE regime. These peaks are so thin that even adaptive methods can not detect it. We present here our solution for integrating these kind of density of state. Please note that we only implemented them for quantum system with translation invariance (leads), with defined modes $\psi_\alpha(E)$ and dispersion relation $E_\alpha(k)$. In some cases they can be generalized to system with scattering regions and leads but this is beyond the scope of this thesis.

The idea here is to rotate the integration from E to k using the dispersion relation for the change of variable. Indeed the previously discussed divergences occur at the opening of a mode (see Fig. C.1). There is no such band opening if we look at each band individually as a function k, i.e. the bands are smooth for $-\pi \leq k \leq \pi$.

We can rewrite equation C.1:

$$K_i(\mu) = \sum_\alpha \int_{-\pi}^{\pi} \mathrm{dk}\, \frac{\mathrm{dE}}{\mathrm{dk}} \rho_\alpha(\mathrm{E}_\alpha(\mathrm{k}), \mathrm{i})\, \mathrm{f_T}(\mathrm{E}_\alpha(\mathrm{k}), \mu) \tag{C.9}$$

Using the fact that $|\psi_{\alpha k}(i)|^2 = \frac{\mathrm{dE}}{\mathrm{dk}} \rho_\alpha(E_\alpha(k), i)$ is the wave function normalized by velocity, (as directly outputted by Kwant)

$$K_i(\mu) = \sum_\alpha \int_{-\pi}^{\pi} \mathrm{dk}\, |\psi_{\alpha\mathrm{k}}(\mathrm{i})|^2\, \mathrm{f_T}(\mathrm{E}_\alpha(\mathrm{k}), \mu) \tag{C.10}$$

Since the wave functions are calculated via Kwant, what remains is the integration over k

Simple integration

The idea behind this method is to realize that the chemical potential μ only appears in the Fermi function. In principle, this means that one should be able to get as

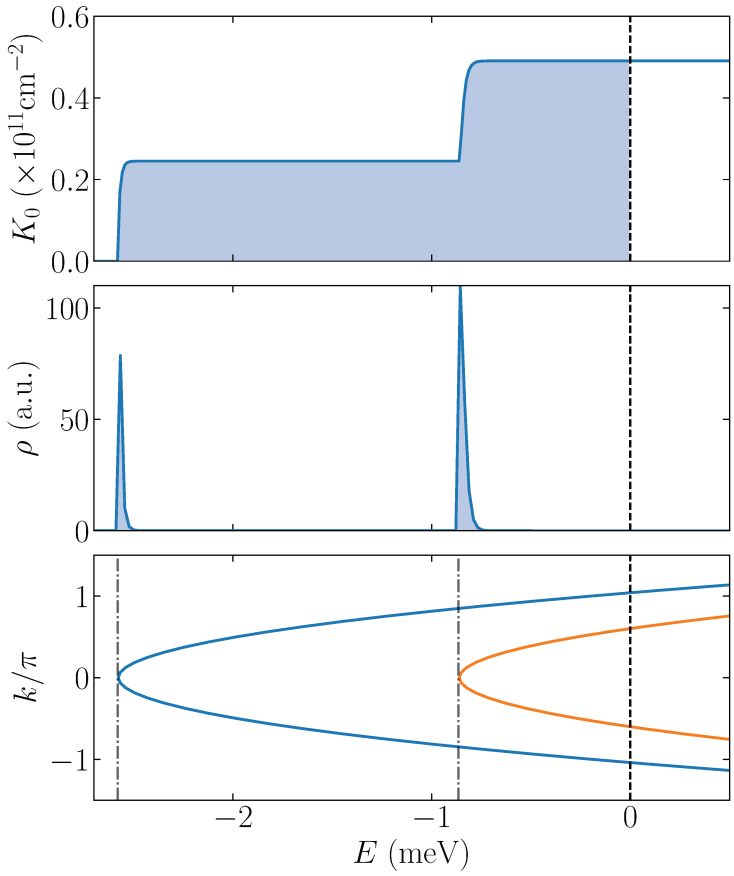

Figure C.1: (top) Integrated local density of state $\rho(\mu)$, (center) local density of state $\rho(E)$ and (bottom) dispersion relation as a function of the energy E for a toy potential and magnetic field $B = 1T$. Bands open in the dispersion relation at $E \sim -0.8$meV and $E \sim -2.6$meV. To these openings correspond divergences of the density of state. These divergences are themselves translated into jumps of the integrated density of state.

many value of μ as we want for the cost of one integration. The drawback being that point of integration in k have to be decided in advance. The algorithm goes as follow:

- Prepare a list of energies for the interpolation. We calculate the bands of the system for a regular spacing in k. For each band, the corresponding energies are calculated and added to a list $\{E_\mu\}$. This ensures that more interpolation points will be present near a band opening, yielding a smoother interpolant as shown in Fig.C.2.

- Get the integration points in k. The integration interval $[-\pi, \pi]$ is divided into sub-intervals on which Tchebyschev nodes $\{k_i\}$ and weights $\{w_i\}$ are calculated.

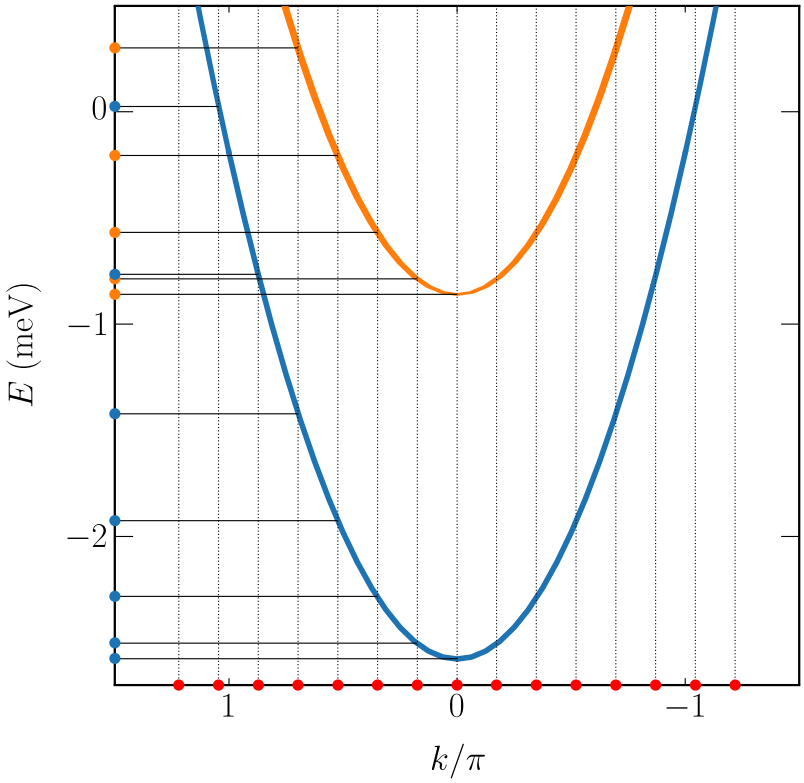

Figure C.2: Preparing the list of energy points. We first generate regularly space points in k (red). Then we calculate the corresponding energies E for each modes (blue and orange). By construction there are more points around the band openings

- For each k in k_i calculate the wave function and energies. The wave functions $\{\psi_k^n\}$ and energies $\{\epsilon_k^n\}$ of each modes n are calculated by Kwant.

- Then simply sum for each k the square of the wave function times the Fermi function for all energies in $\{E_\mu\}$ and keep its value in a table

$$\mathrm{Int}_\mu = \sum_{k_i} \sum_n \frac{w_i}{\pi} \left(f(\epsilon_i^n - E_\mu) \times |\psi_i^n|^2 \right) \tag{C.11}$$

  where the spatial dependency of the wave function is hidden.

- Finally construct an interpolant in energy at each point in space

In practice we do vectorial calculations: for each k we compute the table $f_{\mu,n} = f(\epsilon_n - E\mu)$ and do the matrix vector product $f \cdot |\psi_k|^2$.

The problem of this method is that we need to give the k in advance an can not use adaptive integration (keeping all the information needed would take too much memory).

Integration of interpolated function

The other idea is to interpolate the wave functions and dispersion relations and exactly integrate their interpolations. We still need to choose the $\{k_i\}$ and $\{E_\mu\}$. We can then construct on each subinterval the wave function and eigenenergie interpolations on power of k

$$|\psi^n(k)|^2 = \sum_i \alpha_i^n (k)^i, \qquad \epsilon^n(k) = \sum_j \beta_j^n (k)^j \tag{C.12}$$

By replacing these into the integral C.10 we obtain on each subinterval

$$\text{Int}[\mu, :] = \sum_i \sum_n \alpha_i^n \int_{-\pi}^{\pi} \mathrm{d}E\ (k)^i\ f\left(\sum_j \beta_j^n (k)^j - E_\mu\right) \tag{C.13}$$

Using fast polynomial evaluation (horner method) this was the method giving the best result. One problem that has been voluntarily left out is the fact that one needs to be able to follow a band in $[-\pi, \pi]$. This is not at all trivial when band crossing occur. To do so we used a tool for the band analysis developed by a post-doc in the lab that allows to do it.

D

More details on the IQHE

This appendix is made a supplementary informations to the chapter 4. The goal here is double. First, it can serve as a crash course on the integer quantum Hall effect without self-consistency as we start by establishing the relations used in the thesis. Second, we also explicit more precisely the construction of compressible and incompressible stripes from the article by Chklovskii, Shklovskii and Glazman [8].

D.1 Landau levels

We start by establishing the solution of the Schrödinger equation for a free particle in a 2D plane, under a perpendicular magnetic field, i.e. the Landau levels.

Particle in a constant magnetic field

Let us consider a particle of mass m, restricted to a 2d space and with wave function $\psi(x, y)$. Its equation of motion is governed by the following Hamiltonian $H = \mathbf{P}^2/2m$ where $\mathbf{P}$ is the 2d momentum operator. This particle is plunged into a constant magnetic field in the z direction $\mathbf{B} = B\hat{z}$, perpendicular to its plan of motion. The corresponding vector potential is A such that $\mathbf{B} = \nabla \times \mathbf{A}$. The effect of this potential can be incorporated into the previous Hamiltonian through minimal coupling:

$$H = \frac{(\mathbf{P} - e\mathbf{A})^2}{2m} \tag{D.1}$$

For practicality we choose to express the vector potential in the Landau gauge: $\mathbf{A} = xB\hat{y}$. The Hamiltonian can be rewritten:

$$H = \frac{P_x^2}{2m} + \frac{(\mathbf{P_y} - exB\hat{y})^2}{2m} \tag{D.2}$$

where the momentum operator has been separated into its components P_x and P_y. This form is explicitly invariant along y which motivates to develop the solution on plane waves $\psi(x,y) = \phi(x)e^{iky}$. Using the explicit form of the momentum operator $P_y = -i\hbar\nabla_y$, one obtains an effective 1D Hamiltonian, which can expressed as an harmonic oscillator:

$$\begin{aligned} H_k &= \frac{P_x^2}{2m} + \frac{(\hbar k - e\mathbf{A})^2}{2m} \\ &= \frac{P_x^2}{2m} + \frac{m}{2}\left(\frac{eB}{m}\right)^2 \left(x - \frac{\hbar}{eB}k\right) \\ &= \frac{P_x^2}{2m} + \frac{m}{2}\omega_c \left(x - kl_B^2\right) \end{aligned}$$

where $\omega_c = (eB)/m$ is the cyclotron frequency and $l_B = \sqrt{\hbar/(eB)}$ is the magnetic length. This is an harmonic oscillator of frequency ω_c and with center displaced by kl_B^2. Its spectrum and eigenvectors are well known to be:

$$E_n = \hbar\omega_c \left(n + \frac{1}{2}\right) \tag{D.3}$$

$$\phi(x) \propto \mathcal{H}(x - kl_B^2)\, e^{-\frac{(x-kl_B^2)^2}{2l_B^2}} \tag{D.4}$$

$$\tag{D.5}$$

This spectrum is constituted of flat bands called Landau levels (LLs), independent of k, separated by $\hbar\omega_c$. The corresponding wave functions are made of an hermitian polynomial times a gaussian centered on $x_0 = kl_B^2$ and width l_B. This introduces a formal mapping between position x and momentum k which give interesting properties to the LLs. We remark that the invariance along the direction x has been hidden by the choice of the gauge.

The LLs are highly degenerated. Let us consider a box of size $L_x \times L_y$. The confinement in x: $0 \leq x \leq L_x$ implies a confinement in k: $0 \leq |k| \leq L_x/l_B^2$. The total number of particle in the box is then $N = L_y \int_0^{L_x/l_B^2} \frac{\mathrm{d}k}{2\pi}$ which gives for the density of a LL:

$$n_{LL} = \frac{N}{L_x L_y} = \frac{1}{2\pi l_B^2} = \frac{B}{\varphi_0} \tag{D.6}$$

where $\phi_0 = h/e$ is the flux quantum.

Effect of a small confinement

We suppose now a confinement $V(x)$, varying slowly compared to l_B along x. At first order, the wave functions are not modified and the change in the energies can be calculated from perturbation theory: $\delta E_n = \int \mathrm{d}x \, \langle\psi_n| \, V(x) \, |\psi_n\rangle$. For a potential

$V(x)$ varying adiabatically, the change of energy is just the potential at the center of the gaussian x_0. $\delta E_n \sim V(x_0) = V(kl_B^2)$. We see that the dispersion relation has been made k dependent. But this dependency also corresponds to a space dependency: the bands are simply bended by the potential:

$$E_n = \hbar\omega_c \left(n + \frac{1}{2}\right) + V(x_0 = kl_B^2) \tag{D.7}$$

The effect of the potential can be seen on Fig. D.1(b) (which is a sketch of Fig. 4.1 (b)). By imposing a Fermi energy one opens modes and since the dispersion relation can be read in real space, we can seed that these modes are situated at the edge of the sample. Their drift velocity is given by their Fermi velocity $v_n \propto \partial E_n/\partial x$. One sees that the velocity is negative at the left of the sample and positive at the right: these are chiral edge states.

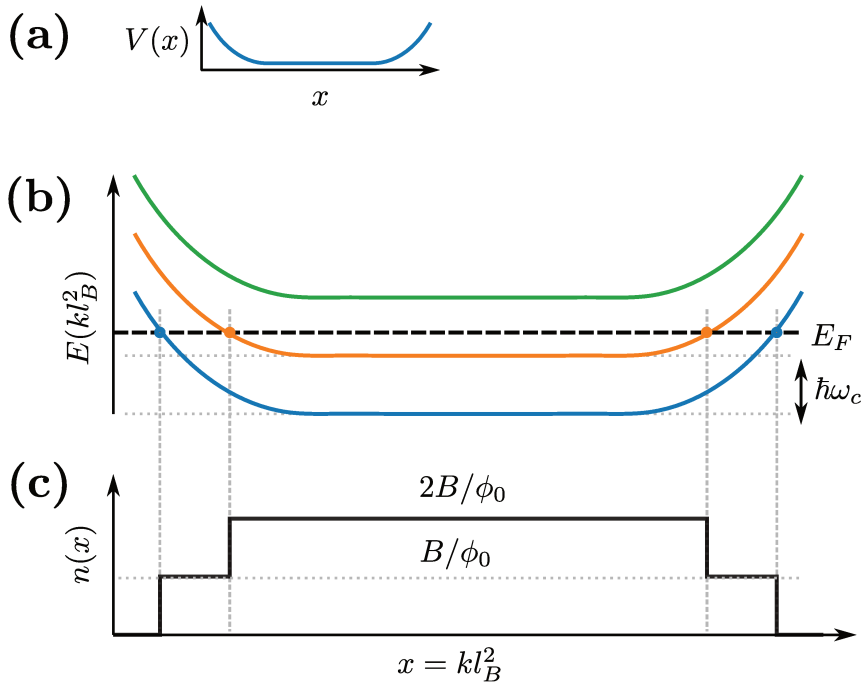

Figure D.1: (a) Adiabatic confinement $V(x)$. (b) Bending of the LLs dispersion relation (top) due to the confinement and corresponding density profile (bottom)

Longitudinal and hall resistance of the LLs

In order to observe the quantization of the hall conductance (or resistance), let us consider the hall bar shown in D.2. We injected one pair of chiral edge states in the bar. We define the current between leads from Landauer-Buttiker theory with ideal transmission (no backscattering). I_1 current in lead 1, I_{12} current in cable between lead 1 and 2. By definition the current in the cable between the lead 1 and 6 is $I_{61} = N_{\text{ch}}e^2/h(V_1 - V_6)$ where N_{ch} is the number of chiral channel (here $N_{ch} = 1$),

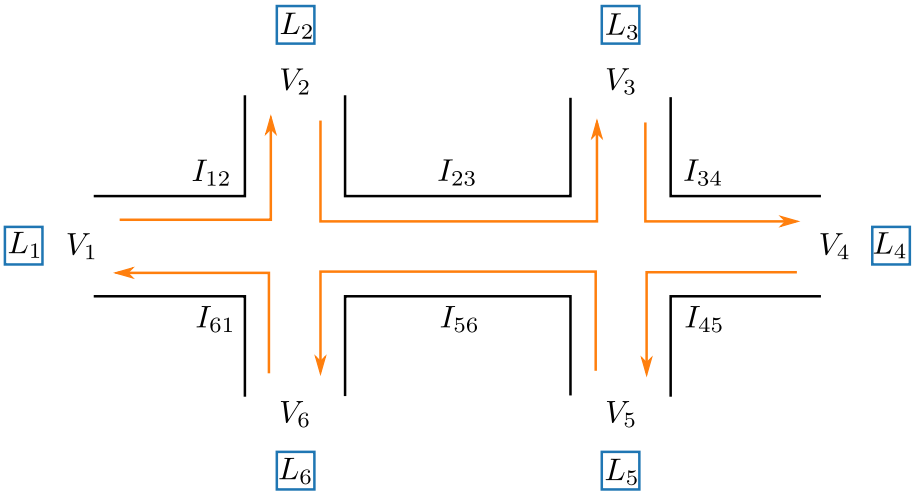

Figure D.2: Schema of a hall bar with 1 pair of chiral edge states. The potential V_a are the potential in the leads L_a, the I_{ab} is the current in the cable between lead L_a and lead L_b

and so on for all pairs of leads. In order to perform a measure, we impose that the input current in lead 1 is the same as the current in lead 4: $I_1 = I = -I_4$ and that the current is 0 in the other leads $I_1 = I_2 = I_4 = I_5 = 0$. This imposes a constant potential in the upper and lower branch $V_2 = V_3 = V_4$, $V_5 = V_6 = V_1$. From these definition one can calculate the hall resistance $R_H = (V_2 - V_6)/I = (V_3 - V_5)/I$ and the longitudinal resistance $R_L = (V_3 - V_2)/I = (V_5 - V_6)/I$. One finds

$$R_H = \frac{h}{e^2}\frac{1}{N_{\text{ch}}} \qquad R_L = 0 \tag{D.8}$$

The hall resistance is quantized and depends of the inverse of $N_{ch}e^2/h$, with N_{ch} an integer corresponding to the number of open channel (crossing of E_F in Fig. D.1 (b)). This is in perfect agreement with the experimental observations shown in D.3. At B corresponding to a channel opening, the LL is exactly at the Fermi energy, conduction can happen in the bulk through percolation of cyclotron orbits, which can explain the jumps observed in R_L).

D.2 Construction of compressible and incompressible stripes

The problem arrising from this definition of the LLs has already been discussed in chapter 4 and is clearly visible in Fig. D.1 (c) (namely, the density in the bulk is proportional to the field, which is not possible in reallity). In this part, we just aim to explicit the construction of the compressible stripes. This construction can be separated in 3 stages (Fig. D.4).

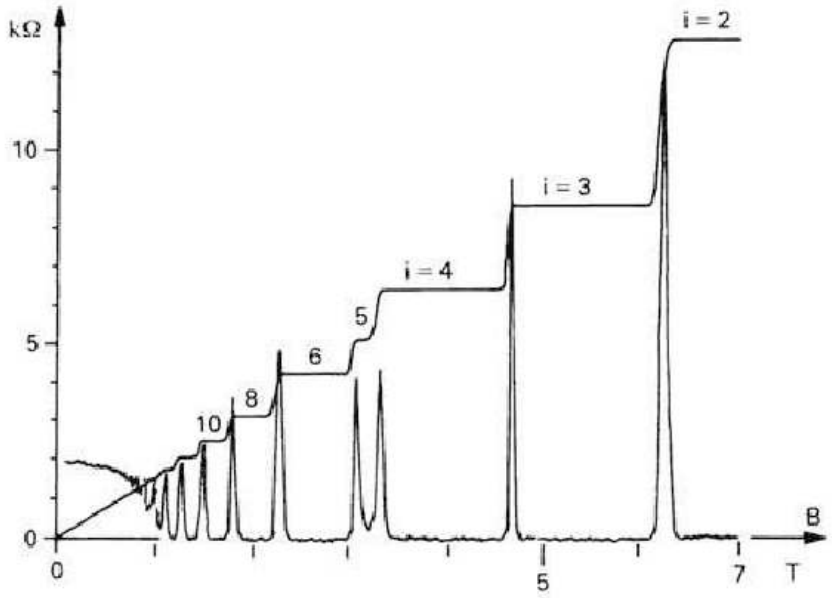

Figure D.3: Experimental observation of the quantized hall resistivity. from Practice and theory. NobelPrize.org. Nobel Media AB 2019. Wed. 10 Apr 2019. https://www.nobelprize.org/prizes/physics/1998/9580-practice-and-theory/

(a) Since the density should not be modified by the magnetic field, we start with a density at B=0. This density has a particular value in the bulk n_0, corresponding to a non-integer number of LL: $n_0 \sim 2.3 n_{LL} = 2.3B/\phi_0$. This means that in the bulk, two LLs should be fully opened (blue and orange in the figure) and the third one should sit exactly at the Fermi energy since it is not entirely filled (green). Going away from the bulk, the density should cross the $n(x) = 2n_{LL}$ and $n(x) = n_{LL}$, which corresponds to the closing of a LL (vertical dashed lines). Between these closing, the density varies so the LLs should be pinned to the Fermi energy.

(b) One then connects the flat parts of the LL with each other, level by level (blue, orange and green separatly).

(c) Finally one corrects the density: where there is no LL in at the Fermi energy (no available states), the density can not vary (light blue vertical spans). This creates plateaux. After connecting smoothly between these plateaux to the density at B=0, one obtains the final picture: Where the density varies, the LL are pinned to the Fermi energy (compressible stripes); and where the LL leave the Fermi energy, the density plateaus (incompressible stripes).

D.3 Estimation of the width of an incompressible plateau

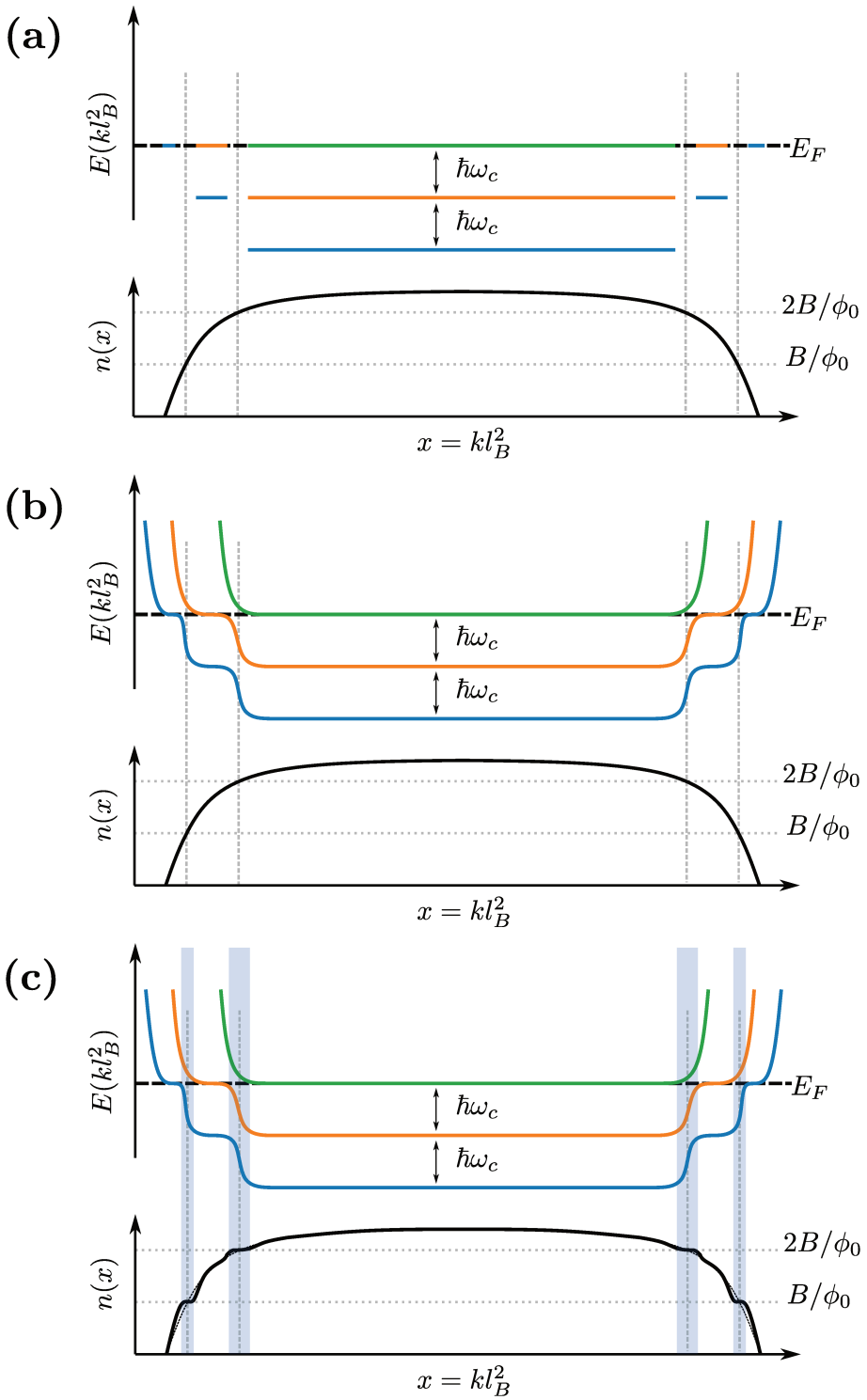

Figure D.4: Sketch of the construction of the CSG compressible and incompressible stripes. For each plot, the top is the dispersion relation (3 fist bands in blue, orange and green), and the bottom is the density.

We just ad here a schema to explicit the calculation of the width of an incompressible plateau presented in equation D.9 of the section 4.5. The situation is presented in Fig. D.5. In order to prevent back and forth between here and section 4.5, let us just rewritte the derivation.

The positions x_ν of the center of the incompressible stripes can be estimated from the electronic density calculated at zero field $n(x, B = 0)$ with very good approximation $n(x_\nu, B = 0) = \nu eB/h$ ($\nu = 1, 2, \dots$). The width δx_ν of these plateaus can also be estimated using a simple energetic argument. The creation of the incompressible stripe involves the creation of the small electric dipole of charge δq_ν with respect to the $B = 0$ density. On one hand, we have $\delta q_\nu \approx e\partial_x n(x_\nu, B = 0)\delta x_\nu$. On the other hand, electrostatic imposes $\delta q_\nu \approx c(\epsilon/\delta x_\nu)(\hbar\omega_c/e)$ where $c(\epsilon/d)$ is the effective capacitance of the problem and $(\hbar\omega_c/e)$ is the kinetic energy gained by creating the stripe, which compensates the corresponding electric energy ($\omega_c = eB/m^\star$ is the cyclotron frequency). We arrive at [8],

$$\delta x_\nu \approx \sqrt{\frac{c\epsilon\hbar B}{em^*\partial_x n(x_\nu, B = 0)}} \tag{D.9}$$

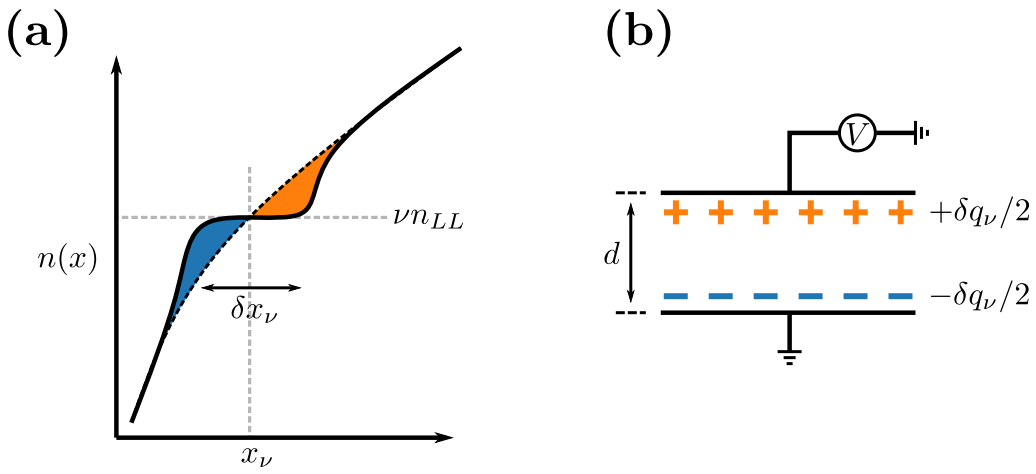

Figure D.5: Analytical estimation of the width of an incompressible plateau. (a) zoom on a density plateau. A dipole is created compared to the density at B=0 (thin dashed line) between an excess of negative charges comming from the first LL (blue) and a default of negative charges from the first LL. (b) Equivalent planar capacitor. Two plates with a potential difference $V = \hbar\omega_c/e$ are separated by a distance $d = \delta x_\nu$, creating a charge difference $e\delta q_\nu$.

Bibliography

[1] T. Jullien, P. Roulleau, B. Roche, A. Cavanna, Y. Jin, and D. C. Glattli, "Quantum tomography of an electron," *Nature*, vol. 514, p. 603, Oct. 2014.

[2] C. W. Groth, M. Wimmer, A. R. Akhmerov, and X. Waintal, "Kwant: a software package for quantum transport," *New Journal of Physics*, vol. 16, p. 063065, jun 2014.

[3] P. Armagnat, A. Lacerda, B. Rossignol, C. Groth, and X. Waintal, "The self-consistent quantum-electrostatic problem in strongly non-linear regime," *In preparation*, 2019.

[4] P. Armagnat and X. Waintal, "Reconciling edge states with compressible stripes in a ballistic mesoscopic conductor," *arXiv e-prints*, p. arXiv:1903.05028, Mar 2019.

[5] B. Rossignol, T. Kloss, P. Armagnat, and X. Waintal, "Toward flying qubit spectroscopy," *Phys. Rev. B*, vol. 98, p. 205302, Nov 2018.

[6] G. Roussely, E. Arrighi, G. Georgiou, S. Takada, M. Schalk, M. Urdampilleta, A. Ludwig, A. D. Wieck, P. Armagnat, T. Kloss, X. Waintal, T. Meunier, and C. Bäuerle, "Unveiling the bosonic nature of an ultrashort few-electron pulse," *Nature Communications*, vol. 9, p. 2811, July 2018.

[7] S. Datta, *Electronic Transport in Mesoscopic Systems*. Cambridge Studies in Semiconductor Physics and Microelectronic Engineering, Cambridge University Press, 1995.

[8] D. B. Chklovskii, B. I. Shklovskii, and L. I. Glazman, "Electrostatics of edge channels," *Phys. Rev. B*, vol. 46, pp. 4026–4034, Aug 1992.

[9] A. Trellakis, T. Andlauer, and P. Vogl, "Efficient solution of the schrödinger-poisson equations in semiconductor device simulations," in *Large-Scale Scientific Computing* (I. Lirkov, S. Margenov, and J. Waśniewski, eds.), (Berlin, Heidelberg), pp. 602–609, Springer Berlin Heidelberg, 2006.

[10] H. K. Gummel, "A self-consistent iterative scheme for one-dimensional steady state transistor calculations," *IEEE Transactions on Electron Devices*, vol. 11, pp. 455–465, Oct. 1964.

[11] I.-H. Tan, G. L. Snider, L. D. Chang, and E. L. Hu, "A self-consistent solution of Schrödinger–Poisson equations using a nonuniform mesh," *Journal of Applied Physics*, vol. 68, pp. 4071–4076, Oct. 1990.

[12] V. Gudmundsson, "Oscillating impurity spectra caused by non-linear screening in the quantum hall regime," *Solid State Communications*, vol. 74, pp. 63–67, Apr. 1990.

[13] F. Rana, S. Tiwari, and D. A. Buchanan, "Self-consistent modeling of accumulation layers and tunneling currents through very thin oxides," *Appl. Phys. Lett.*, vol. 69, pp. 1104–1106, Aug. 1996.

[14] V. Eyert, "A comparative study on methods for convergence acceleration of iterative vector sequences," *Journal of Computational Physics*, vol. 124, no. 2, pp. 271 – 285, 1996.

[15] A. Vuik, D. Eeltink, A. R. Akhmerov, and M. Wimmer, "Effects of the electrostatic environment on the majorana nanowire devices," *New Journal of Physics*, vol. 18, p. 033013, mar 2016.

[16] A. Trellakis, A. T. Galick, A. Pacelli, and U. Ravaioli, "Iteration scheme for the solution of the two-dimensional Schrödinger-Poisson equations in quantum structures," *Journal of Applied Physics*, vol. 81, pp. 7880–7884, June 1997.

[17] S. Birner, T. Zibold, T. Andlauer, T. Kubis, M. Sabathil, A. Trellakis, and P. Vogl, "nextnano: General purpose 3-d simulations," *IEEE Transactions on Electron Devices*, vol. 54, pp. 2137–2142, Sep. 2007.

[18] H. R. Khan, D. Mamaluy, and D. Vasileska, "Quantum Transport Simulation of Experimentally Fabricated Nano-FinFET," *IEEE Transactions on Electron Devices*, vol. 54, pp. 784–796, Apr. 2007.

[19] X. Gao, D. Mamaluy, E. Nielsen, R. W. Young, A. Shirkhorshidian, M. P. Lilly, N. C. Bishop, M. S. Carroll, and R. P. Muller, "Efficient self-consistent quantum transport simulator for quantum devices," *Journal of Applied Physics*, vol. 115, p. 133707, Apr. 2014.

[20] Y.-M. Niquet, V.-H. Nguyen, F. Triozon, I. Duchemin, O. Nier, and D. Rideau, "Quantum calculations of the carrier mobility: Methodology, matthiessen's rule, and comparison with semi-classical approaches," *Journal of Applied Physics*, vol. 115, no. 5, p. 054512, 2014.

[21] H. Sahasrabudhe, B. Novakovic, J. Nakamura, S. Fallahi, M. Povolotskyi, G. Klimeck, R. Rahman, and M. J. Manfra, "Optimization of edge state velocity in the integer quantum hall regime," *Phys. Rev. B*, vol. 97, p. 085302, Feb 2018.

[22] A. Ben-Israel, "A newton-raphson method for the solution of systems of equations," *Journal of Mathematical Analysis and Applications*, vol. 15, no. 2, pp. 243 – 252, 1966.

[23] J. Nocedal and S. Wright, *Numerical Optimization*. Springer New York, 2006.

[24] P. Andrei and I. Mayergoyz, "Analysis of fluctuations in semiconductor devices through self-consistent Poisson-Schrödinger computations," *Journal of Applied Physics*, vol. 96, pp. 2071–2079, Aug. 2004.

[25] R. Lake, G. Klimeck, R. C. Bowen, D. Jovanovic, D. Blanks, and M. Swaminathan, "Quantum Transport with Band-Structure and Schottky Contacts," *physica status solidi (b)*, vol. 204, no. 1, pp. 354–357, 1997.

[26] A. Pacelli, "Self-consistent solution of the Schrodinger equation in semiconductor devices by implicit iteration," *IEEE Transactions on Electron Devices*, vol. 44, pp. 1169–1171, July 1997.

[27] R. G. Parr and Y. Weitao, *Density-Functional Theory of Atoms and Molecules*. Berlin, Heidelberg: Oxford University Press, 1994.

[28] C. B. Barber, D. P. Dobkin, and H. Huhdanpaa, "The quickhull algorithm for convex hulls," *ACM TRANSACTIONS ON MATHEMATICAL SOFTWARE*, vol. 22, no. 4, pp. 469–483, 1996.

[29] T. Ozaki, "Continued fraction representation of the fermi-dirac function for large-scale electronic structure calculations," *Phys. Rev. B*, vol. 75, p. 035123, Jan 2007.

[30] B. J. van Wees, H. van Houten, C. W. J. Beenakker, J. G. Williamson, L. P. Kouwenhoven, D. van der Marel, and C. T. Foxon, "Quantized conductance of point contacts in a two-dimensional electron gas," *Phys. Rev. Lett.*, vol. 60, pp. 848–850, Feb 1988.

[31] H. van Houten and C. Beenakker, "Quantum point contacts," *Physics Today*, vol. 49, pp. 22–27, jul 1996.

[32] C. Bäuerle, D. C. Glattli, T. Meunier, F. Portier, P. Roche, P. Roulleau, S. Takada, and X. Waintal, "Coherent control of single electrons: a review of current progress," *Reports on Progress in Physics*, vol. 81, p. 056503, apr 2018.

[33] K. v. Klitzing, G. Dorda, and M. Pepper, "New method for high-accuracy determination of the fine-structure constant based on quantized hall resistance," *Phys. Rev. Lett.*, vol. 45, pp. 494–497, Aug 1980.

[34] B. I. Halperin, "Quantized hall conductance, current-carrying edge states, and the existence of extended states in a two-dimensional disordered potential," *Phys. Rev. B*, vol. 25, pp. 2185–2190, Feb 1982.

[35] M. Büttiker, "Absence of backscattering in the quantum hall effect in multiprobe conductors," *Phys. Rev. B*, vol. 38, pp. 9375–9389, Nov 1988.

[36] U. Wulf, V. Gudmundsson, and R. R. Gerhardts, "Screening properties of the two-dimensional electron gas in the quantum hall regime," *Phys. Rev. B*, vol. 38, pp. 4218–4230, Aug 1988.

[37] C. W. J. Beenakker, "Edge channels for the fractional quantum hall effect," *Phys. Rev. Lett.*, vol. 64, pp. 216–219, Jan 1990.

[38] A. Chang, "A unified transport theory for the integral and fractional quantum hall effects: Phase boundaries, edge currents, and transmission/reflection probabilities," *Solid State Communications*, vol. 74, no. 9, pp. 871 – 876, 1990.

[39] D. B. Chklovskii, B. I. Shklovskii, and L. I. Glazman, "Erratum: Electrostatics of edge channels," *Phys. Rev. B*, vol. 46, pp. 15606–15606, Dec 1992.

[40] D. B. Chklovskii, K. A. Matveev, and B. I. Shklovskii, "Ballistic conductance of interacting electrons in the quantum hall regime," *Phys. Rev. B*, vol. 47, pp. 12605–12617, May 1993.

[41] D. Schmerek, S. Manus, A. O. Govorov, W. Hansen, J. P. Kotthaus, and M. Holland, "Compressible and incompressible stripes in a narrow electron channel," *Phys. Rev. B*, vol. 54, pp. 13816–13819, Nov 1996.

[42] R. J. F. van Haren, F. A. P. Blom, and J. H. Wolter, "Direct observation of edge channels in the integer quantum hall regime," *Phys. Rev. Lett.*, vol. 74, pp. 1198–1201, Feb 1995.

[43] Y. Y. Wei, J. Weis, K. v. Klitzing, and K. Eberl, "Edge strips in the quantum hall regime imaged by a single-electron transistor," *Phys. Rev. Lett.*, vol. 81, pp. 1674–1677, Aug 1998.

[44] N. Aoki, C. R. da Cunha, R. Akis, D. K. Ferry, and Y. Ochiai, "Imaging of integer quantum hall edge state in a quantum point contact via scanning gate microscopy," *Phys. Rev. B*, vol. 72, p. 155327, Oct 2005.

[45] R. J. F. van Haren, W. de Lange, F. A. P. Blom, and J. H. Wolter, "Imaging of edge channels in the integer quantum hall regime by the lateral photoelectric effect," *Phys. Rev. B*, vol. 52, pp. 5760–5766, Aug 1995.

[46] K. Panos, R. R. Gerhardts, J. Weis, and K. von Klitzing, "Current distribution and hall potential landscape towards breakdown of the quantum hall effect: a scanning force microscopy investigation," *New Journal of Physics*, vol. 16, p. 113071, nov 2014.

[47] T. Patlatiuk, C. P. Scheller, D. Hill, Y. Tserkovnyak, G. Barak, A. Yacoby, L. N. Pfeiffer, K. W. West, and D. M. Zumbühl, "Evolution of the quantum hall bulk spectrum into chiral edge states," *Nature Communications*, vol. 9, p. 3692, Sept. 2018.

[48] E. M. Kendirlik, S. Sirt, S. B. Kalkan, N. Ofek, V. Umansky, and A. Siddiki, "The local nature of incompressibility of quantum hall effect," *Nature Communications*, vol. 8, p. 14082, Jan. 2017.

[49] N. Pascher, C. Rössler, T. Ihn, K. Ensslin, C. Reichl, and W. Wegscheider, "Imaging the conductance of integer and fractional quantum hall edge states," *Phys. Rev. X*, vol. 4, p. 011014, Jan 2014.

[50] S. Ilani, J. Martin, E. Teitelbaum, J. H. Smet, D. Mahalu, V. Umansky, and A. Yacoby, "The microscopic nature of localization in the quantum hall effect," *Nature*, vol. 427, p. 328, Jan. 2004.

[51] D. Zhang, S. Schmult, V. Venkatachalam, W. Dietsche, A. Yacoby, K. von Klitzing, and J. Smet, "Local compressibility measurement of the $\nu_{tot} = 1$ quantum hall state in a bilayer electron system," *Phys. Rev. B*, vol. 87, p. 205304, May 2013.

[52] K. Lier and R. R. Gerhardts, "Self-consistent calculations of edge channels in laterally confined two-dimensional electron systems," *Phys. Rev. B*, vol. 50, pp. 7757–7767, Sep 1994.

[53] K. Güven and R. R. Gerhardts, "Self-consistent local equilibrium model for density profile and distribution of dissipative currents in a hall bar under strong magnetic fields," *Phys. Rev. B*, vol. 67, p. 115327, Mar 2003.

[54] J. H. Oh and R. R. Gerhardts, "Self-consistent thomas-fermi calculation of potential and current distributions in a two-dimensional hall bar geometry," *Phys. Rev. B*, vol. 56, pp. 13519–13528, Nov 1997.

[55] A. Siddiki and R. R. Gerhardts, "Thomas-fermi-poisson theory of screening for laterally confined and unconfined two-dimensional electron systems in strong magnetic fields," *Phys. Rev. B*, vol. 68, p. 125315, Sep 2003.

[56] A. Siddiki, "Self-consistent coulomb picture of an electron-electron bilayer system," *Phys. Rev. B*, vol. 75, p. 155311, Apr 2007.

[57] G. Bilgeç, H. Üstünel Toffoli, A. Siddiki, and I. Sokmen, "The self-consistent calculation of exchange enhanced odd integer quantized hall plateaus within thomas–fermi–dirac approximation," *Physica E: Low-dimensional Systems and Nanostructures*, vol. 42, no. 4, pp. 1058 – 1061, 2010. 18th International Conference on Electron Properties of Two-Dimensional Systems.

[58] R. R. Gerhardts, K. Panos, and J. Weis, "Current-induced asymmetries of incompressible strips in narrow quantum hall systems," *New Journal of Physics*, vol. 15, p. 073034, jul 2013.

[59] A. E. Kavruk, T. Orzturk, A. Orzturk, U. Atav, and H. Yuksel, "The self-consistent calculation of the edge states in bilayer quantum hall bar," *Journal of Physics: Conference Series*, vol. 334, p. 012066, dec 2011.

[60] T. Suzuki and T. Ando, "Self-consistent edge states of quantum wires in high magnetic fields," *Physica B: Condensed Matter*, vol. 249-251, pp. 415 – 419, 1998.

[61] T. Suzuki and T. Ando, "Self-consistent results in quantum wires in magnetic fields: Temperature effects," *Physica B: Condensed Matter*, vol. 227, no. 1, pp. 46 – 49, 1996. Proceedings of the Third International Symposium on New Phenomena in Mesoscopic Structures.

[62] A. Siddiki and R. R. Gerhardts, "Incompressible strips in dissipative hall bars as origin of quantized hall plateaus," *Phys. Rev. B*, vol. 70, p. 195335, Nov 2004.

[63] A. Salman, M. B. Yucel, and A. Siddiki, "Edge electrostatics revisited," *Physica E: Low-dimensional Systems and Nanostructures*, vol. 47, pp. 229 – 236, 2013.

[64] L. D. Landau and L. M. Lifshitz, *Quantum Mechanics Non-Relativistic Theory, Third Edition: Volume 3.* Butterworth-Heinemann, 3 ed., Jan. 1981.

[65] H. Kamata, T. Ota, K. Muraki, and T. Fujisawa, "Voltage-controlled group velocity of edge magnetoplasmon in the quantum hall regime," *Phys. Rev. B*, vol. 81, p. 085329, Feb 2010.

[66] K. Matveev and L. Glazman, "Conductance and coulomb blockade in a multi-mode quantum wire," *Physica B: Condensed Matter*, vol. 189, no. 1, pp. 266 – 274, 1993.

[67] P. W. Shor, "Algorithms for quantum computation: discrete logarithms and factoring," in *Proceedings 35th Annual Symposium on Foundations of Computer Science*, pp. 124–134, Nov 1994.

[68] A. Wallraff, D. I. Schuster, A. Blais, L. Frunzio, R.-S. Huang, J. Majer, S. Kumar, S. M. Girvin, and R. J. Schoelkopf, "Strong coupling of a single photon to a superconducting qubit using circuit quantum electrodynamics," *Nature*, vol. 431, pp. 162–167, Sept. 2004.

[69] A. A. Houck, D. I. Schuster, J. M. Gambetta, J. A. Schreier, B. R. Johnson, J. M. Chow, L. Frunzio, J. Majer, M. H. Devoret, S. M. Girvin, and R. J. Schoelkopf, "Generating single microwave photons in a circuit," *Nature*, vol. 449, pp. 328–331, Sept. 2007.

[70] N. Roch, M. E. Schwartz, F. Motzoi, C. Macklin, R. Vijay, A. W. Eddins, A. N. Korotkov, K. B. Whaley, M. Sarovar, and I. Siddiqi, "Observation of measurement-induced entanglement and quantum trajectories of remote superconducting qubits," *Phys. Rev. Lett.*, vol. 112, p. 170501, Apr 2014.

[71] R. Hanson, L. P. Kouwenhoven, J. R. Petta, S. Tarucha, and L. M. K. Vandersypen, "Spins in few-electron quantum dots," *Rev. Mod. Phys.*, vol. 79, pp. 1217–1265, Oct 2007.

[72] F. A. Zwanenburg, A. S. Dzurak, A. Morello, M. Y. Simmons, L. C. L. Hollenberg, G. Klimeck, S. Rogge, S. N. Coppersmith, and M. A. Eriksson, "Silicon quantum electronics," *Rev. Mod. Phys.*, vol. 85, pp. 961–1019, Jul 2013.

[73] D. D. Awschalom, L. C. Bassett, A. S. Dzurak, E. L. Hu, and J. R. Petta, "Quantum spintronics: Engineering and manipulating atom-like spins in semiconductors," *Science*, vol. 339, no. 6124, pp. 1174–1179, 2013.

[74] H. Flentje, P.-A. Mortemousque, R. Thalineau, A. Ludwig, A. D. Wieck, C. Bäuerle, and T. Meunier, "Coherent long-distance displacement of individual electron spins," *Nature Communications*, vol. 8, Sept. 2017.

[75] T. Fujita, T. A. Baart, C. Reichl, W. Wegscheider, and L. M. K. Vandersypen, "Coherent shuttle of electron-spin states," *npj Quantum Information*, vol. 3, June 2017.

[76] A. Bertoni, P. Bordone, R. Brunetti, C. Jacoboni, and S. Reggiani, "Quantum logic gates based on coherent electron transport in quantum wires," *Physical Review Letters*, vol. 84, pp. 5912–5915, June 2000.

[77] R. Ionicioiu, G. Amaratunga, and F. Udrea, "Quantum computation with ballistic electrons," *International Journal of Modern Physics B*, vol. 15, pp. 125–133, Jan. 2001.

[78] T. Bautze, C. Süssmeier, S. Takada, C. Groth, T. Meunier, M. Yamamoto, S. Tarucha, X. Waintal, and C. Bäuerle, "Theoretical, numerical, and experimental study of a flying qubit electronic interferometer," *Phys. Rev. B*, vol. 89, p. 125432, Mar 2014.

[79] B. Gaury, J. Weston, M. Santin, M. Houzet, C. Groth, and X. Waintal, "Numerical simulations of time-resolved quantum electronics," *Physics Reports*, vol. 534, no. 1, pp. 1 – 37, 2014. Numerical simulations of time-resolved quantum electronics.

[80] Y. Aharonov and D. Bohm, "Significance of electromagnetic potentials in the quantum theory," *Phys. Rev.*, vol. 115, pp. 485–491, Aug 1959.

[81] H. Batelaan and A. Tonomura, "The aharonov–bohm effects: Variations on a subtle theme," *Physics Today*, vol. 62, pp. 38–43, Sept. 2009.

[82] C. H. W. Barnes, J. M. Shilton, and A. M. Robinson, "Quantum computation using electrons trapped by surface acoustic waves," *Phys. Rev. B*, vol. 62, pp. 8410–8419, Sep 2000.

[83] L. Yu and O. Voskoboynikov, "Ballistic aharonov–bohm quantum bits and quantum gates," *Solid State Communications*, vol. 145, no. 9, pp. 447 – 450, 2008.

[84] H. Schomerus and J. P. Robinson, "Entanglement between static and flying qubits in an aharonov–bohm double electrometer," *New Journal of Physics*, vol. 9, pp. 67–67, mar 2007.

[85] M. Reiher, N. Wiebe, K. M. Svore, D. Wecker, and M. Troyer, "Elucidating reaction mechanisms on quantum computers," *Proceedings of the National Academy of Sciences*, vol. 114, no. 29, pp. 7555–7560, 2017.

[86] H. Duprez, E. Sivre, A. Anthore, A. Aassime, A. Cavanna, A. Ouerghi, U. Gennser, and F. Pierre, "Macroscopic electron quantum coherence in a solid-state circuit," *arXiv e-prints*, p. arXiv:1904.04543, Apr 2019.

[87] J. Weston and X. Waintal, "Towards realistic time-resolved simulations of quantum devices," *Journal of Computational Electronics*, vol. 15, pp. 1148–1157, Dec 2016.

[88] A. Logg and G. N. Wells, "Dolfin: Automated finite element computing," *ACM Trans. Math. Softw.*, vol. 37, pp. 20:1–20:28, Apr. 2010.

[89] T. Kloss, J. Weston, and X. Waintal, "Transient and sharvin resistances of luttinger liquids," *Phys. Rev. B*, vol. 97, p. 165134, Apr 2018.

[90] M. Istas, X. Waintal, and C. Groth, "Getting past the three dimensional wall for quantum transport simulations," *In preparation*, 2019.

[91] P. Gonnet, *Adaptive quadrature re-revisited*. Lulu. com, 2009.